

2005

The interaction between stratification, circulation, and sediment transport in a partially-mixed estuary

Malcolm E. Scully

College of William and Mary - Virginia Institute of Marine Science

Follow this and additional works at: <https://scholarworks.wm.edu/etd>



Part of the [Oceanography Commons](#)

Recommended Citation

Scully, Malcolm E., "The interaction between stratification, circulation, and sediment transport in a partially-mixed estuary" (2005). *Dissertations, Theses, and Masters Projects*. Paper 1539616846. <https://dx.doi.org/doi:10.25773/v5-bp3k-ay70>

This Dissertation is brought to you for free and open access by the Theses, Dissertations, & Master Projects at W&M ScholarWorks. It has been accepted for inclusion in Dissertations, Theses, and Masters Projects by an authorized administrator of W&M ScholarWorks. For more information, please contact scholarworks@wm.edu.

NOTE TO USERS

This reproduction is the best copy available.

UMI[®]

THE INTERACTION BETWEEN STRATIFICATION, CIRCULATION, AND
SEDIMENT TRANSPORT IN A PARTIALLY-MIXED ESTUARY

A Dissertation

Presented to

The Faculty of the School of Marine Science

The College of William and Mary

In Partial Fulfillment

Of the Requirements for the Degree of

Doctor of Philosophy

by

Malcolm E. Scully

2005

UMI Number: 3193094

Copyright 2006 by
Scully, Malcolm E.

All rights reserved.

INFORMATION TO USERS

The quality of this reproduction is dependent upon the quality of the copy submitted. Broken or indistinct print, colored or poor quality illustrations and photographs, print bleed-through, substandard margins, and improper alignment can adversely affect reproduction.

In the unlikely event that the author did not send a complete manuscript and there are missing pages, these will be noted. Also, if unauthorized copyright material had to be removed, a note will indicate the deletion.

UMI[®]

UMI Microform 3193094

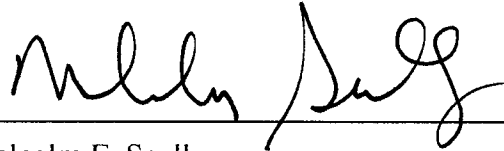
Copyright 2006 by ProQuest Information and Learning Company.

All rights reserved. This microform edition is protected against unauthorized copying under Title 17, United States Code.

ProQuest Information and Learning Company
300 North Zeeb Road
P.O. Box 1346
Ann Arbor, MI 48106-1346

APPROVAL SHEET

This dissertation is submitted in partial fulfillment of
the requirements for the degree of
Doctor of Philosophy



Malcolm E. Scully

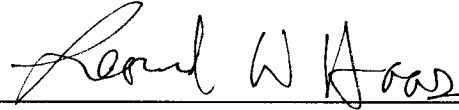
Approved, November 2005



Carl T. Friedrichs, Ph.D.
Committee Chairman/Advisor



John M. Brubaker, Ph.D.



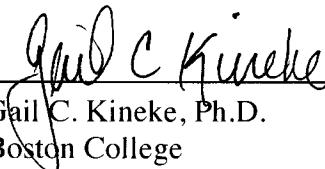
Leonard W. Haas, Ph.D.



L. Donelson Wright, Ph.D.



W. Rockwell Geyer, Ph.D.
Woods Hole Oceanographic Institute
Woods Hole, Massachusetts



Gail C. Kineke, Ph.D.
Boston College
Boston, Massachusetts

TABLE OF CONTENTS

	Page
ACKNOWLEDGMENTS	vi
LIST OF TABLES	vii
LIST OF FIGURES.....	viii
ABSTRACT	xiv
INTRODUCTION AND SUMMARY	2
CHAPTER 1: CONTROL OF ESTUARINE STRATIFICATION BY WIND- INDUCED STRAINING OF THE ESTUARINE DENSITY FIELD.....	7
1.1 INTRODUCTION.....	8
1.2 METHODS	10
1.3 RESULTS	13
1.4 DISCUSSION	21
1.5 CONCLUSION	25
CHAPTER 2: THE IMPORTANCE OF TIDAL AND LATERAL ASYMMETRIES IN STRATIFICATION TO RESIDUAL CIRCULATION IN PARTIALLY-MIXED ESTUARIES	26
2.1 INTRODUCTION.....	27
2.2 METHODS	30
2.2.1 Environmental Setting and Observations	30
2.2.2 Data Analysis.....	33
2.3 RESULTS.....	36
2.3.1 Observations	36
2.3.2 Momentum Balance	50

2.3.3	1-D Modeling Results	54
2.4	DISCUSSION	59
2.5	CONCLUSIONS.....	63
CHAPTER 3: TIDALLY-DRIVEN EKMAN FLOWS IN A SHALLOW STRATIFIED ESTUARY.....		65
3.1	INTRODUCTION.....	66
3.2	OBSERVATIONS AND METHODS.....	68
3.2.1	Study Site.....	68
3.2.2	Observations	70
3.2.3	Momentum Balance	72
3.3	RESULTS	73
3.3.1	Observations	73
3.3.2	Lateral Momentum Balance	84
3.3.3	Simple Model for Lateral Tidal Dynamics.....	87
3.4	DISCUSSION	94
3.4.1	Channel Curvature	94
3.4.2	Bathymetry	95
3.4.3	Sub-tidal Forcing	96
3.5	CONCLUSION	100
CHAPTER 4: SEDIMENT PUMPING BY TIDAL ASYMMETRY IN A PARTIALLY-MIXED ESTUARY.....		103
4.1	INTRODUCTION.....	104
4.2	METHODS	106
4.2.1	Hydrographic Measurements.....	106

4.2.2	Suspended Sediment Measurements	109
4.3	RESULTS	113
4.4	DISCUSSION	120
4.4.1	The Impact of Tidal Asymmetries on the Advective Flux	120
4.4.2	Influence of Sediment Availability	122
4.4.3	Fall Velocity	130
4.5	CONCLUSION	140
	LITERATURE CITED.....	142
	VITA	148

ACKNOWLEDGEMENTS

The research presented in this dissertation would not have been possible without the support and input of my graduate advisor, Dr. Carl Friedrichs. I am extremely grateful for his guidance, encouragement, and patience throughout the course of this project. I also would like to acknowledge the other members of my advisory committee for all of their thoughtful input. I have been fortunate to work closely with all of them during my tenure at VIMS. Numerous people assisted in the fieldwork carried out to support this research. I am deeply indebted to the following people for all of their help: Todd Nelson, Grace Cartwright, Bob Gammisch, Charles Machen, George Pongonis, Wayne Reisner, Sam Wilson, Frank Farmer, and Carol Pollard. I would also like to thank Willy Reay and Joy Austin for their loan of, and assistance with, the YSI 6000 CTDs used in this project. Funding for this research was provided by the National Science Foundation Division of Ocean Sciences Grant OCE-9984941. Most importantly, I would like to thank my parents, Ann and Tucker Scully, and my sister Elinor. They have supported me in everything I have ever done. And finally, I would like to thank Tami Thome. Her love, support and dedication inspire me every day.

LIST OF TABLES

Table		Page
Table 1-1	Correlations between observed lowpass-filtered time-series data.....	20
Table 1-2	Comparison of conditions during flood and ebb, and during up- and down-estuary wind conditions.	20
Table 2-1	Comparison of the median values of the depth averaged current magnitude and duration, stratification, and depth averaged estimate of eddy viscosity from the axial momentum balance for entire data set and spring and neap tidal conditions, segregated by tidal phase.....	38

LIST OF FIGURES

Figure		Page
Figure 1-1	Instrument locations in the 2002 and 2003-04 experiments, York River Estuary, Virginia	11
Figure 1-2	Time series data 2002: a) combined daily river discharge from United States Geological Service’s Mattaponi and Pamunkey gauging station and 60-year averaged daily discharge; b) salinity stratification measured between S4’s 3 and 6 meter above bed; c) depth-averaged current speed measured by S4s; d) wind speed measured at the Virginia Institutes of Marine Sciences’ Byrd Hall; e) along-channel density gradient estimated between the Chesapeake Bay National Estuarine Research Reserve System’s Claybank and Goodwin Island Stations	14
Figure 1-3	Time series data 2003-04: a) combined daily river discharge from United States Geological Service’s Mattaponi and Pamunkey gauging station and 60 year averaged daily discharge; b) salinity stratification measured between conductivity, temperature and depth sensors located 0.2 and 4 meters above bed; c) depth-averaged current speed measured by the acoustic Doppler current profiler; d) wind speed measured at the National Oceanic and Atmospheric Administration’s Sewell’s Point station; e) along-channel density gradient estimated between the Chesapeake Bay National Estuarine Research Reserve System’s Claybank and Goodwin Island Stations	15
Figure 1-4	33-hour lowpass-filtered time series 2002: a) along-channel wind velocity vs. estuarine exchange flow (S4s 3 and 6 meters above bed); b) salinity stratification vs. depth-average eddy viscosity measured by the acoustic Doppler current profiler.....	17
Figure 1-5	33-hour lowpass-filtered time series 2003-04: a) along-channel wind velocity vs. estuarine exchange flow (top and bottom bins of the acoustic Doppler current profiler—6.45 and 1.45 meters above bed); b) salinity stratification vs. depth-average eddy viscosity measured by the acoustic Doppler current profiler.....	18
Figure 1-6	Conceptual model of wind-induced straining of the estuarine density field and responding exchange flow	22
Figure 2-1	Map of study area, York River Estuary, Virginia with estuarine cross-section at “channel” and “shoal” deployment locations. Also shown are locations of the CBNERR CTD sites	31

Figure 2-2	Time series data December 2003—January 2004: a) combined daily river discharge from United States Geological Service’s Mattaponi and Pamunkey gauging stations, with 60-year daily average; b) depth-averaged current magnitude measured by ADCP at the channel site; c) density stratification measured between the highest and lowest CTDs at the channel site (dark line) and the shoal site (light line); d) 35-hour lowpass filtered near-bed currents from the lowest bin of the ADCP at the channel site (dark line) and ADP at the shoal site (light line); e) along channel wind speed measured at the National Oceanic and Atmospheric Administration’s Sewell’s Point station (positive values indicate up-estuary directed wind).....	37
Figure 2-3	Depth averaged along-channel velocity profiles for a) neap and b) spring tidal conditions measured by ADCP at the channel site (dark line) and ADP at the shoal site (dashed line)	40
Figure 2-4	Test of law of the wall using ADV data at channel site. Error estimates for ϕ_m correspond to one standard error	42
Figure 2-5	Smoothed time-series of ϕ_m measured 0.6 mab (solid line) and density stratification measured 0.89 mab (dashed line), both at channel site	43
Figure 2-6	Average tidal cycle values of a) depth averaged current velocities (dark line the channel site and dashed line the shoal site); b) density stratification at the channel site (circles) and shoal site (triangles); c) drag coefficient calculated from ADV data at channel site; d) eddy viscosity measured by ADVs 0.6 mab at channel site; e) the lateral difference in stratification obtained by subtracting stratification measured at the shoal site from the channel site, for neap (solid line) and spring (dashed line) conditions. Vertical lines represent one standard error	46
Figure 2-7	Depth integrated transport measured by the ADCP at the channel site (a) and ADP at the shoal site (b) plotted against the estimate of the depth integrated barotropic pressure gradient.....	49
Figure 2-8	Scatterplot of estimated bed stress from the momentum integral and the quadratic velocity measured 1.4 mab for both channel and shoal sites. Values of C_b are derived from least squares regression of the data	51
Figure 2-9	Median profiles of the eddy viscosity estimated from the momentum integral for both channel and shoal sites during spring	

	and neap tidal conditions (solid line denotes flood and dashed line denotes ebb).....	53
Figure 2-10	Smoothed time-series of the eddy viscosity at the channel site estimated from the momentum integral 1.4 mab (solid line) and by ADVs 0.6 mab (dashed line)	55
Figure 2-11	Results from 1-D turbulence model runs: a) time series of salinity stratification predicted by the model for depths of 5m and 10m (circles represent flood tide and crosses represent ebb tide); b) median eddy viscosity profiles from model run with baroclinic and net ebb-directed barotropic pressure gradient (dashed lines represent flood tide and solid lines represent ebb tide); c) along-channel residual velocity profile for model run with baroclinic and net ebb-directed barotropic pressure gradient; d) along-channel residual velocity profile for model run with no baroclinic or net barotropic pressure gradient	57
Figure 3-1	Map of study area, York River Estuary, Virginia with estuarine cross-section at “channel” and “shoal” deployment locations	69
Figure 3-2	Time series data December 2003 – January 2004: a) combined daily river discharge from United States Geological Service’s Mattaponi and Pamunkey gauging stations, with 60-year daily average; b) depth-averaged current magnitude measured by ADCP at the channel site; c) density stratification measured between the highest and lowest CTDs at the channel site (dark line) and the shoal site (light line); d) lateral salinity difference between channel and shoal location (positive indicates higher salinity in channel) with 35-hour lowpass filter.....	74
Figure 3-3	Average tidal cycle salinity contours from CTD data. Contour interval is 0.4 psu	77
Figure 3-4	Comparison of the observed salinity with the salinity expected due to longitudinal advection. a) channel location; b) shoal location; c) lateral salinity difference (solid lines are the observed values and dashed lines are based on the expected longitudinal advection; positive values indicate the salinity at the channel is greater than the salinity at the shoal).....	78
Figure 3-5	Average profiles of lateral velocity at the shoal (a and b) and channel (c and d), segregated by the phase of the tide (dark line flood, light line ebb). In a and c, the mean profile (dashed line) has been removed.....	81

Figure 3-6	Strength of lateral circulation at channel (dark line) and shoal (light line) locations. The strength of the lateral circulation was calculated by taking the absolute value of the difference between the top and bottom bins of the ADCP/ADP. Values have been smoothed with a 50-hour lowpass filter	83
Figure 3-7	Gradient Richardson number at a) Channel location; b) Shoal location. Horizontal dashed line represents critical value (i.e. $Ri_g = 0.25$). Light solid line represents 50 hour running median	85
Figure 3-8	Estimates of the depth-integrated lateral momentum balance. a) time series of the coriolis forcing compared with lateral pressure gradient; b) scatter plot of depth-integrated coriolis and lateral pressure gradient terms; c) average tidal cycle showing contributions from coriolis (dark line), barotropic pressure gradient (light line), and baroclinic pressure gradient (dashed line)	86
Figure 3-9	Schematic representation of the two-layer reduced gravity model.....	88
Figure 3-10	Predicted surface elevation and pycnocline height from the two-layered model for a) max ebb; b) max flood; and the predicted c) longitudinal and d) lateral velocities for the channel mid-point in the upper (dark line) and lower (light line) layer.....	91
Figure 3-11	Depth-integrated lateral momentum balance for the lower layer from the reduced-gravity model. Consistent with the observations, the balance is geostrophic with the coriolis forcing (dark line), balanced by the combined barotropic (light line) and baroclinic (dashed line) pressure gradients.....	93
Figure 3-12	Analytic solution for tidally varying Ekman-forced lateral flow a) ebb and b) flood for a depth of 10 m and $A_z = 5 \text{ cm}^2/\text{s}$ (solid line) and 6 m and $A_z = 10 \text{ cm}^2/\text{s}$ (dashed line); and c) Steady Ekman solution for a depth of 10 m and $A_z = 5 \text{ cm}^2/\text{s}$ (solid line) and 6 m and $A_z = 10 \text{ cm}^2/\text{s}$ (dashed line) with $d\rho/dx = -3e-4 \text{ kg/m}^4$ and $d\rho/dy = -4e-5 \text{ kg/m}^4$	97
Figure 3-13	Sub-tidal axial momentum (from Scully and Friedrichs, submitted) for the a) Channel and b) Shoal locations. Shown are the axial pressure gradient (dark line), coriolis forcing (dashed line) and stress divergence (light line) terms	101
Figure 4-1	Map of study area, York River Estuary, Virginia with estuarine cross-section at the “channel” and “shoal” deployment locations.....	107

Figure 4-2	Sediment calibration curves for acoustic backscatter from a) ADCP (channel); B) ADP (shoal); c) ADV 0.1 mab (channel); d) ADV 1.1 mab (channel). All calibration curves are plotted against concentration values obtained from co-located transmissometers, except the ADV 1.1 mab, which was calibrated against concentration values obtained from the ADCP	112
Figure 4-3	Time series data December 2003—January 2004: a) combined daily river discharge from United States Geological Service’s Mattaponi and Pamunkey gauging stations, with 60-year daily average; b) depth-averaged current magnitude measured by ADCP at the channel site; c) depth-averaged sediment concentration measured by calibrated ADCP backscatter at the channel site; d) depth-averaged sediment concentration measured by calibrated ADP backscatter at the shoal site; e) density stratification measured between the highest and lowest CTDs at the channel site (dark line) and the shoal site (light line).....	114
Figure 4-4	a) Depth averaged along-channel velocity profiles measured by ADCP at the channel site (dark line) and ADP at the shoal site (light line); b) depth averaged along-channel sediment flux profiles measured by ADCP at the channel site (dark line) and ADP at the shoal site (light line); c) depth averaged profiles of sediment pumping flux (dark line) and advective flux (light line) at the channel site; d) depth averaged profiles of sediment pumping flux (dark line) and advective flux (light line) at the shoal site; e) tidally-averaged sediment concentration profiles for flood (dark line and symbols) and ebb (light line and symbol) at the channel site obtained from calibrated ADCP (lines). Circles represent values obtained from calibrated ADV backscatter and triangles represent values from calibrated transmissometers; f) tidally-averaged sediment concentration profiles for flood (dark line and symbols) and ebb (light line and symbol) at the shoal site obtained from calibrated ADP (lines). Triangles represent values from calibrated transmissometers	115
Figure 4-5	Median profiles of the eddy viscosity (from chapter 2) estimated from the momentum integral for both channel and shoal sites during spring and neap tidal conditions (solid line denotes flood and dashed line denotes ebb).....	118
Figure 4-6	Time series of depth integrated a) total sediment flux; b) advective sediment flux; and c) pumping sediment flux (dark lines represent the channel site and light lines represent the shoal site).	119

Figure 4-7	Bed stress vs. concentration measured 0.10 mab for a) Channel site; and b) Shoal site. Circles indicate flood and crosses indicate ebb. Stress at the channel site was measured by the ADV 0.12 mab and stress at the shoal site was estimated using a drag coefficient (0.0023) and quadratic velocity measure 1.0 mab. Lines indicate a linear regression fit to all data where the stress exceeded 0.3 Pa.....	124
Figure 4-8	a) Sediment erodibility estimated at the channel location, using ADV concentration and stress measured 0.10 mab; b) Bed elevation measured by the acoustic altimetry feature of the ADV 0.10 mab	127
Figure 4-9	Comparison of the depth integrated cumulative sediment flux measured by the ADCP at the channel site (dark line--left axis) and the bed elevation measured by the acoustic altimetry feature of the ADV 0.10 mab (light line-right axis).....	129
Figure 4-10	Estimate of fall velocity from ADV data obtained by regressing the turbulent diffusive sediment flux against concentration as measured by the ADVs a) 0.10 mab; b) 1.1 mab; c) after binning data from each ADV into equal increments based on concentration.....	132
Figure 4-11	Comparison of smoothed time-series (50-hour lowpass filter) of fall velocity (dark line--left axis) and the ratio of ADCP concentration to transmissometer concentration measured 3.1 mab (light line--right axis).	134
Figure 4-12	Frequency histogram of a) floc diameter calculated from the ADV estimate of fall velocity following equation (4-10); b) Kolmogorov micro-scale, estimated following equation (4-8).....	137
Figure 4-13	Comparison of the averaged tidal cycle values of the floc diameter estimated following equation (4-10) (dark circles) and the Kolmogorov micro-scale estimated following equation (4-8) (light triangles). Vertical line represent one standard error	139

ABSTRACT

Detailed field observations from the York River estuary, Virginia are used to examine the processes governing vertical density stratification and to evaluate the importance of spatial and temporal variations in turbulent mixing on estuarine dynamics and sediment transport. Contrary to previous findings that suggest wind stress acts predominantly as a source of energy to mix away stratification, this study demonstrate that the wind can play a more important role in "straining" the along-channel estuarine density gradient. As a result, down-estuary winds enhance the tidally-averaged vertical shear, which interacts with the along-channel density gradient to increase stratification. Conversely, up-estuary winds tend to reduce, or even reverse the vertical shear, reducing stratification. While wind straining can play a dominant role in governing the overall degree of turbulent mixing at sub-tidal time scales, tidal straining of the along-channel density gradient can result in asymmetries in turbulent mixing at the tidal time scale. In estuarine systems with channel-shoal morphologies, tidal straining can lead to asymmetries in turbulent mixing near the deeper channel while the neighboring shoals remain relatively well-mixed. These temporal and spatial variations in turbulent mixing result in a barotropically-induced estuarine residual flow that favors inflow over the shoal regions and outflow over the channel. This pattern of residual circulation can offset, or even reverse, the pattern of residual circulation typically associated with baroclinic estuarine circulation. These tidal asymmetries in mixing have the opposite influence on the patterns of sediment flux. The higher values of eddy viscosity that occur during the less-stratified flood tide resuspend sediment higher in the water column, favoring up-estuary pumping. The presence of strong density stratification significantly damps turbulence in the upper water column, and the lateral dynamical balance is largely geostrophic at tidal time scales. Even though friction does not contribute at lowest order to the lateral balance, the lateral circulation is frictionally-driven by Ekman transport in the bottom boundary layer. The interaction of the lateral circulation and the stratification acts to limit the strength of the lateral circulation and as a result, significantly stronger lateral circulation occurs during less stratified conditions.

**THE INTERACTION BETWEEN STRATIFICATION, CIRCULATION, AND
SEDIMENT TRANSPORT IN A PARTIALLY-MIXED ESTUARY**

INTRODUCTION AND SUMMARY

The presence of horizontal and vertical density gradients is fundamental to estuarine dynamics. Traditionally, the tidally-averaged residual estuarine circulation is treated as a density-driven flow that results from the along-channel density gradient. The interaction between the density-driven residual vertical velocity shear and horizontal density gradient plays a central role in governing vertical density stratification at the sub-tidal time-scale. At tidal time-scales, the interaction between the vertical velocity shear and horizontal density gradient can lead to asymmetries in stratification. Not only does the degree of density stratification vary at a number of important time scales, but there can also be strong spatial gradients in estuarine systems that are caused by variations in bathymetry. It is important to understand how both the spatial and temporal changes in stratification impact the turbulent characteristics of estuarine flows. Vertical density gradients can significantly damp turbulent mixing, fundamentally altering the vertical exchange of momentum. Thus, temporal and spatial variations in turbulent mixing can have profound impacts on estuarine dynamics. The research presented in this dissertation examines the important interactions between vertical density stratification, lateral and axial estuarine circulation, and sediment transport. The first chapter examines the important role the wind-driven circulation plays in governing estuarine circulation and sub-tidal stratification. The role that tidal and lateral asymmetries in turbulent mixing have on the tidally-averaged axial circulation is examined in chapter two. Chapter three examines the tidal lateral dynamic balance and the important interaction between lateral

circulation and stratification. The fourth and final chapter evaluates the importance of tidal asymmetries in turbulent mixing to sediment transport.

In chapter one, observations from the York River Estuary demonstrate that the along-channel wind plays a dominant role in governing the estuarine exchange flow and the corresponding increase or decrease in vertical density stratification. Contrary to previous findings that suggest wind stress acts predominantly as a source of energy to mix away estuarine stratification, these results demonstrate that the wind can play a more important role in “straining” the along-channel estuarine density gradient. As a result, down-estuary winds enhance the tidally-averaged vertical shear, which interacts with the along-channel density gradient to increase vertical stratification. Conversely, up-estuary winds tend to reduce, or even reverse the vertical shear, reducing vertical stratification. In two experiments each lasting approximately a month, the estuarine exchange flow was highly correlated with the along-channel component of the wind. The changes in stratification caused by the exchange flow appear to control the amount of vertical mixing as parameterized by the vertical eddy viscosity. Because decreased mixing enhances the density-driven residual circulation, a positive feedback exists that enhances the estuarine exchange flow during down-estuary wind conditions. A similar feedback limits the strength of the exchange flow when the wind stress is directed up-estuary. The degree of stratification induced by wind straining also appears to play an important role in controlling the effectiveness of wind and tidal mixing. As a result, under stratified conditions wind and tidal mixing need to supply more kinetic energy to overcome the increased potential energy than under more weakly stratified conditions.

Superimposed upon these sub-tidal variations in stratification are both tidal and

spatial asymmetries. Chapter two demonstrates the important impact that tidal and lateral asymmetries in turbulent mixing driven by these patterns of stratification have on the along-channel residual circulation. A reduction in turbulent mixing during the ebb phase of the tide caused by tidal straining of the axial density gradient results in increased vertical velocity shear during the ebb tide. In the absence of significant lateral differences in turbulent mixing, the enhanced ebb-directed transport caused by tidal straining is balanced by a reduction in the net seaward-directed barotropic pressure gradient, resulting in laterally uniform residual flow. However, the channel-shoal morphology of many drowned river valley estuaries often leads to lateral gradients in turbulent mixing. Tidal straining may then lead to tidal asymmetries in turbulent mixing near the deeper channel while the neighboring shoals remain relatively well-mixed. As a result, the largest lateral asymmetries in turbulent mixing occur at the end of the ebb tide when the channel is significantly more stratified than the shoals. The reduced internal friction at the end of ebb delays the onset of the flood tide, increasing the duration of ebb in the channel. Conversely, over the shoal regions where stratification is more inhibited by tidal mixing, there is greater internal friction and the transition from ebb to flood occurs more rapidly. The resulting residual circulation is seaward over the channel and landward over the shoal. The channel-shoal segregation of this barotropically-induced estuarine residual flow is opposite to that typically associated with baroclinic estuarine circulation over channel-shoal bathymetry.

The tidal asymmetries in mixing presented in chapter two are largely limited to lower portion of the water column. The presence of strong density stratification appears to significantly damp turbulence in the upper water column. As a result, estimates of the

dominant terms in the lateral momentum balance during stratified conditions suggest that the dynamical balance is largely geostrophic at tidal time-scales. Even though friction does not contribute at lowest order to the lateral balance, the lateral circulation is frictionally-driven by Ekman transport in the bottom boundary layer. This transport interacts with the density stratification, causing the lateral slope of the pycnocline to oscillate at the tidal frequency. The lateral slope of the pycnocline and the overlying water surface are nearly 180 degrees out of phase and move in opposition in a manner consistent with the thermal wind balance. The interaction of the lateral circulation and the density stratification acts to limit the strength of the lateral circulation and as a result, significantly stronger lateral circulation occurs during less stratified conditions. A simple two-layer reduced-gravity model reasonably represents the observations and is consistent with the estimated lateral momentum balance. While this behavior has been observed in other, significantly deeper systems, these results are surprising given that the mean depth of the mesohaline portion of the York River estuary is less than 5 meters. Despite the fact that such shallow systems are usually considered to be dominated by friction, much of water column appears to be inviscid under stratified conditions. As a result, the interaction of the lateral circulation and density stratification dominates the tidal behavior of the baroclinic pressure gradient and differential longitudinal advection is not dynamically important.

The tidal and lateral variations in stratification described in chapter two, have significant implications to the patterns of sediment transport observed at two laterally adjacent locations in the estuary. Estimates of sediment flux are decomposed into an advective and pumping component to evaluate the importance of tidal asymmetries in

turbulent mixing. At the instrumented location in the estuarine channel, a strong asymmetry in internal mixing due to tidal straining is documented, with higher values of eddy viscosity occurring during the less-stratified flood tide. As a result of this asymmetry, sediment is resuspended higher in the water during the flood phase of the tide resulting in up-estuary pumping of sediment despite a net down-estuary advective flux. At the instrumented location on the adjacent shoal, where no pronounced tidal asymmetry in internal mixing was found, both the pumping flux and advective flux were directed down-estuary. The down-estuary pumping of sediment on the shoal appears to be driven by asymmetries in bed stress. The impact of tidal asymmetries in bed stress at the channel location was negated because the amount of sediment available for resuspension was limited. As a result, the pumping flux was dominated by the overlying asymmetries in internal mixing. The asymmetries in stratification appear to exert an important control on the vertical distribution of sediment by both impacting the eddy diffusivity as well as the fall velocity. During the more turbulent flood tide, the fall velocities are smaller suggesting the Kolmogorov micro-scale is setting the upper bound on floc diameter.

CHAPTER 1

CONTROL OF ESTUARINE STRATIFICATION BY WIND-INDUCED STRAINING OF THE ESTUARINE DENSITY FIELD

1.1 INTRODUCTION

Stratification in estuarine environments is often thought of as a result of the competition between the effect of stirring due the wind and tides and the stratifying influence of tidal straining and a baroclinic exchange flow (e.g. Simpson et al., 1991). A number of authors have approached the dynamics of coastal and estuarine stratification by examining the vertically integrated potential energy anomaly (Simpson & Bowers, 1981; Simpson et al. 1990). Using this approach, several studies have successfully predicted the major features of the temporally varying vertical stratification field, including semi-diurnal tidal asymmetries and spring-neap variability in stratification (Simpson et al., 1990; Simpson et al., 1991; Sharples et al., 1994). However, in applying these models, the wind was always treated as a source of kinetic energy that promotes mixing. Its ability to drive circulation that interacts with the along-channel density gradient and both create and destroy stratification via horizontal advection has been largely ignored in estuarine environments.

This approach is flawed because often the wind plays a dominant role in controlling the non-tidal circulation in estuaries. Studies of the Providence River documented a strong inverse correlation between the wind and the non-tidal near bed currents (Weisberg, 1976). Similar observations were made in the Potomac River (Elliott, 1978), the upper Chesapeake Bay (Wang, 1979), and Mobile Bay (Noble et al., 1996). While these authors often describe a near-bed return flow that opposes the wind as baroclinic, they simply invoke continuity to explain its physics. In the lower

Chesapeake Bay, Wang (1979) describes the in-phase relationship between the non-tidal surface and bottom currents and the wind as barotropic, and the phase lag between the bottom currents and the wind in the upper Bay as baroclinic. While his model successfully describes the observations, it does not include a role of the along-channel density gradient. Interestingly, Wang (1979) does suggest that the wind-driven circulation may play an important role in controlling vertical density stratification, which may impact the vertical eddy viscosity. However, no observations were collected to support this hypothesis.

In two shallow estuarine systems in Waquoit Bay, Geyer (1997) demonstrated that down-estuary winds enhanced surface outflow, significantly reducing the along-estuary salinity gradient. However, the response of these shallow systems is fundamentally different than deeper partially-mixed estuaries. In contrast to the data presented by Wang (1979), Geyer's results demonstrate an overall decrease in vertical stratification associated with down-estuary winds. More recently, field observations and numerical modeling studies of the upper Chesapeake Bay demonstrate rapid up-estuary movement of the salt front in response to down-estuary winds (North et al., 2004). Their observations and modeling results show increased stratification associated with down-estuary wind events, but do not explicitly address the role that the increased stratification may play in reducing vertical mixing and enhancing the baroclinically-driven estuarine circulation.

These previous studies have clearly demonstrated the important role that wind forcing can play in estuarine systems. However, the role that the wind plays in directly "straining" the estuarine density field has not been sufficiently documented in the

literature to our knowledge. In this chapter, we demonstrate that during periods of energetic winds in a partially-mixed estuary, the along-channel wind is the dominant mechanism driving the estuarine exchange flow and, as a result, exerts a first order control on the development of stratification. It is our assertion that the wind often plays a larger role in “straining” the along-channel density gradient than it does in providing energy to mix away estuarine stratification. In fact, we will demonstrate that in some cases changes in stratification due to “wind straining” are greater than those caused by tidal straining and spring-neap variability. Additionally, because the along-channel wind exerts a first order control on stratification via straining, it greatly influences the vertical eddy viscosity, further influencing the estuarine exchange flow.

1.2 METHODS

Field experiments were carried out in the York River Estuary during spring 2002 and winter 2003-04. Both experiments were located in the mesohaline portion of the estuary as shown in Fig. 1-1. During 2002, a bottom mounted RDI 1200 kHz, acoustic Doppler current profiler (ADCP) was deployed on the west flank of the main channel. The ADCP recorded vertical profiles of current velocity and was programmed using mode 12 to sample at 1 Hz and collect data in 0.50 m bins continuously. Because the memory and battery constraints using this intensive sampling strategy limited the total sampling time to roughly one week, the ADCP was retrieved, serviced, and redeployed twice during the experiment. This approach yielded roughly 25 days of data with two breaks during which servicing of the instrument was performed. Roughly 2 km upstream from the ADCP location, a mooring containing two InterOcean S4 current and

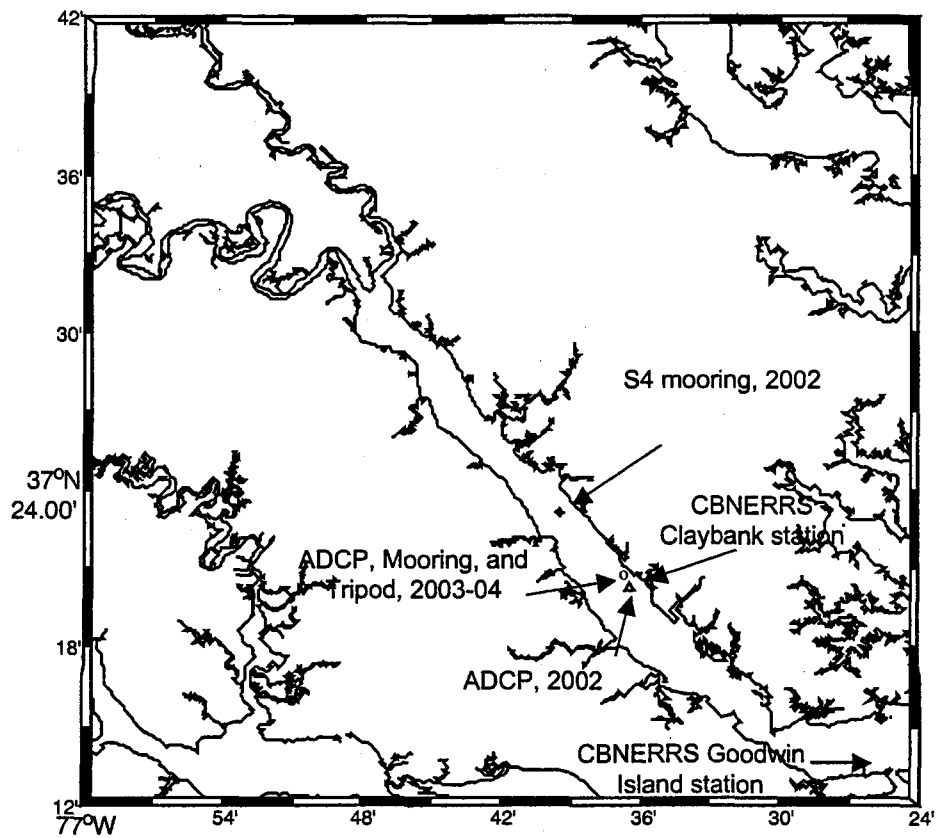


Figure 1-1. Instrument locations in the 2002 and 2003-04 experiments, York River Estuary, Virginia.

conductivity sensors was deployed. The surface and bottom S4s were located approximately 6 and 3 meters above bed (mab), respectively, giving point measurements of temperature, salinity, and current velocity. Mean water depths at the ADCP and mooring location were approximately 6 and 7 meters, respectively.

During the winter of 2003-04, a similar array of instruments was deployed in nearly the same location. Again, the 1200 kHz ADCP was located on the west flank of the main channel. The ADCP was programmed to sample in a manner identical to that of 2002 experiment, except that a burst sampling scheme that collected one 10-minute burst every hour was used to prolong the sampling duration. Adjacent to the ADCP was a benthic boundary layer tripod containing three YSI conductivity, temperature and depth (CTD) probes located 0.20, 0.39, and 1.74 mab. Additionally, an adjacent mooring had a CTD roughly 2.8 mab and an S4 sensor roughly 4 mab. The mean water depth at the main channel instrument location was about 6 m.

The two data sets described above were used to assess the influence of the along-channel wind on the observed estuarine circulation and vertical stratification. During 2002, the wind speed and direction were obtained from the Virginia Institute of Marine Sciences' (VIMS) meteorological observation station located atop Byrd Hall located near the mouth of the York River Estuary. Because of damage to that station incurred during Hurricane Isabel, wind data for 2003-04 was obtained from the Sewell's Point meteorological station maintained by the National Oceanic and Atmospheric Association (NOAA), located roughly 36 km southeast of VIMS. Winds were rotated 30 degrees west of north to conform to the main axis of the York River. Winds are treated in the

oceanographic context, indicating the direction towards which they are blowing (i.e., NW wind is ebb directed and negative).

1.3 RESULTS

The 2002 and 2003-04 experiments took place during contrasting freshwater flow conditions. During 2002, large portions of the east coast of the United States were experiencing historic drought conditions. During March of 2002, discharge into the York River Estuary from the Mattaponi and Pamunkey Rivers was 87% below the 60-year monthly average (Fig. 1-2a). With the relatively low river discharge, the vertical salinity stratification was weak ranging from a maximum of 1 psu/m to nearly well-mixed conditions (Fig. 1-2b). In contrast, the 2003-04 experiment took place during relatively wet conditions, when discharge from the York River tributaries for December 2003 was, on average, nearly 3 times the 60 year average (Fig. 1-3a). This large river discharge led to considerably more vertical salinity stratification, with maximum values of almost 3 psu/m (Fig. 1-3b). Both experiments lasted for roughly one month and captured the spring-neap variability in the tidal currents (Figs. 1-2c and 1-3c). During both experiments winds were moderately energetic with several events where the wind speed exceeded 10 m/s (Figs. 1-2d and 1-3d).

In order to examine the residual circulation, the velocity data from the 2002 and 2003-04 experiments were filtered using a 33-hour lowpass-filter to remove the tidal signal. The strength of the estuarine exchange flow (ΔU) is calculated by subtracting the lowpass-filtered along-channel velocities measured highest in the water column from that measured at the location lowest in the water column (positive values consistent with density-induced estuarine circulation). In both years, there is a strong inverse correlation

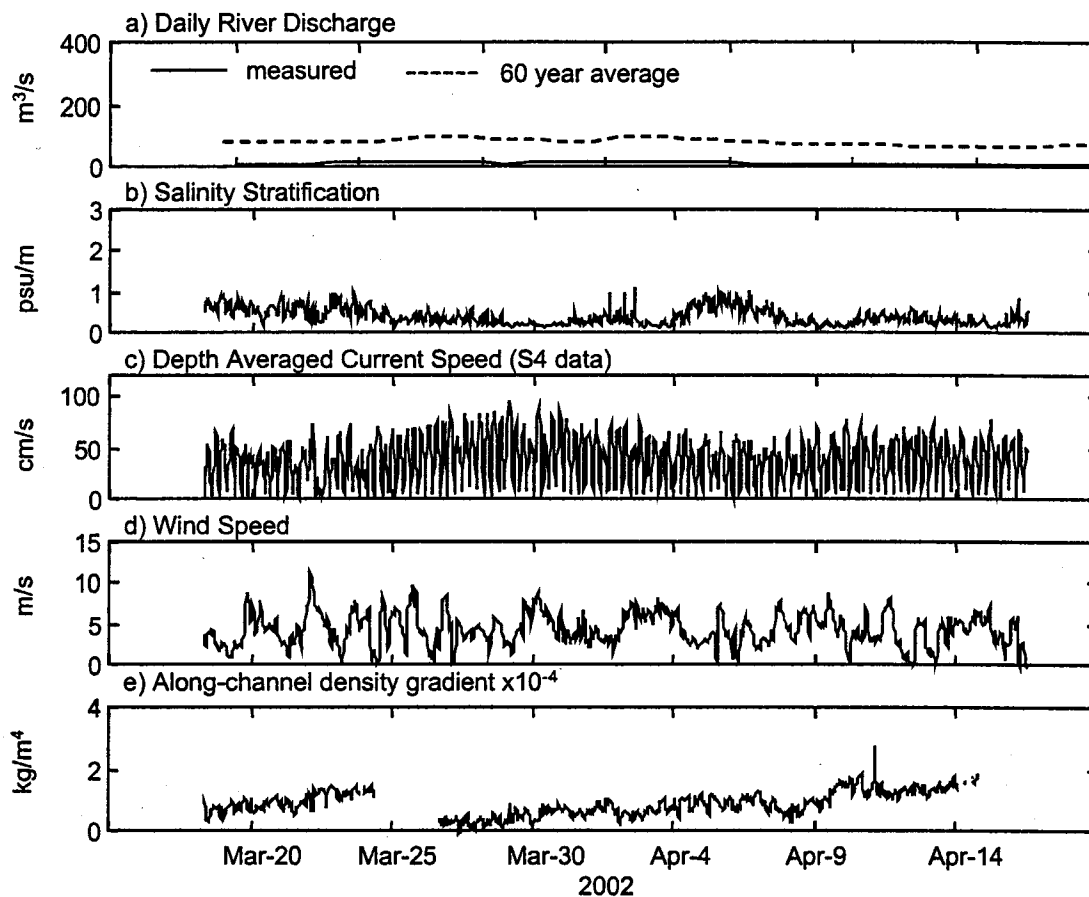


Figure 1-2. Time series data 2002: a) combined daily river discharge from United States Geological Service's Mattaponi and Pamunkey gauging station and 60-year averaged daily discharge; b) salinity stratification measured between S4's 3 and 6 meter above bed; c) depth-averaged current speed measured by S4s; d) wind speed measured at the Virginia Institutes of Marine Sciences' Byrd Hall; e) along-channel density gradient estimated between the Chesapeake Bay National Estuarine Research Reserve System's Claybank and Goodwin Island Stations.

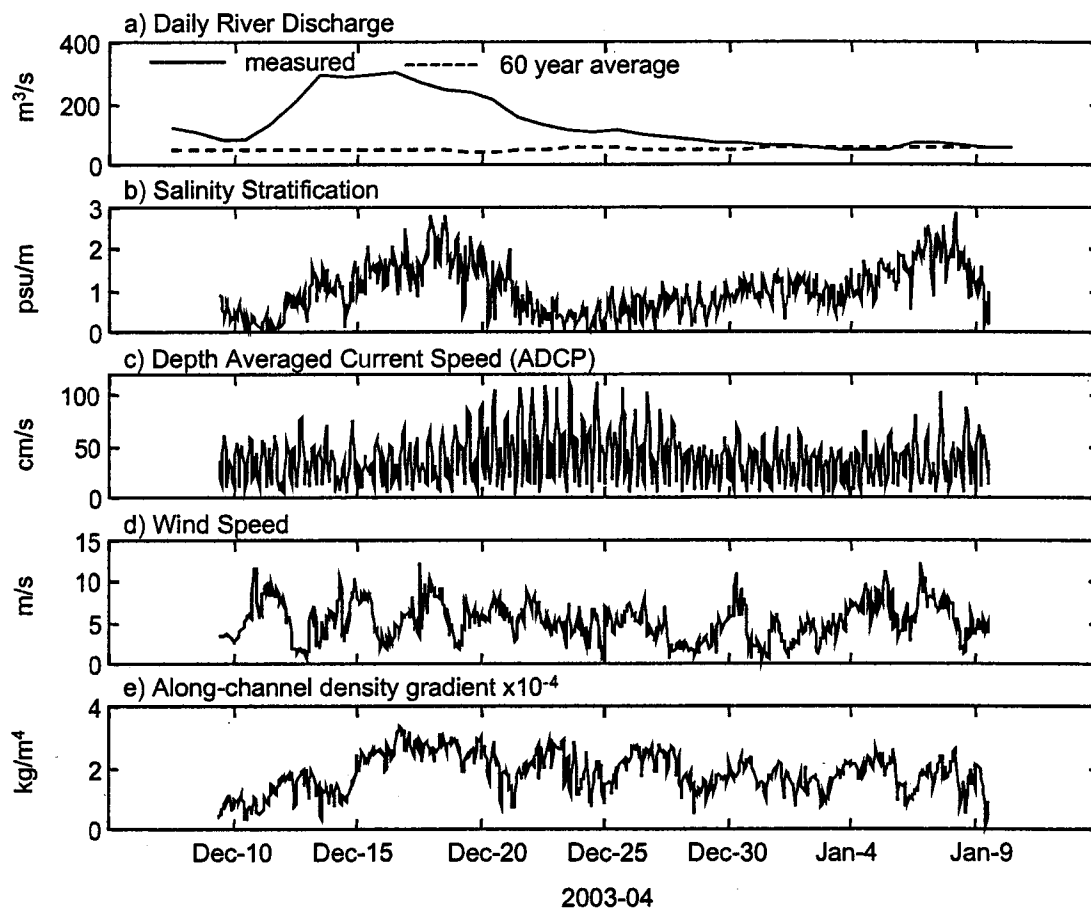


Figure 1-3. Time series data 2003-04: a) combined daily river discharge from United States Geological Service's Mattaponi and Pamunkey gauging station and 60 year averaged daily discharge; b) salinity stratification measured between conductivity, temperature and depth sensors located 0.2 and 4 meters above bed; c) depth-averaged current speed measured by the acoustic Doppler current profiler; d) wind speed measured at the National Oceanic and Atmospheric Administration's Sewell's Point station; e) along-channel density gradient estimated between the Chesapeake Bay National Estuarine Research Reserve System's Claybank and Goodwin Island Stations.

between the along-channel component of the wind and the estuarine exchange flow (Figs. 1-4a and 1-5a). There is a clear pattern in which down-estuary winds increase the estuarine exchange flow while up-estuary winds reduce or even reverse the exchange flow.

The interaction of the estuarine exchange flow and the along-channel salinity gradient exerts an important control on the vertical density stratification. As a result, periods of down-estuary winds increase the exchange flow and tend to increase the vertical salinity stratification, while up-estuary winds tend to decrease the vertical stratification. This can be seen clearly in both the 2002 and 2003-04 datasets, where there is negative correlation between the along-channel component of the wind and the vertical salinity stratification (Figs. 1-4 and 1-5). In both years there is a stronger correlation between the along-channel component of the wind (including its sign) and the vertical stratification than between the overall magnitude of the wind and the stratification (table 1-1). In fact, during the 2003-04 experiment the vertical stratification is more negatively correlated with the along-channel wind than it is with the depth-averaged, lowpass-filtered current magnitude. In 2002, the along-channel wind and the current magnitude are equally correlated with the vertical salinity stratification, suggesting that tidal mixing also is playing a significant role in governing stratification during the 2002 experiment. In either case, the along-channel wind is exerting a major influence on the degree of salinity stratification.

The degree of salinity stratification is one of the fundamental parameters governing estuarine dynamics. Increases in salinity stratification can damp vertical mixing, decreasing the vertical eddy viscosity. In both 2002 and 2003-04, the 1200 kHz

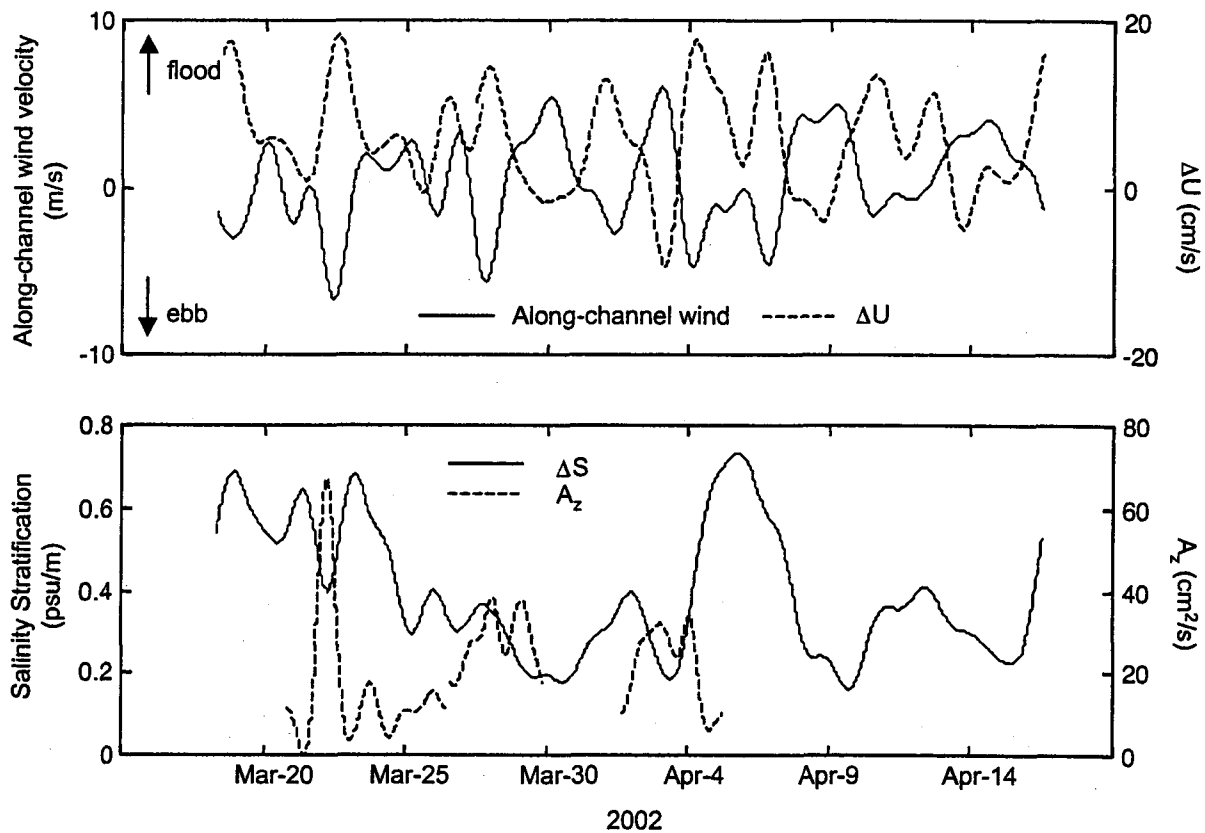


Figure 1-4. 33-hour lowpass-filtered time series 2002: a) along-channel wind velocity vs. estuarine exchange flow (S4s 3 and 6 meters above bed); b) salinity stratification vs. depth-average eddy viscosity measured by the acoustic Doppler current profiler.

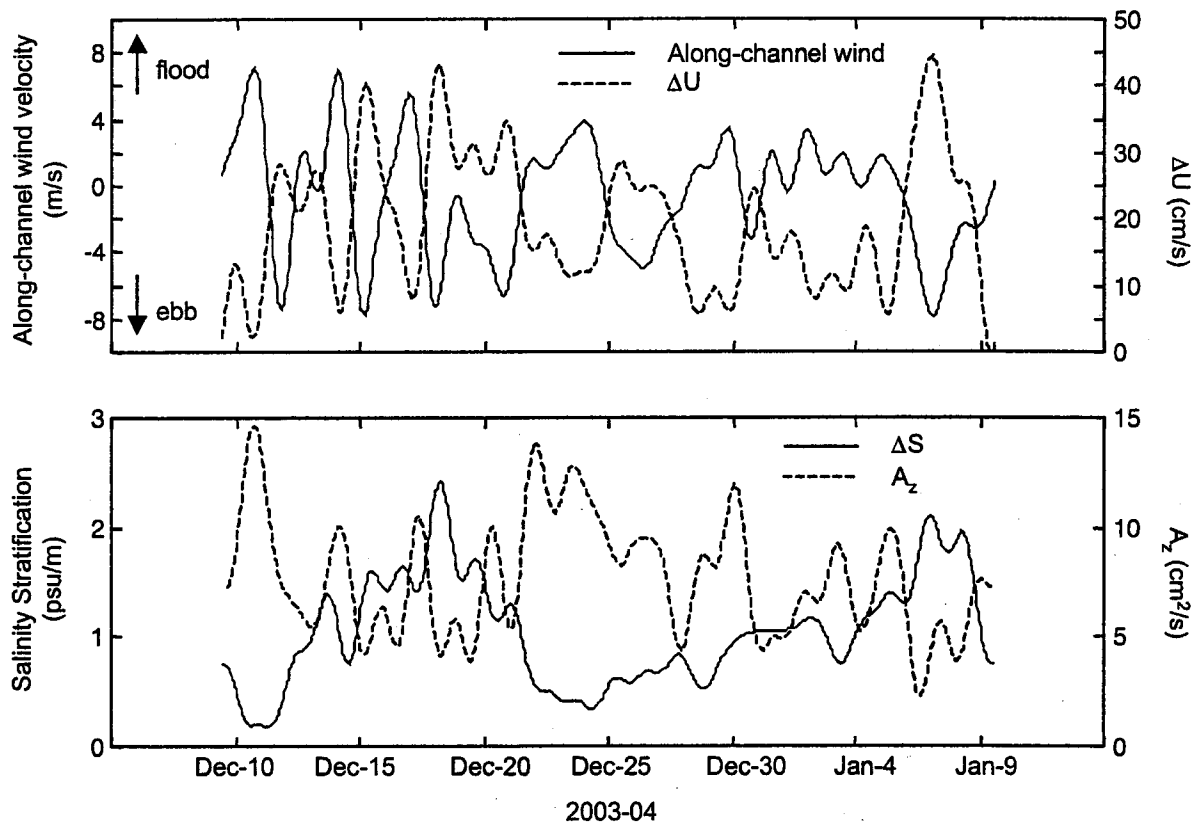


Figure 1-5. 33-hour lowpass-filtered time series 2003-04: a) along-channel wind velocity vs. estuarine exchange flow (top and bottom bins of the acoustic Doppler current profiler—6.45 and 1.45 meters above bed); b) salinity stratification vs. depth-average eddy viscosity measured by the acoustic Doppler current profiler.

ADCP collected along-beam velocities enabling the application of the variance method of Stacey et al. (1999) to calculate vertical profiles of Reynolds stress. Using the estimates of Reynolds stress and the observed vertical velocity shear, the vertical eddy viscosity was estimated for all of the 2003-04 experiment and for the portions of the 2002 experiment when ADCP data was available. After calculating profiles of eddy viscosity, the data were depth-averaged and smoothed using a 33-hour lowpass filter. Figures 1-4b and 1-5b demonstrate a negative correlation between the observed salinity stratification and our estimates of eddy viscosity. The estimates of eddy viscosity demonstrate that the changes in vertical salinity stratification caused by the along-channel winds can significantly alter the amount of vertical mixing. In table 1-2, the data from both the 2002 and 2003-04 experiments is differentiated by flood and ebb tides, as well as by the direction of the along-channel wind. During the 2003-04 experiment, the ebb tide experienced greater vertical salinity stratification than the flood, consistent with the concept of “tidal straining” (Simpson et al., 1990). As expected, the vertically averaged eddy viscosity measured using the ADCP is larger on flood than on ebb. However, differences in stratification caused by the direction of the along-channel wind are greater than those due to the tidal asymmetry. This results in larger eddy viscosities during periods of up-estuary directed wind than during periods of down-estuary directed wind. Despite the fact that both the magnitude of the wind and vertically averaged currents are larger during periods experiencing down- versus up-estuary winds, the median eddy viscosity is over 30% lower in association with the increased salinity stratification during periods of down-estuary winds.

		2003-04 Experiment								
		Current magnitude	Wind magnitude	Along-channel wind	ΔU	ΔS	A_z	$\partial\rho/\partial x$		
2002 Experiment	Current magnitude		0.01	-0.12	0.11	-0.28	0.38	0.26		Current magnitude
	Wind magnitude	-0.23		-0.38	0.36	0.24	0.16	0.18		Wind magnitude
	Along-channel wind	0.14	0.39		-0.84	-0.42	0.52	0.29		Along-channel wind
	ΔU	-0.11	-0.37	-0.85		0.58	-0.57	0.35		ΔU
	ΔS	-0.51	-0.44	-0.51	0.45		-0.68	0.43		ΔS
	A_z	0.20	0.57	-0.25	-0.35	-0.56		-0.15		A_z
	$\partial\rho/\partial x$	0.13	-0.28	0.10	0.10	0.13	-0.05			$\partial\rho/\partial x$
		Current magnitude	Wind magnitude	Along-channel wind	ΔU	ΔS	A_z	$\partial\rho/\partial x$	2003-04 Experiment	
		2002 Experiment								

Table 1-1. Correlations between observed lowpass-filtered time-series data.

2002 Experiment				
	Flood	Ebb	Up-Estuary Wind	Down-Estuary Wind
Median A_z (cm^2/s)	8.31	9.31	9.90	7.67
Median dS/dz (psu/m)	0.41	0.33	0.30	0.44
Median Current Speed (m/s)	0.31	0.32	0.34	0.29
Median Wind Speed (m/s)	4.57	4.29	5.15	3.95
2003-04 Experiment				
	Flood	Ebb	Up-Estuary Wind	Down-Estuary Wind
Median A_z (cm^2/s)	5.08	3.84	5.17	3.64
Median dS/dz (psu/m)	0.98	1.03	0.86	1.16
Median Current Speed (m/s)	0.32	0.41	0.36	0.37
Median Wind Speed (m/s)	4.95	5.31	4.67	5.68

Table 1-2. Comparison of conditions during flood and ebb, and during up- and down-estuary wind conditions.

The pattern observed during the 2002 experiment is consistent with the observations from 2003-04. Interestingly, during the 2002 experiment, the flood tide consistently is more stratified than the ebb. Nonetheless, changes in salinity stratification and vertical eddy viscosity caused by the direction of the along-channel wind still appear to play a greater role than tidal asymmetries. However, during periods of down-estuary winds, the tidal currents and wind magnitude on average are greater than during periods of up-estuary wind making these results more ambiguous than during 2003-04.

1.4 DISCUSSION

The classic analytic solution for density-induced estuarine circulation primarily is dependent upon three variables: estuarine depth, eddy viscosity, and the along-channel density gradient (Officer, 1976). Although this profile is based upon a number of simplifying assumptions, it still provides insight into the fundamental controls on the strength of the estuarine exchange flow associated with gravitational circulation. Our observations suggest that the “straining” of the along-channel density gradient by the along-channel component of the wind, exerts a first order control on the vertical stratification, which then governs the vertical eddy viscosity. We contend that these changes in eddy viscosity ultimately play a leading role in governing the strength of the exchange flow (Fig. 1-6). However, the along-channel density gradient also may influence the strength of the estuarine exchange flow. During the both 2002 and 2003-04 experiments, the along-channel density gradient was estimated from the Chesapeake Bay National Estuarine Research Reserve System’s monitoring stations located at Claybank and the Goodwin Islands along the York River (<http://cdmo.baruch.sc.edu/>) (see Fig. 1-1). During both 2002 and 2003-04, there was only a weak correlation between the

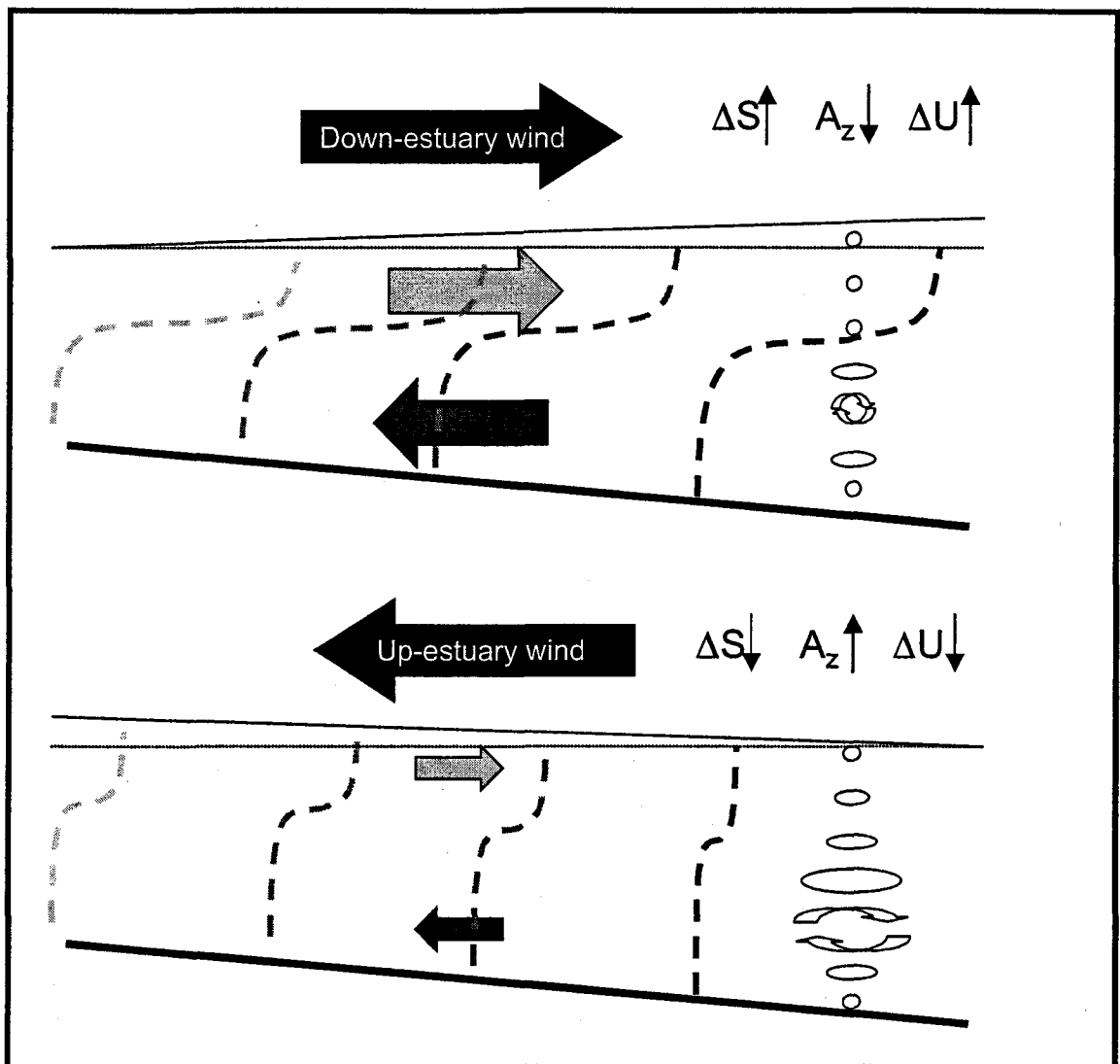


Figure 1-6. Conceptual model of wind-induced straining of the estuarine density field and responding exchange flow.

lowpass-filtered along-channel density gradient and the exchange flow and between the along-channel wind and the along-channel density gradient (table 1-1). During both experiments, the negative correlation between the estimated eddy viscosity and the strength of the exchange flow is larger in magnitude than the correlation with the along-channel density gradient. Although along-channel density gradient was larger during the 2003-04 experiment when the estuarine exchange was stronger, the data suggest that on shorter time scales, temporal changes in eddy viscosity play a more dominant role in controlling the estuarine exchange flow than changes in the along-channel density gradient.

A limitation of these data sets is the location of the instruments in the main channel. In order to minimize interference with shipping traffic, the instruments were deployed on the southwestern flank of the channel at a depth of approximately 6 m. However, the main channel reaches a maximum depth of approximately 9 m in this reach of the river. Thus, the instrumentation does not measure the full profile of the estuarine circulation over the deepest portion of the estuarine cross-section. As a result, a portion of the net up-estuary residual circulation that occurs in the deeper portions of the channel is not accounted for. The relatively shallow locations of the ADCP and S4 moorings results in the lowest velocity measurement being located only slightly below the null point in the residual circulation profile. Clearly there is a portion of net return flow that is not being captured. However, we would only expect the pattern revealed by the data to be stronger if the deepest portion of the cross-section were resolved.

Although these data demonstrate the important role that wind plays in straining the along-channel density field, there is also evidence for wind mixing. For example, on

22 March 2002 the mean wind speed exceeded 10 m/s towards the south, and there was a significant reduction in the vertical density stratification and increase in eddy viscosity. An interesting contrast occurred on 17 December 2003. During this period, peak wind speed exceeded 10 m/s and again was generally directed down-estuary. However, instead of causing substantial mixing, this energetic wind event increased stratification, leading to one of the most stratified periods observed during either experiment. One interesting pattern that emerges is that during less stratified conditions, the wind was more effective at creating mixing. The much higher river discharge and generally more stratified conditions during 2003-04 were more resistant to both wind and tidal mixing. This can be seen clearly in table 1-1. During the 2003-04 experiment the vertical salinity stratification is not negatively correlated with the wind magnitude and there is only a weak negative correlation between the stratification and the current magnitude. The correlation between the eddy viscosity and the wind magnitude is significantly larger during the 2002 experiment and both wind and tidal mixing appear to be much more effective at creating mixing than during the following year.

These results highlight several weaknesses of the potential energy approach to examining density stratification. First of all, the wind not only plays a role in creating mixing, but it also influences the tidally-averaged vertical shear that acts on the along-channel salinity gradient to increase or decrease the vertical stratification via straining. Secondly, our results indicate that changes in the vertical eddy viscosity fundamentally control the strength of the estuarine exchange flow. Without accounting for these temporal changes in the eddy viscosity and feedback between stratification and turbulent mixing, understanding and predicting important estuarine parameters such as vertical

stratification will be difficult. Lastly, the degree of stratification feeds back to influence the effectiveness of both wind and tidal mixing. As a result, using a constant efficiency parameter to represent the effectiveness of mixing has only limited applicability and cannot be implemented effectively a priori.

1.5 CONCLUSIONS

Data from two contrasting experiments demonstrate that the along-channel wind plays a significant role in driving the estuarine exchange flow. During two experiments in both wet and draught conditions, the estuarine exchange flow was most highly correlated with the along-channel component of the wind. This exchange flow interacts with the along-channel salinity gradient so that down-estuary winds favor the development of vertical stratification, while up-estuary winds inhibit it. Thus, "wind straining" of the along-channel salinity gradient often results in greater changes in stratification than asymmetries associated with tidal straining. This suggests that in many estuarine environments the along-channel wind stress may play a larger role in straining the along-channel salinity gradient than in promoting turbulent mixing. During periods of down-estuary winds, a positive feedback exists in which increased exchange flow increases salinity stratification, which in turn reduces the vertical eddy viscosity (Fig. 1-6). The magnitude of the resulting exchange flow is more closely related to changes in eddy viscosity due to wind-induced straining than to changes in the along-channel density gradient. Furthermore, changes in eddy viscosity associated with wind straining fundamentally impact the efficiency of both wind and tidal mixing. These data suggest that in order to accurately model the temporal evolution of estuarine stratification, one must account for these feedback mechanisms associated with wind-induced straining.

CHAPTER 2

THE IMPORTANCE OF TIDAL AND LATERAL ASYMMETRIES IN STRATIFICATION TO RESIDUAL CIRCULATION IN PARTIALLY-MIXED ESTUARIES

2.1 INTRODUCTION

The understanding of tidally-averaged residual circulation is fundamental to the study of estuarine processes. The classic representation of the two-layer estuarine exchange flow was represented by Pritchard (1956) as the balance between the seaward directed barotropic pressure gradient, the landward directed baroclinic pressure gradient, and the stress divergence. The internal friction associated with the exchange flow is often parameterized in terms of a vertically and tidally-averaged eddy viscosity acting on the tidally-averaged vertical velocity shear. This representation of estuarine circulation has been the cornerstone for the classical understanding of estuarine dynamics. However, the use of a tidally-averaged mixing coefficient may often be inappropriate in characterizing the basic forcing driving tidally-averaged residual circulation in estuarine systems where there are significant spatial and temporal variations in turbulent mixing.

In many estuarine systems, the interaction between the vertical tidal shear and the longitudinal density gradient can lead to tidal asymmetries in density stratification. This process, known as tidal straining (Simpson et al., 1990), favors the development of stratification during ebb tides and the destruction of stratification during the flood and can lead to significant tidal asymmetries in vertical mixing (Stacey et al., 1999; Geyer et al., 2000; Rippeth et al., 2001). Jay and Smith (1990) suggested that tidal asymmetries in vertical mixing associated with tidal straining could play an important role in generating residual circulation in estuaries. They argued that reduction of tidal mixing during ebb combined with increased near-bed mixing during flood could generate a two layer tidally-

averaged residual circulation qualitatively similar to a baroclinically driven exchange flow. Consistent with Jay and Smith's results, Stacey et al. (2001) kinematically described the two-layer residual circulation in northern San Francisco Bay as the barotropic response to tidal asymmetries in vertical mixing. In a study carried out in the Hudson River Estuary, Geyer et al. (2000) also observed tidal asymmetries in the vertical mixing coefficients associated with tidal straining, but concluded that the tidally-averaged estuarine circulation was not fundamentally affected by this internal asymmetry. In a companion paper, however, Trowbridge et al. (1999) found the relationship between bottom stress and the near-bed velocity shear in the Hudson systematically departed from the law of the wall during ebb tides, consistent with greater stratification due to tidal straining. Trowbridge et al. (1999) hypothesized that the departure from the law of the wall on ebb was not due to local stratification, but caused by overlying stratification remotely damping the near-bed turbulent length scale. Similar findings were presented by Scully and Friedrichs (2003), who demonstrated significant damping of near-bed turbulence by non-local, overlying stratification in the York River estuary.

These previous studies provide a somewhat contradictory view of the affect that tidal asymmetries in mixing have on estuarine residual circulation. While Jay and Smith (1990) and Stacey et al. (2001) suggest tidal straining of the density field enhances up-estuary residual flow near the bed, Geyer et al. (2000) concluded that asymmetries in vertical mixing had little impact on the near-bed residual circulation. Trowbridge et al. (1999) and Scully and Friedrichs (2003) suggested that tidal straining of the density field

often leads to increased velocity shear on ebb near the bed, which would presumably favor down-estuary residual flow.

In addition to the variations in turbulent mixing caused by temporal changes in stratification, many estuarine systems exhibit spatial gradients in mixing caused by lateral bathymetric variability. The impact of bathymetry on residual estuarine circulation has been addressed analytically by a number of authors (Wong, 1994; Kasai et al., 2000; Valle-Levinson et al., 2003). However, their analytical approach uses a spatial and temporally constant eddy viscosity and thus cannot account for asymmetries in turbulent mixing. Only the analytical model of Friedrichs and Hamrick (1996) attempted to account for lateral variations in mixing by assuming the eddy viscosity scaled with depth. Drowned river valley estuaries often have channel-shoal morphologies, with marked lateral variations in density stratification. Lateral mixing fronts often form at breaks in topography, separating the relatively well-mixed water on the shoal from the more stratified waters over the channel (Huzzey and Brubaker, 1988). In contrast to the approach suggested by Friedrichs and Hamrick (1996), the absence of stratification over the shoal may enhance turbulent mixing relative to the more stratified channel. Despite the fact that lateral variability in stratification in many systems may exceed temporal variations arising from tidal straining, its role in modulating residual circulation has been largely ignored.

In this chapter, measurements collected at two laterally adjacent locations are used to examine the forces driving residual circulation in the York River estuary. The observational and analytical methods are described in Section 2-2 and the results are presented in Section 2-3. The results include direct measurements that document tidal

asymmetries in turbulent mixing. Lateral asymmetries in turbulent mixing are inferred from stress estimates based on the dominant terms in the axial momentum balance. Finally, results from a relatively simple numerical experiment utilizing k-epsilon turbulence closure are presented to examine in more detail the physical mechanisms that create residual flows in estuaries experiencing tidal and lateral asymmetries in stratification. The results are discussed in Section 2-4 and conclusions are presented in Section 2-5.

2.2 METHODS

2.2.1 Environmental Setting and Observations

Observations were collected in the mesohaline portion of the York River estuary during the winter of 2003-04 (Fig. 2-1). The York River is a partially-mixed sub-estuary of the Chesapeake Bay that forms at the confluence of the Mattaponi and Pamunkey Rivers. Most of the York River is characterized by a main channel with an approximate depth of 10 meters, flanked by broad shoals with a mean depth of approximately 4 meters. Although the mean tidal range is only about 0.7 meters, tidal currents are energetic with surface currents reaching over 1 m/s during spring tidal conditions. Both salinity and temperature exhibit significant seasonal variability, however the density gradient is nearly always dominated by gradients in salt. Top to bottom salinity stratification can range from well-mixed to greater than 12 psu.

During the winter of 2003-04, instrumentation was maintained at two laterally adjacent locations in the estuarine cross-section near Clay Bank, located roughly 13 kilometers up-estuary from Gloucester Point. At this location in the York River, the main channel of the estuary is located on the northeastern side of the river with a maximum

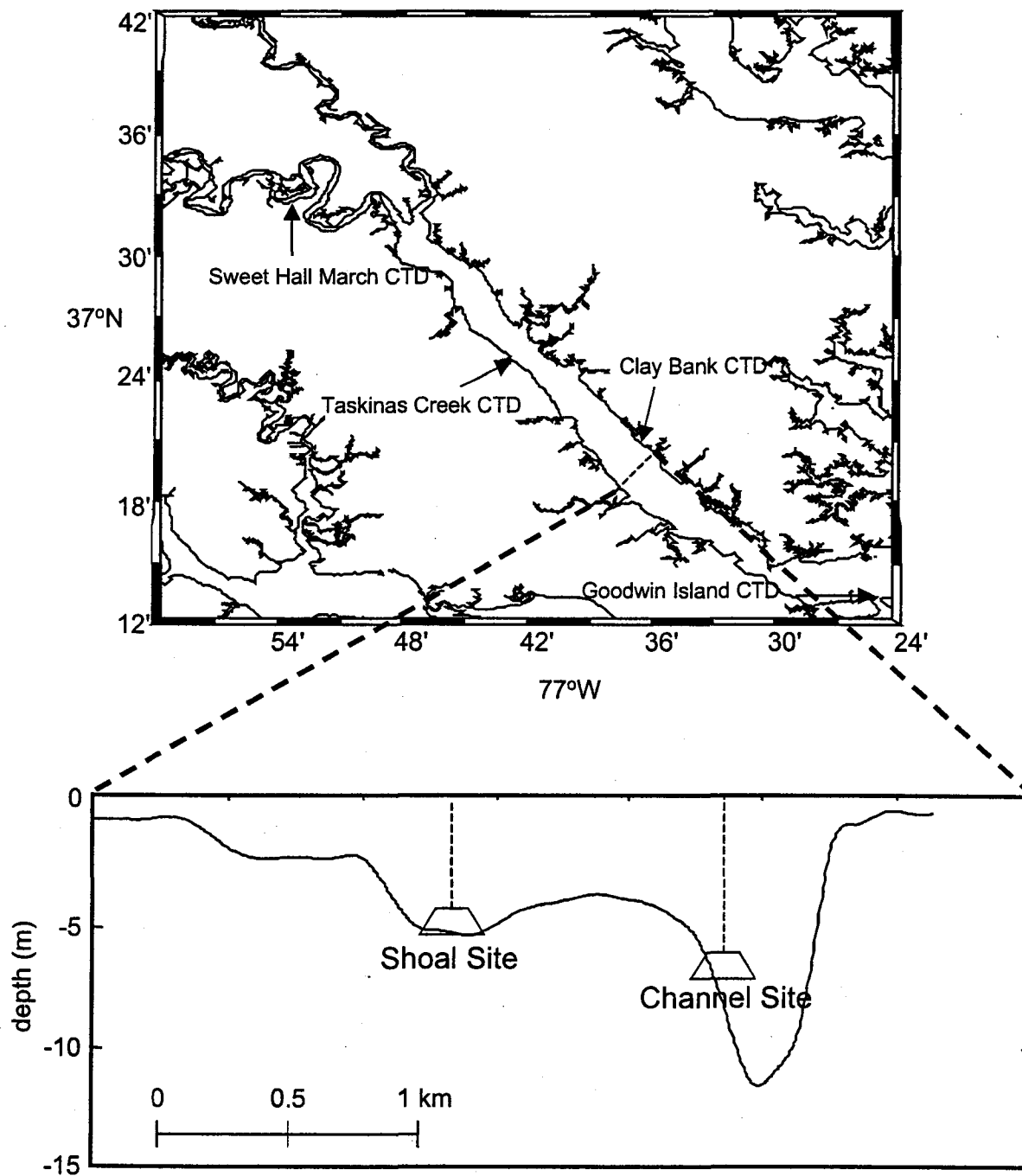


Figure 2-1. Map of study area, York River Estuary, Virginia with estuarine cross-section at “channel” and “shoal” deployment locations. Also shown are locations of the CBNERR CTD sites.

depth of approximately 10 meters. A broad shoal extends to the southwest of the main navigational channel with a maximum depth of approximately 6.5 meters. Instruments were deployed along the southwestern side of the main channel at a water depth of approximately 7 meters (“channel” site) to avoid interfering with navigation, and at the deepest location within the southwestern shoals at a water depth of roughly 6 meters (“shoal” site).

During the experiment, detailed velocity measurements were collected by 4 Sontek acoustic Doppler velocimeters (ADV), an RDI 1200 kHz acoustic Doppler current profiler (ADCP), and a Sontek 1500 kHz acoustic Doppler profiler (ADP). The 4 ADVs were mounted on a benthic boundary layer tripod deployed at the channel site to provide high-resolution velocity measurements at discrete elevations over the lowest 1.2 meters of the water column. The ADVs were mounted 0.10, 0.43, 0.76, and 1.1 meters above the bed (mab), on an arm of the tripod that was rotated perpendicular to the dominant orientation of the York River channel. Unfortunately, the ADVs at 0.43 and 0.76 mab did not function properly and will not be discussed. The ADVs collected three-dimensional velocity measurements in 5 minute bursts once an hour at a sampling frequency of 5 Hz. The 1200 kHz ADCP was deployed immediately adjacent to the tripod at the channel site and collected vertical profiles of current velocity in 0.50 m bins. The ADCP sampled at roughly 1 Hz and collected one 10-minute burst every hour. The 1500 kHz ADP was deployed at the shoal site and sampled at a rate of 1 Hz averaged over one minute bursts to provide vertical profiles of current velocity in 0.25 m bins.

Three YSI 6000 conductivity, temperature and depth sensors (CTDs) were mounted on the tripod at the channel site at 0.10, 0.41, and 1.4 mab and collected

pressure, salinity, and temperature every 30 minutes. A mooring that consisted of a YSI 6000 CTD and an InterOcean S4 current meter, outfitted with a CTD was located immediately adjacent to the tripod at the channel site. The CTD and S4 on the mooring were located 2.8 and 3.4 mab, respectively. At the shoal site, two YSI 6600 CTDs located 0.10 and 1.5 mab and an InterOcean S4 sensor with a CTD located 3.5 mab were deployed immediately adjacent to the ADP. In addition to the field instrumentation deployed as part of this experiment, the Chesapeake Bay National Estuarine Research Reserve (CBNERR) maintains four YSI 6600 data sondes year-round along the York River estuary as shown in Figure 2-1. Each sensor is mounted on a fixed platform immediately below mean low water and measures a variety of environmental parameters every 15 minutes. In this chapter, we use the CBNERR pressure sensor data to estimate the along-channel barotropic pressure gradient.

2.2.2 Data Analysis

The primary focus of this chapter is to examine how asymmetries in turbulent mixing associated with temporal and spatial gradients in density stratification impact the tidally-averaged residual circulation. Direct measurements of stress are available from the ADV data collected at the channel site. To calculate stress from the ADV data, the flow measurements in each burst were first rotated vertically such that no mean vertical velocity was present. Flow measurements were then rotated horizontally into the predominant along channel direction. Reynolds stress calculations were made using the covariance method as described by Kim et al. (2000), where:

$$\tau_b = \rho \langle u' w' \rangle \quad (2-1)$$

The angled brackets indicate time-averaging, and u' and w' represent the turbulently fluctuating components of the along-channel and vertical velocities, respectively.

Although there were no direct measurements of stress at the shoal site, estimates of stress can be obtained from the dominant terms in the axial momentum balance (Geyer, et al. 2000; Winant and Guitierrez, 2003). Neglecting rotation and the advective terms, the along-channel momentum balance can be written approximately as:

$$\frac{\partial u}{\partial t} = -g \frac{\partial \eta}{\partial x} + \frac{g}{\rho} \int \frac{\partial \rho}{\partial x} dz + \frac{1}{\rho} \frac{\partial \tau}{\partial z} \quad (2-2)$$

where u is the along-estuary velocity, g is the acceleration of gravity, η is the sea surface elevation anomaly, x is the horizontal coordinate (positive landward), ρ is the density of water, τ is the Reynolds stress and z is the vertical coordinate (positive upward). We followed the methods of Geyer et al. (2000) and vertically integrated (2-2) to solve for the vertical profile of the effective stress (τ), assuming that $d\rho/dx$ to be independent of z . This assumption was confirmed by two longitudinal hydrographic surveys conducted during the experiment.

The acceleration term ($\partial u/\partial t$) was easily determined from both the ADCP and ADP data. The barotropic pressure gradient was calculated from the difference between the pressure sensors deployed by CBNERR at the Sweet Hall Marsh and Goodwin Island locations. Although they were separated by the greatest distance of the four pressure sensors, the instrumented cross-section was located nearly equidistant from these two sensors. Additionally, we previously compared the along-channel barotropic pressure gradient calculated from all possible combinations of these four CBNERR sensors that coincided with data collected by tide gauges during an experiment in 2002 (Scully et al., 2003; Simpson et al., 2005). The gradient measured between the Sweet Hall Marsh and

Goodwin Island CBNERR stations best matched the well constrained local tide gauge data collected during 2002. When calculating the barotropic pressure gradient from the CBNERR pressure sensor data, there was an unknown offset between the two sensors due to their fixed heights relative to the local geopotential surface. Consistent with methods of Geyer et al. (2000), this difference was determined by requiring the zero-crossings of the momentum-integral estimates of near-bed stress to occur at the times of the zero-crossings of the near-bed velocity.

In calculating the baroclinic pressure gradient, the along channel salinity gradient was estimated using the S4 data from the channel and shoal sites based on the local salt conservation equation, ignoring lateral advection and vertical turbulent flux:

$$\frac{ds}{dx} = -\frac{1}{u} \frac{ds}{dt} \quad (2-3)$$

The relatively minor contribution of the axial temperature gradient was not included in the estimate of the baroclinic pressure gradient. The estimates of ds/dx using (2-3) were low-passed filtered to remove the high-frequency noise associated with this method. The separate estimates from the two adjacent locations were then averaged, assuming that the along-channel density gradient did not vary significantly in the across-channel direction. The time-series of ds/dx obtained in this manner has a temporal variability consistent with that derived from the CBNERR data. Estimates from the various CBNERR stations could not be used directly because of a number of issues including, 1) the presence of fresh water at the Sweet Hall Marsh location; 2) lateral density differences between Clay Bank and Taskinas Creek; and 3) salinity gradient reversals near the mouth of the estuary. In calculating the baroclinic pressure gradient for both experiments, we assumed that dp/dx does not vary with depth. Although there may be some errors in both our

estimate of the barotropic and baroclinic pressure gradients, these errors have a similar impact on the stress estimates at each across-channel location because it is unlikely that there are persistent lateral differences in either $\partial\eta/\partial x$ or $\partial\rho/\partial x$.

In integrating (2-2), the surface stress was set equal to the wind stress calculated using the bulk formula of Large and Pond (1981). Wind data was obtained from the Sewell's Point meteorological station maintained by the National Oceanic and Atmospheric Association (NOAA), located roughly 36 km southeast of Gloucester Point. The coordinate system was rotated 30 degrees west of north so that the winds conform to the main axis of the York River. With the relatively moderate winds observed during the experiment, the momentum estimates of internal stress were relatively insensitive to the inclusion of the surface wind stress. However, the wind plays an important role in modulating both the tidally-averaged barotropic pressure gradient and the degree of salinity stratification, as described by Scully et al. (2005).

2.3 RESULTS

2.3.1 Observations

The 2003-04 experiment took place during a period of elevated rainfall. Discharge from the York River tributaries for December 2003 was, on average, nearly 3 times the 60-year average (Fig. 2-2a). The experiment spanned approximately 30 days, covering the full spring-neap tidal cycle. The spring-neap cycle was apparent in the depth averaged current magnitude measured at the channel site (Fig. 2-2b). With the elevated river discharge, there was persistent vertical density stratification throughout much of the experiment at both the channel and shoal sites, especially during neap tide (Fig. 2-2c). The vertical stratification exceeded 2 kg/m^4 on several occasions at both

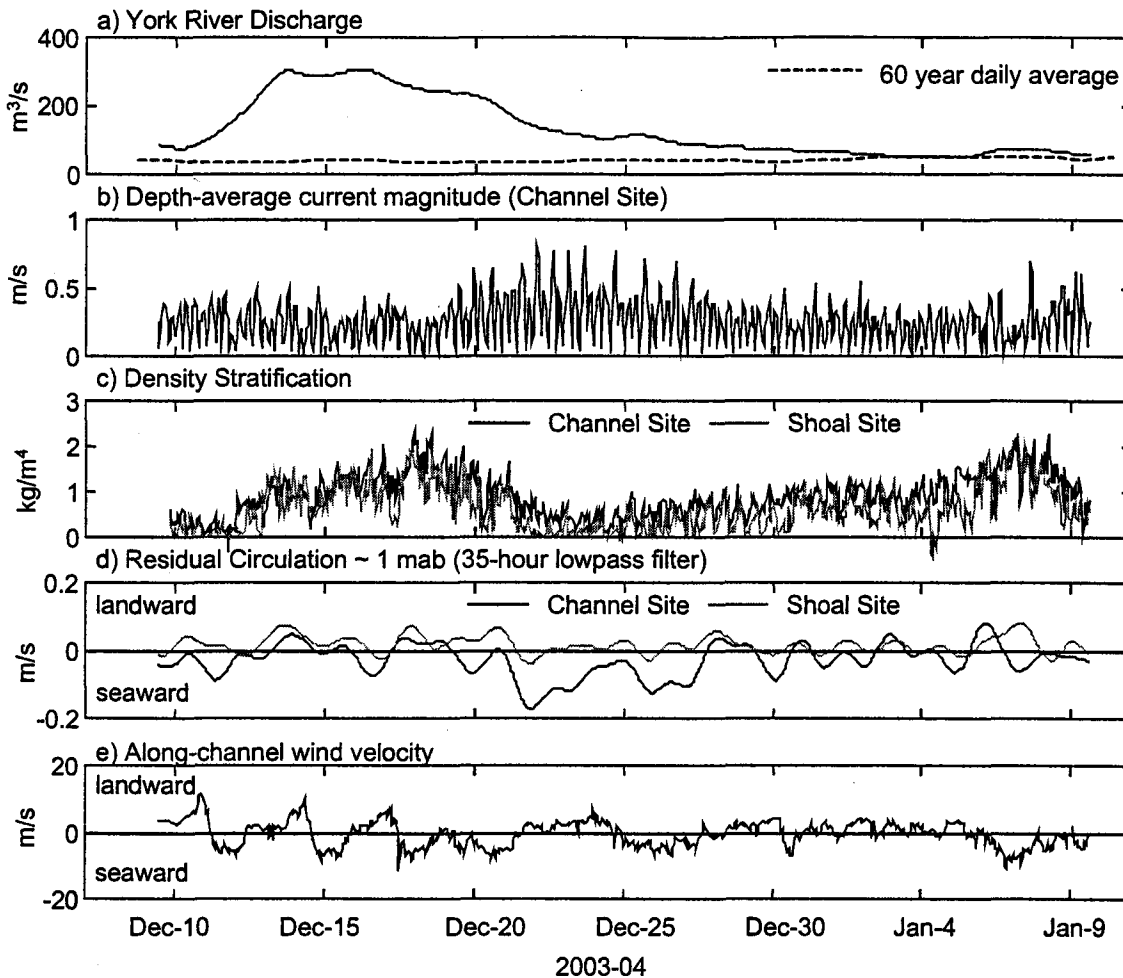


Figure 2-2. Time series data December 2003—January 2004: a) combined daily river discharge from United States Geological Service's Mattaponi and Pamunkey gauging stations, with 60-year daily average; b) depth-averaged current magnitude measured by ADCP at the channel site; c) density stratification measured between the highest and lowest CTDs at the channel site (dark line) and the shoal site (light line); d) 35-hour lowpass filtered near-bed currents from the lowest bin of the ADCP at the channel site (dark line) and ADP at the shoal site (light line); e) along channel wind speed measured at the National Oceanic and Atmospheric Administration's Sewell's Point station (positive values indicate up-estuary directed wind).

locations, and median values of stratification measured between the upper-most and lower-most sensors were 0.88 and 0.58 kg/m⁴ at the channel and shoal sites, respectively. In addition, significant tidal asymmetries in stratification were observed at both locations. At the channel site, the median stratification on flood and ebb was 0.81 and 0.94 kg/m⁴, respectively (Table 2-1). The asymmetry had the opposite sense at the shoal site, where the flood was actually more stratified on average than the ebb (0.65 and 0.53 kg/m⁴). This pattern of tidal asymmetry led to the greatest lateral asymmetry in stratification during the ebb tide, which significantly impacted the estuarine dynamics as discussed below. At both locations, the overall degree of stratification also was modulated by the advective effect of wind-driven circulation (Scully et al., 2005).

All Data				
	Channel		Shoal	
	Flood	Ebb	Flood	Ebb
<U> (m/s)	0.33	-0.41	0.32	-0.43
Duration	43.4%	56.6%	48.2%	51.8%
dp/dz (kg/m ⁴)	0.81	0.94	0.65	0.53
<A _z > (cm ² /s)	13.1	12.6	16.1	19.1
Neap Tide				
	Channel		Shoal	
	Flood	Ebb	Flood	Ebb
<U> (m/s)	0.29	-0.37	0.29	-0.39
Duration	44.1%	55.9%	46.9%	53.1%
dp/dz (kg/m ⁴)	0.85	1.02	0.80	0.62
<A _z > (cm ² /s)	8.6	12.1	10.7	17.6
Spring Tide				
	Channel		Shoal	
	Flood	Ebb	Flood	Ebb
<U> (m/s)	0.36	-0.49	0.37	-0.48
Duration	42.8%	57.2%	49.5%	50.5%
dp/dz (kg/m ⁴)	0.73	0.78	0.37	0.40
<A _z > (cm ² /s)	26.8	13.6	30.7	30.3

Table 2-1. Comparison of the median values of the depth averaged current magnitude and duration, stratification, and depth averaged estimate of eddy viscosity from the axial momentum balance for entire data set and spring and neap tidal conditions, segregated by tidal phase.

The subtidal near-bed currents at both sites exhibited significant variability (Fig. 2-2d). However, a consistent pattern emerged; on average, the currents tended to be more seaward directed at the channel site than at the shoal site, particularly during spring tidal conditions. This pattern was seen clearly in the velocity profiles collected by the ADCP and ADP. Figure 2-3 shows the velocity profiles collected at each site, averaged separately over neap and spring tidal conditions. For all cases, the tidally-averaged along-channel velocity profiles demonstrated vertical shear consistent with the classic view of estuarine circulation. However, there was significant lateral shear during spring tidal conditions when the currents at the shoal site were relatively more landward directed than at the channel site. It is important to note that while the depth at the two sites was roughly the same, the deployments at the channel site were not located at the deepest point in the main channel to avoid interfering with shipping traffic. As a result, the velocity profiles at the channel site did not capture the landward directed-residual that we assume occurred over the deepest portion of the channel.

Previous authors have documented that the presence of vertical density stratification causes excess shear relative to the Prandtl-Karman law of the wall relationship (e.g.; Smith and McLean, 1977; Soulsby and Dyer, 1981; Friedrichs et al., 2000). It follows that increased stratification on the ebb tide due to tidal straining would lead to a greater departure from the law of the wall and hence (in the absence of an opposing barotropic pressure gradient) favor down estuary residual flow. We evaluated the relationship between stress and velocity shear by comparing the observed near-bed shear with that expected based on the law of the wall, given as:

$$\kappa z \frac{du}{dz} = u_* \quad (2-4)$$

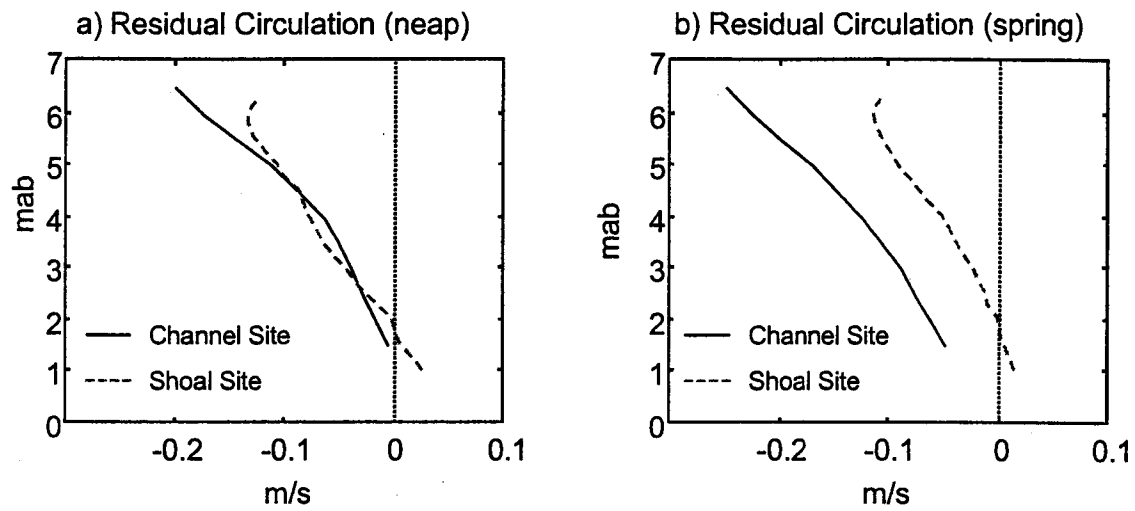


Figure 2-3. Depth averaged along-channel velocity profiles for a) neap and b) spring tidal conditions measured by ADCP at the channel site (dark line) and ADP at the shoal site (dashed line).

The observed shear was calculated by differencing the along-channel velocity from the two functioning ADVs at the channel site, and u_* ($\langle u'w' \rangle^{1/2}$) was calculated from the stress measured by the lowest ADV sensor (0.10 mab). The empirical value of 0.41 was used for κ , and $z = 0.6$ m (the mean height of the two ADV sensors). Figure 2-4 plots $\kappa z du/dz$ as a function of u_* . Although the data were noisy, they exhibited a roughly linear relationship with an intercept of approximately zero (regression to all data resulted in slope of 1.5 and intercept of -0.003). The slope of the regression was greater than the expected value of unity for law of the wall scaling. It should be noted that use of a linear average in estimating z may slightly over-estimate $\kappa z du/dz$ under well-mixed conditions, since du/dz decreases nonlinearly with height in a log layer. In the atmospheric literature, the ratio of $\kappa z du/dz$ to u_* (defined as ϕ_m) is often used to quantify the departure from the law of the wall (e.g., Bussinger et al., 1971). To estimate ϕ_m , we fit the data with a least squares regression. Flood and ebb data were fit separately, the regression was forced through the origin, and all data where the sign of the shear and u_* were opposite were excluded. As a result, 78 percent of the data were used in the regression. The regression analysis yielded values of ϕ_m of 1.5 and 2.0 for flood and ebb, respectively, consistent with the observations of persistent near-bed stratification, as well as with the observed tidal asymmetries in stratification at the channel site.

We evaluated the temporal impact of stratification on boundary layer shear by calculating hourly values of ϕ_m from the ADV data at the channel site. Figure 2-5 shows the time series of ϕ_m compared with the density stratification observed 0.9 mab at the channel location. Because the estimates of ϕ_m were noisy, the data were smoothed using a locally weighted scatterplot smoothing (lowess) filter (Cleveland, 1979) with an 8

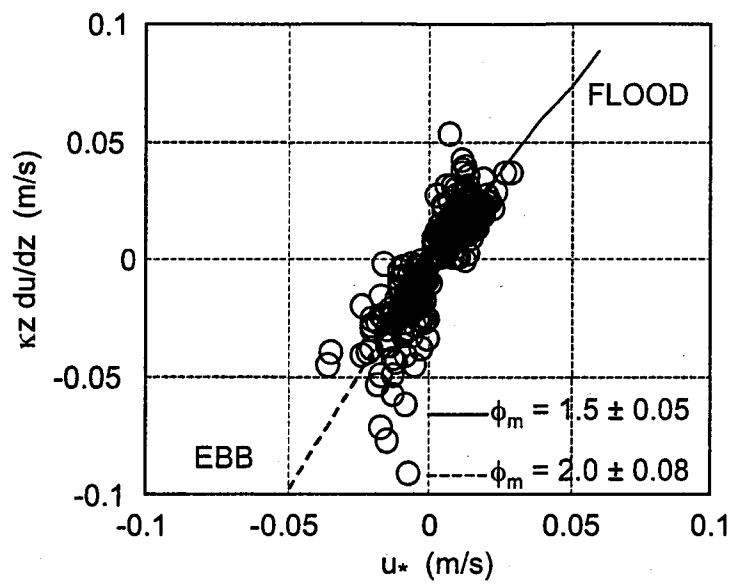


Figure 2-4. Test of law of the wall using ADV data at channel site. Error estimates for ϕ_m correspond to one standard error.

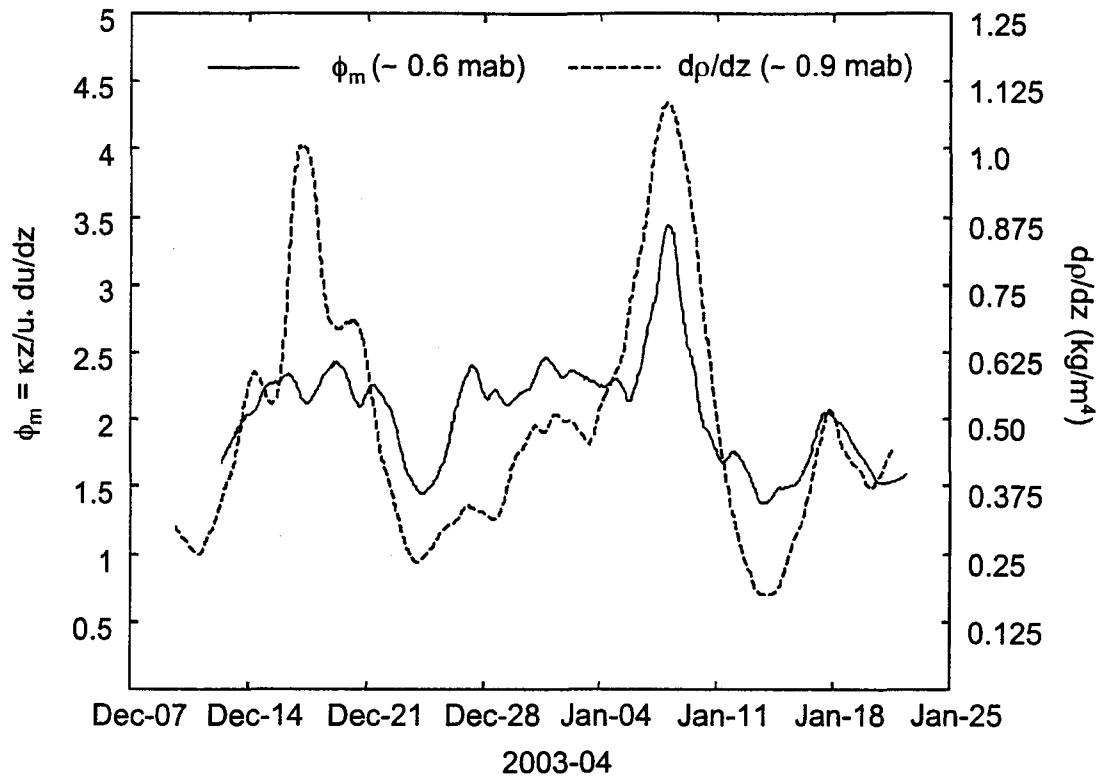


Figure 2-5. Smoothed time-series of ϕ_m measured 0.6 mab (solid line) and density stratification measured 0.89 mab (dashed line), both at channel site.

percent window, after excluding all negative values. As a result, roughly 20 percent of the data were excluded before smoothing, mainly during periods of low current velocity. The smoothed time-series of φ_m was compared to the time-series of the vertical density stratification measured between the two adjacent CTDs that were closest in height to the mean height of the two functioning ADVs deployed at the channel site. Because of instrument noise and periodic erroneous measurements, and consistent with the time-series measurements of φ_m , the time-series of stratification was smoothed using a 8 percent lowess filter after excluding all values which reported unstable density stratification. Consistent with previous authors, we found a positive correlation between the departure from the law of the wall and the local density stratification ($r = 0.76$).

It follows from the analysis of the boundary layer shear at the channel site that the increased stratification on ebb due to tidal straining resulted in an intensification of ebb velocities. As seen in Table 2-1, the depth averaged ebb current magnitude is greater on average than the current magnitude on flood at the channel site. However, there was no strong lateral asymmetry in current magnitudes at peak flood or peak ebb, even during spring tides, when strong lateral shear was observed. This indicates that the preferential down-estuary flow at the channel site was driven by lateral asymmetries in the duration of flood and ebb tides. The depth-averaged currents were ebb directed over 57% of the time at the channel site, compared with roughly 52% of the time at the shoal site. This pattern was even more pronounced during spring tidal conditions (Table 2-1). This lateral asymmetry in duration can be seen more clearly by examining an average tidal cycle representation of the depth-averaged currents at both sites. The average tidal cycle representation was calculated by dividing the entire time series into sections of length

equal to the M_2 tidal period and then averaging all values with the same relative tidal phase. Figure 2-6a shows the average tidal cycle values for the depth-average currents at both sites for the entire experiment. From this view, the lateral asymmetry in duration is clear. At the channel site the ebb tide was consistently longer than the ebb observed at the shoal site. This occurs because the transition from ebb to flood occurred much later at the channel site than at the shoal site, while the transition from flood to ebb occurred more simultaneously at both locations.

The delay in the reversal of the ebb directed currents at the channel site appears to have been caused by tidal asymmetries in turbulent mixing that result from tidal straining of the axial density gradient. To examine the tidal variability of the data, the average tidal cycle values of stratification at the channel site are plotted in Figure 2-6b.

Consistent with the classic view of tidal straining, stratification generally increased throughout the ebb tide, and decreased during the flood (Fig. 2-6b). While the ebb values of stratification were greater on average than those on flood, the greatest asymmetry occurred between the end of ebb and the end of flood. The increased stratification at the end of ebb significantly reduced the internal friction and provides an explanation for delay in onset of the flood tide at the channel site.

The tidal variations in the degree of bottom friction can be represented using a drag coefficient given as:

$$C_D = \frac{\tau_b / \rho}{u|u|} \quad (2-5)$$

where u is the velocity measured by the ADV 1.1 mab and τ_b is calculated from the ADV data following (2-1). Figure 2-6c shows the average tidal cycle values of C_D for the entire deployment. There was a decrease in C_D during the ebb tide, reaching a minimum

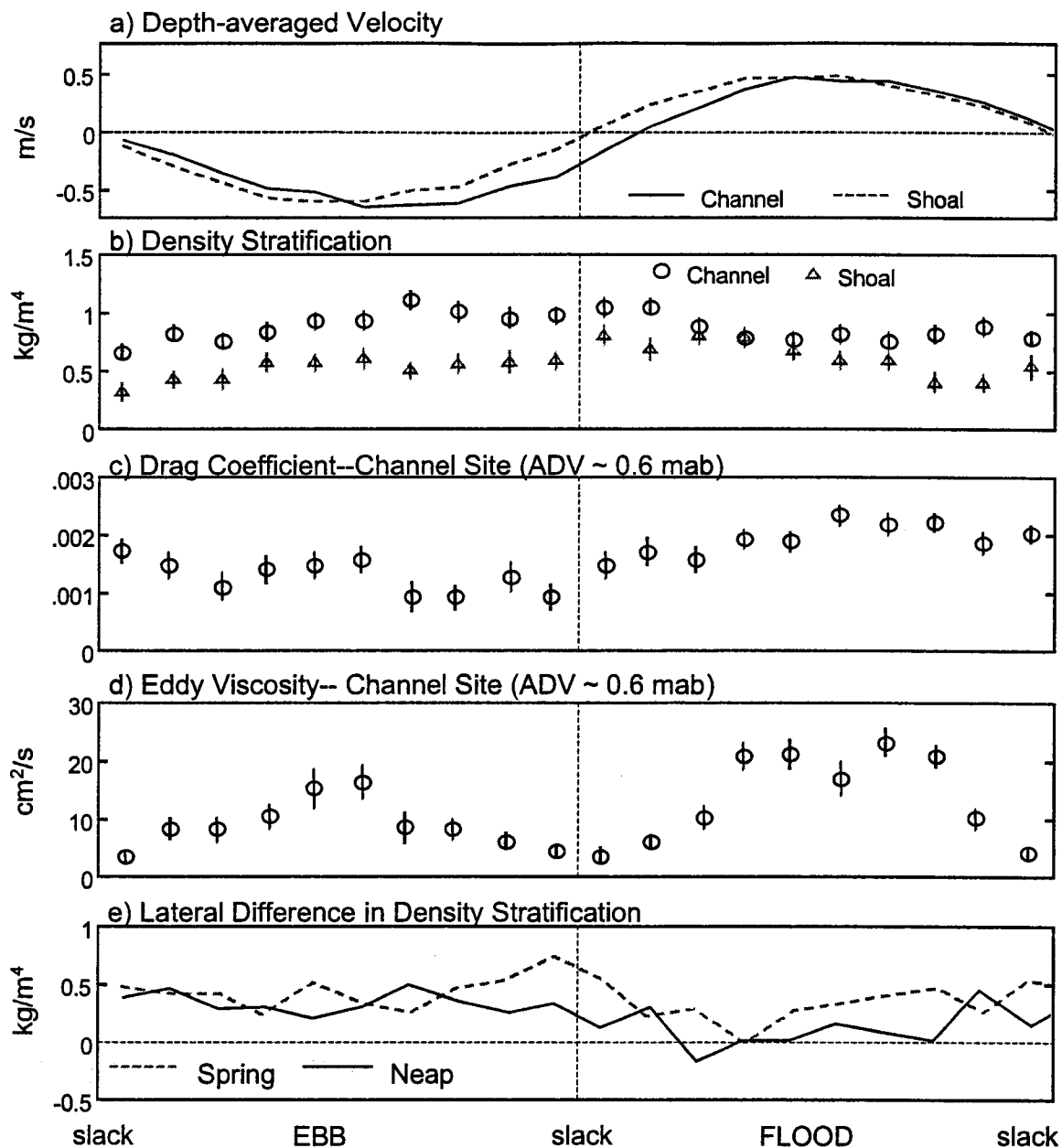


Figure 2-6. Average tidal cycle values of a) depth averaged current velocities (dark line the channel site and dashed line the shoal site); b) density stratification at the channel site (circles) and shoal site (triangles); c) drag coefficient calculated from ADV data at channel site; d) eddy viscosity measured by ADVs 0.6 mab at channel site; e) the lateral difference in stratification obtained by subtracting stratification measured at the shoal site from the channel site, for neap (solid line) and spring (dashed line) conditions. Vertical lines represent one standard error.

value at the end of ebb. During the flood, the drag coefficient generally increased, reaching a maximum value near the end of flood. From this view, the drag coefficient was only slightly greater on flood than on ebb in the average sense. However C_D was over twice as large at the end of flood (0.002) than the end of ebb (0.0009). This pattern is consistent with tidal variations in stratification at the channel site and the general pattern of stratification expected due to tidal straining.

The vertical velocity shear and stress measured by the ADV sensors was used to calculate the eddy viscosity, given as:

$$A_z = \frac{\langle u' w' \rangle}{du/dz} \quad (2-6)$$

Similar to the data presentation for the drag coefficient, the average tidal cycle values of the eddy viscosity are presented in Figure 2-6d. As one might expect, the average tidal cycle values of eddy viscosity exhibited a strong M_4 tidal signature. However, there was also a notable tidal asymmetry in the values of A_z , with substantially higher values occurring during the flood phase of the tide. This was despite the fact that the residual current was ebb directed at this location, which should favor greater values during the ebb phase of the tide. Consistent with the pattern of stratification and the tidal variations of the drag coefficient, the tidal asymmetry in eddy viscosity was most pronounced between the later half of flood and ebb.

Although no direct measurements of stress were collected at the shoal site, the instruments deployed at this location provide detailed measurements of density stratification. In general, the shoal site was less stratified than the channel site, consistent with the shallower bathymetry adjacent to the shoal site. Similar to the channel site, stratification at the shoal site generally increased throughout the ebb tide. However, this

increase continued into the flood and did not begin to decrease until slightly before the maximum flood current (Fig. 2-6b). As a result of this pattern, the flood tide was more stratified on average than the ebb at the shoal site. Because of the strong relationship between the degree of density stratification and the internal friction at the channel site, it is useful to compare the lateral differences in stratification between the two locations during the tidal cycle.

Figure 2-6e plots the lateral difference in stratification between the two sites as a function of tidal phase. The data for spring and neap tidal conditions are plotted separately. The lateral difference in stratification was greater during spring tides than it was during neaps even though the overall level of stratification was greater at both locations during neap. In addition, during spring tides the greatest difference in stratification occurred between the two locations at the end of ebb. At the channel site, stratification increased throughout the ebb, but at the shoal site mixing during spring tidal conditions appears to have been sufficient to reduce stratification during the second half of ebb. Given the relationship between stratification and turbulent mixing observed during this experiment, one can conclude that the greatest lateral asymmetry in internal friction occurred during the later half of the ebb tide during spring tidal conditions.

The impact of this inferred lateral difference in internal friction can be seen in figure 2-7, where the depth integrated barotropic pressure gradient is plotted against the depth integrated transport for both sites. If the pressure gradient were balanced solely by friction, the data in figure 2-7 would fall roughly on a straight line, while a frictionless balance between the pressure gradient and acceleration would appear as a circle. The most noticeable difference between the two sites occurred during the second half of the

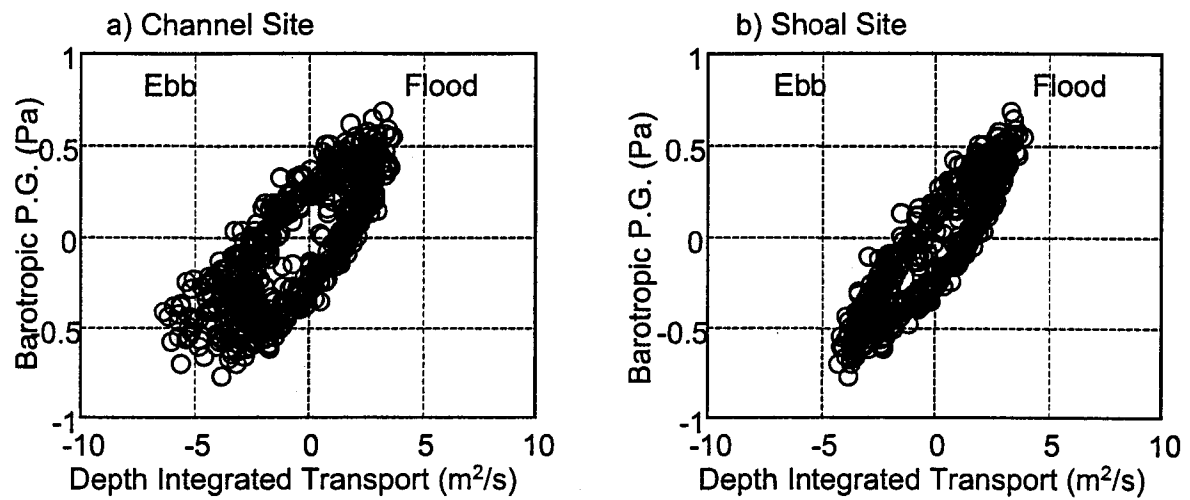


Figure 2-7. Depth integrated transport measured by the ADCP at the channel site (a) and ADP at the shoal site (b) plotted against the estimate of the depth integrated barotropic pressure gradient.

ebb tide, when the transport values at the channel site fall to the left of those for the shoal site. These data coincided with spring tidal conditions and mostly occurred during the period of 21-28 December 2003, when the strongest lateral shear was observed. The data in Figure 2-7 suggest that there was less friction to balance the pressure gradient during the later half of ebb at the channel site as compared to the shoal site.

2.3.2 Momentum Balance

Although there were no direct measurements of stress at the shoal site, the stress at this location was estimated from the dominant terms in the momentum balance, as discussed above. Integration of (2-2) gave an estimate of the bed stress that could be compared with a quadratic drag representation of bed stress as expressed by (2-5). In general, the momentum estimate of near-bed stress was well correlated with the quadratic bottom velocity (Fig. 2-8). The correlation coefficient, r , was 0.70 and 0.82 for the channel and shoal sites, respectively. However, there appeared to be both lateral and tidal asymmetries in the relationship between bottom velocity and bottom stress. These asymmetries can be seen clearly in the estimates of the drag coefficient. The drag coefficient was calculated using a least squares regression between the quadratic velocity and the momentum estimate of the bed stress. Flood and ebb data were treated separately and the regression was forced through the origin.

Consistent with ADV measurement, this analysis suggests that C_D was consistently greater during the flood than the ebb tide at the channel site (0.0019 and 0.0011, respectively). At the shoal site, the tidal asymmetry was less pronounced and had the opposite sense, with a slightly lower C_D on flood as compared to ebb (0.0023 and 0.0026, respectively). This asymmetry is consistent with the overall greater degree of

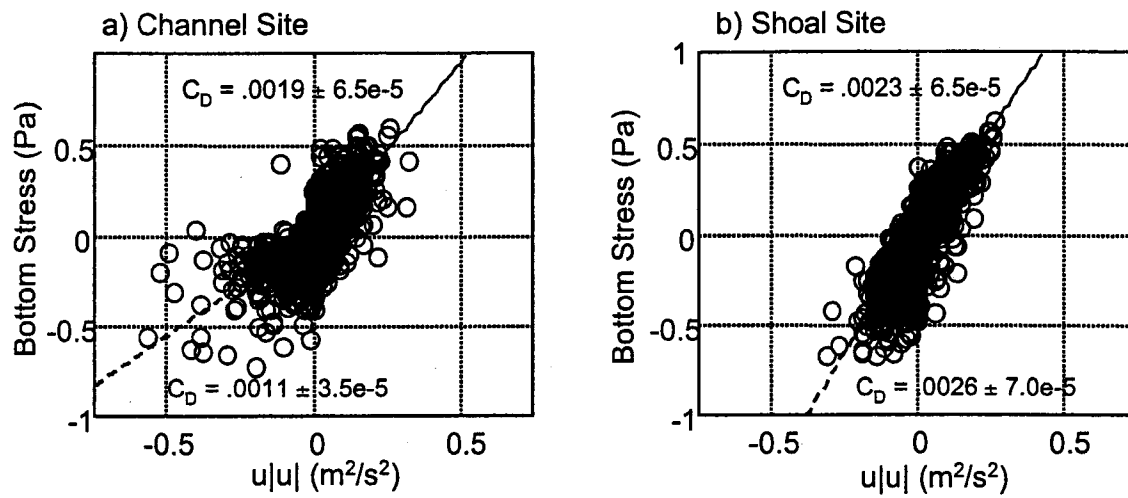


Figure 2-8. Scatterplot of estimated bed stress from the momentum integral and the quadratic velocity measured 1.4 mab for both channel and shoal sites. Values of C_D are derived from least squares regression of the data.

stratification observed at the channel site, as well as the patterns of tidal asymmetry in stratification that were observed. In addition to the tidal asymmetry in C_D , there were important lateral asymmetries as well. This was particularly evident during the ebb phase of the tide. While the estimate of C_D during ebb was significantly greater at the shoal site than the channel site, the difference was much less pronounced during the flood phase of the tide. This pattern of lateral asymmetry is consistent with the observations that showed the tide reversing from ebb to flood significantly later at the channel site than the shoal site, but currents reversing from flood to ebb more simultaneously.

By using the momentum estimate of stress and the observed vertical velocity shear, profiles of the vertical eddy viscosity were estimated from Equation (2-6). Figure 2-9 shows the estimates of the median vertical profiles of eddy viscosity for the two sites. The data were segregated by the phase of the tide as well as spring and neap tidal conditions. Depth averaged values of eddy viscosity derived from the momentum balance (Table 2-1) are consistent with tidal and lateral asymmetries in stratification. In general, values of eddy viscosity were higher during spring tidal conditions and greater at the shoal site than at the channel site. At the channel site, where stratification was greater on average on the ebb phase of the tide, the depth averaged eddy viscosity was consistently greater on flood as compared to ebb. The shoal site generally demonstrated the opposite pattern, consistent with the observed stratification at that location. Although tidal and lateral asymmetries were relatively weak during neap conditions, large asymmetries were present during spring tidal conditions. At the channel site, the depth averaged eddy viscosity was nearly twice as large during the ebb as during the flood, despite strong down estuary flows during this period. No significant tidal asymmetry was

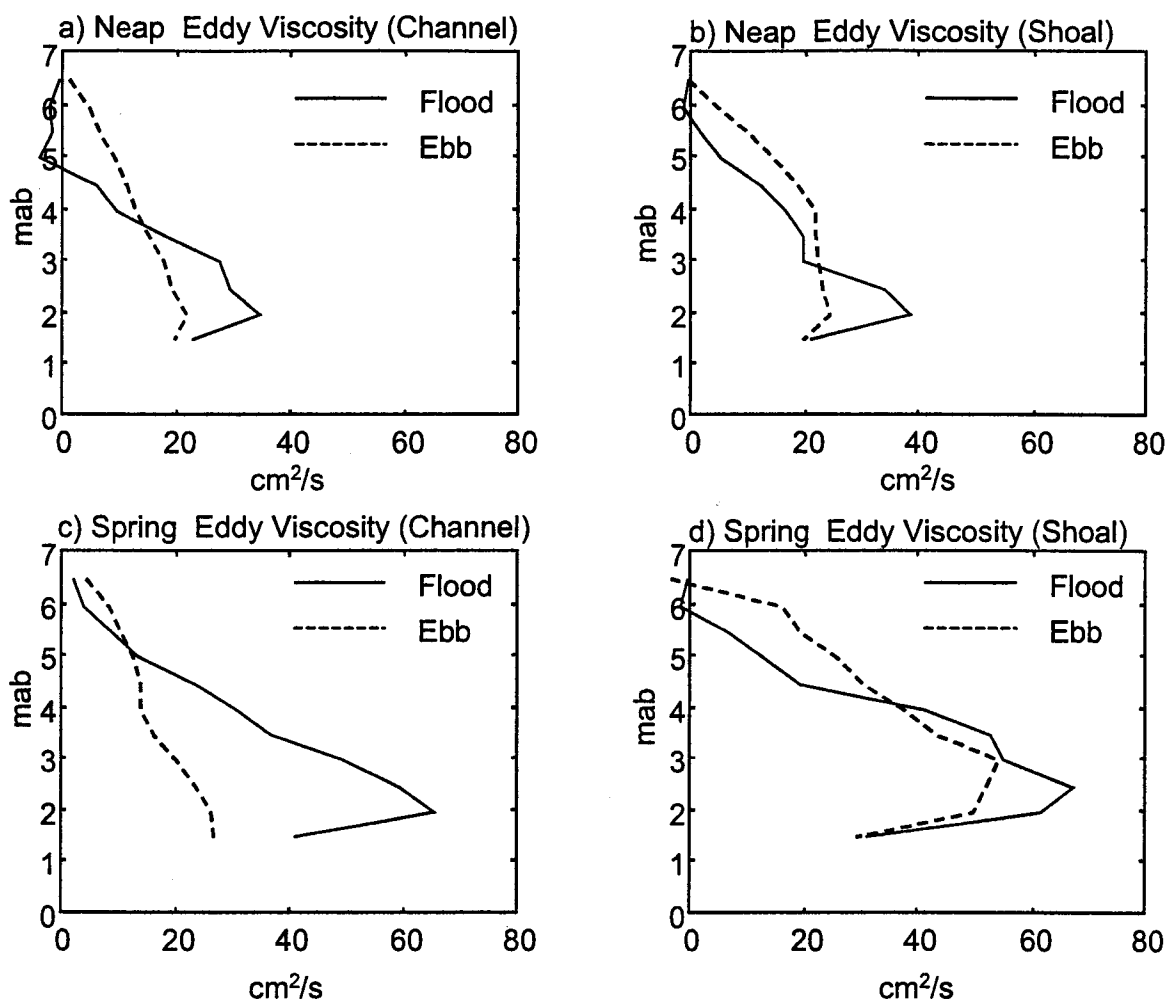


Figure 2-9. Median profiles of the eddy viscosity estimated from the momentum integral for both channel and shoal sites during spring and neap tidal conditions (solid line denotes flood and dashed line denotes ebb).

present at the shoal site, which lead to a strong lateral asymmetry during the ebb phase of the tide.

The estimates of eddy viscosity from the momentum balance also were compared with the measured values from the ADVs at the channel site. Figure 2-10 shows a comparison between the time-series of eddy viscosity measured by the ADV 0.6 mab and the momentum estimate of eddy viscosity that corresponds to the lowest bin of the ADCP (1.4 mab). Because there was noise in both the direct measurement and momentum estimate of eddy viscosity, especially near periods of low current magnitude, both time-series were smoothed using a lowess filter with an 8 percent data window. Before the smoothing was performed, all negative values and all values that exceed the maximum expected value for an unstratified boundary layer (i.e. $\kappa u_* z$) by more than 20 percent were removed. As a result, roughly 80 percent of the data were used for both the direct measurement and the momentum estimate of eddy viscosity. The relatively high correlation between the time series of these two estimates of eddy viscosity provides confidence that the estimates of stress from the momentum integral are meaningful.

2.3.3 1-D Modeling Results

To more clearly illustrate the creation of residual flows due to internal asymmetries in mixing, a relatively simple numerical experiment was conducted using the 1-dimensional General Ocean Turbulence Model (GOTM). GOTM was run employing a k-epsilon turbulence closure scheme as described by Burchard and Bolding (2001) with the stability parameters of Canuto et al. (2001). The model was used to simulate a simple tidal flow, forced by a tidally varying barotropic pressure gradient and a depth invariant along-channel salinity gradient ($dS/dx = 3e-4 \text{ m}^{-1}$). The model was run

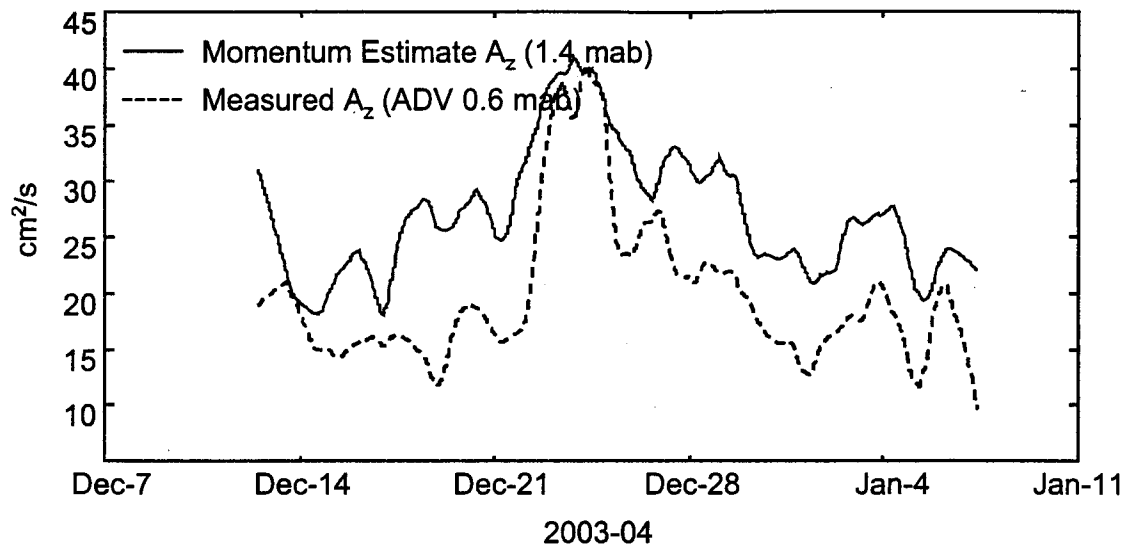


Figure 2-10. Smoothed time-series of the eddy viscosity at the channel site estimated from the momentum integral 1.4 mab (solid line) and by ADVs 0.6 mab (dashed line).

for a depth of 10m, roughly consistent with the main channel of the York River, as well as a depth of 5m, generally consistent with the shoal region of the York River. A net seaward-directed barotropic pressure gradient was added so that the sum of the tidally-averaged transport for the two depths resulted in no net volume transport. The net barotropic pressure gradient was imposed assuming that the shoal area (5 meters deep) and the channel area (10 meters deep) had equal cross-sectional areas, a pattern generally consistent with the bathymetry of the York River.

The model predicted a time-varying pattern of stratification where stratification was generally created during ebb and destroyed during flood at both the channel and shoal locations (Fig. 2-11a). The greatest stratification was predicted when velocity near the bed began to flood and the upper water column was still ebbing. This processes created significant stratification at the end of ebb that persisted into the flood, and a result the flood tide was slightly more stratified on average than the ebb for the 10-meter simulation. However, the time varying pattern of stratification predicted by the model exhibited the key feature that the end of ebb was significantly more stratified than the end of flood. Additionally, the stratification predicted over the lower half of the water column was over twice as large during the ebb, on average, as compared to the flood for the 10-meter simulation. The overall degree of stratification was lower for the 5m location relative to the deeper 10m location because, unlike at the deeper location, boundary layer mixing at the shallow location was capable of reaching all the way to the surface. As a result of the tidal asymmetry in stratification and internal mixing, the eddy viscosity was greater during the flood than during ebb (Fig. 2-11b). While this asymmetry was predicted at both the channel and shoal sites, it was more pronounced at

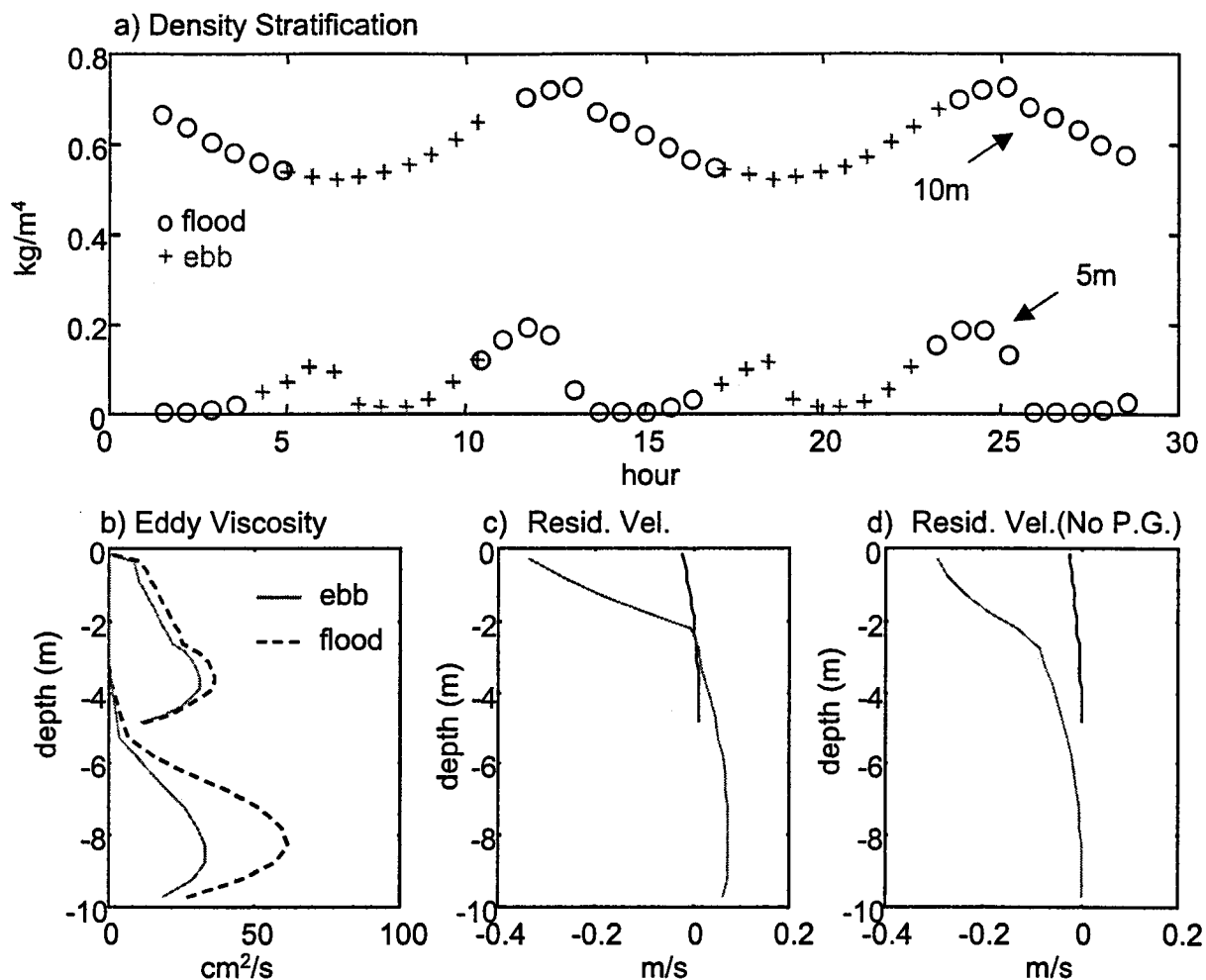


Figure 2-11. Results from 1-D turbulence model runs: a) time series of salinity stratification predicted by the model for depths of 5m and 10m (circles represent flood tide and crosses represent ebb tide); b) median eddy viscosity profiles from model run with baroclinic and net ebb-directed barotropic pressure gradient (dashed lines represent flood tide and solid lines represent ebb tide); c) along-channel residual velocity profile for model run with baroclinic and net ebb-directed barotropic pressure gradient; d) along-channel residual velocity profile for model run with no baroclinic or net barotropic pressure gradient.

the deeper location. Large lateral asymmetries in eddy viscosity in the upper portion of the water column were predicted, largely due to the inviscid conditions predicted in the upper water column at the channel site.

The profiles of residual circulation predicted by the model (Fig. 2-11c) are largely consistent with the observations from the York River. Relatively strong down-estuary residual circulation was predicted over the upper portion of the water column for the channel location, relative to the shoal site. The depth averaged residual circulation was down-estuary over the channel and up-estuary over the shoal despite the stronger integrated baroclinic forcing associated with the deeper location. Although the predicted ebb velocities at the channel location are larger than both the flood velocities at the channel and the ebb velocities on the shoal, much of the down-estuary residual at the channel site is caused by longer relative duration of the ebb tide. Consistent with the observations, both the lateral and vertical phase differences were significantly larger during the transition from ebb to flood than during the transition from flood to ebb. This is largely a consequence of the reduced internal friction at the end of ebb caused by tidal straining of the density field, which delays the onset of the ebb tide in the channel.

It is important to note that in order to have zero net flow through the estuarine cross-sections over the tidal cycle it was necessary to impose a net ebb-directed barotropic pressure gradient. This is consistent with the classic view of estuarine circulation as demonstrated by the analytical solution of Officer (1976). However, the pattern of tidal asymmetries in the vertical density stratification, which lead to increased vertical velocity shear during the ebb tide, reduced the net barotropic pressure gradient significantly from the value predicted analytically. In fact, the net ebb-directed

barotropic pressure gradient necessary to ensure no net volume transport through the cross-section was nearly 70 percent smaller than that predicted based on the Officer (1976) solution.

The role that tidal asymmetries in mixing play in the modification of the net barotropic pressure gradient can be clearly demonstrated with another simple numerical experiment. The model was next run imposing the time varying salinity field from the first model run, but artificially setting the baroclinic pressure gradient to zero. To highlight the role of asymmetries in mixing, no net barotropic pressure gradient was used. The resulting residual circulation profiles are presented in Figure 2-11d. Clearly the time varying pattern of stratification leads to strong down-estuary residual flows, as no baroclinic or net barotropic pressure gradient forcing was used in this simulation. Of course in a real estuary, the net barotropic pressure gradient would adjust to account for this net volume transport in order to conserve mass. The important role that tidal asymmetries in mixing have on the residual velocity is demonstrated in the profiles shown in Figure 2-11d, which have nearly the same vertical form as those presented in Figure 2-11c despite no baroclinic forcing. This result suggests that the two-layer structure of the residual estuarine circulation is driven largely by the interaction of tidal asymmetry and the barotropic tide. The along-channel density gradient is necessary to create the asymmetries in stratification that drive this process, however, the process itself is largely barotropic in nature.

2.4 DISCUSSION

Previous studies have demonstrated that tidal asymmetries in mixing caused by tidal straining can enhance the vertically sheared residual estuarine circulation (Jay and

Smith, 1991; Stacey et al., 2001). However, these studies were conducted in sections of the Columbia River and northern San Francisco Bay where the lateral bathymetry is relatively uniform. In such systems, it is likely tidal asymmetries in stratification, and hence tidal asymmetries in mixing, act more or less uniformly across the estuary. As a result, the enhanced volume transport caused by the increased velocity shear on the ebb tide modifies the residual barotropic pressure gradient, leading to a vertically segregated two-layer flow, even in the absence of a baroclinic pressure gradient. However, many drowned river valley estuaries, such as the York River, have extensive shoal areas adjacent to the deeper channel region. The interaction of this morphology with density stratification can result in lateral asymmetries in turbulent mixing as well as tidal asymmetries. In such systems, it is unlikely that tidal asymmetries in stratification act uniformly on the estuarine cross-section. Because the barotropic pressure gradient responds to the integrated transport through the entire estuarine cross-section, while the vertical velocity shear responds locally to the degree of turbulent mixing, distinct laterally sheared residual flows can develop in systems that exhibit both tidal and lateral asymmetries in mixing. From the data collected in the York River, the strongest tidal and lateral asymmetries in mixing appear to occur during spring tidal conditions. Although tidal asymmetries are apparent during neap conditions, the lack of lateral asymmetry prevents the lateral shear in the residual circulation, and the response is a vertically sheared residual similar to the results of Jay and Smith (1991) and Stacey et al. (2001).

A spring-neap modulation in lateral shear also was recently documented by Winant and Gutierrez de Velasco (2003) in a study of the Laguna San Ignacio (LSI), an inverse estuary on the Pacific coast of Baja California. In their study, the pattern of

residual inflow and outflow switched from vertically to horizontally sheared in conjunction with the spring-neap cycle and was well correlated with the internal Froude number (Fr). Although they reported laterally sheared flows with outflow over the shoals with inflow over the deeper channel, their results are consistent with the observations from York River because of the opposite sense of the axial density gradient in LSI. A reversed axial density gradient would lead to the opposite sense of tidal straining and associated tidal asymmetries in turbulent mixing. The authors attributed the pattern of residual circulation at LSI to nonlinear advection ($u \, du/dx$), in order to explain the strong correlation between the mode of shear in the residual circulation and Fr . However, their observations also are consistent with the patterns described in this chapter, and the correlation between the laterally sheared exchange flow and high Fr in LSI may at least partly be the result of lateral asymmetries in mixing.

Unlike the results of Winant and Gutierrez de Velasco (2003), the progressive nature of the tidal wave and the relatively uniform along-channel bathymetry in the region of the York River examined here make it unlikely that advection of along-channel momentum ($u \, du/dx$) plays a significant role in driving residual circulation. However, the modeling results of Lerczak and Geyer (2004) suggest that the advective terms driven by lateral circulation ($v \, du/dy$ and $w \, du/dz$) can play an important role in the along-channel momentum balance and drive the two-layered estuarine exchange flow in well-mixed estuaries. Similar to the results of Lerczak and Geyer (2004), the pattern of lateral circulation inferred from our data suggest that these advective terms would enhance the residual inflow near the bed in the channel, particularly during spring tides. This is opposite from the pattern of along-channel residual velocity observed during this

experiment and is not consistent with the mechanism described by Lerczak and Geyer (2004).

The pattern of circulation with inflow over the shoals and outflow over the channel has been documented in numerous estuarine systems. However, this mode of circulation is usually associated with shallow, macro-tidal systems (Robinson, 1960; Charlton et al., 1975; Uncles and Stephens, 2000). In these systems, the residual pattern of circulation is thought to be driven largely by tidal non-linearities that arise as the tidal wave propagates into the system, favoring inflow over the shallower shoal regions. This process was addressed explicitly by Li and O'Donnell (1997), who used an analytical model to quantify the tidal rectification of Stokes drift. Although Li and O'Donnell (1997) documented relatively strong residual flows due to this mechanism, Friedrichs and Hammrick (1996) included this process in their analytical model and found that it made only a minor contribution in the micro-tidal James River. Using the velocity and pressure observations collected during this experiment and following the methods of Friedrichs and Hammrick (1996), we estimated the residual velocity due to Stokes drift in the York River was only on the order of 1 cm/s.

While the lateral distribution of residual circulation described in this chapter is typically attributed to shallow macro-tidal estuaries or tidal inlets (Kjerfve, 1978), it has been observed or inferred from modeling studies in a number of estuaries with similar characteristics to the York River, including the upper Chesapeake Bay (Wang and Chao, 1996) and the Hudson River (Hellweger et al., 2004). Li et al. (1998) attempted to separate the barotropic and baroclinic components of the residual circulation in the James River and found the barotropic residual to exhibit outflow over the channel with inflow

on the shoals. Their identification of the barotropic residual was kinematic and they did not identify the physical mechanism driving this flow. However, the James River is dynamically similar in many ways to the York River, and the barotropic residual described by Li et al. (1998) is consistent with the mechanism described in this chapter. While this mechanism is related to asymmetries in stratification caused by tidal straining of the along-channel density gradient, it is a barotropic process nonetheless. Separating baroclinic and barotropic components from a residual flow is difficult. Because of its strong dependence on depth, the baroclinic pressure gradient will act to offset the pattern of residual circulation documented in this chapter. As such, this barotropically-driven pattern of residual circulation may be difficult to identify in some systems

2.5 CONCLUSIONS

This study demonstrates the importance of asymmetries in mixing associated with tidal straining to residual estuarine circulation. The presence of stratification causes the shear in the boundary layer to deviate from the expected law of the wall relationship. This deviation is strongly correlated with the strength of the observed density stratification. As a result, tidal asymmetries in stratification lead to increased shear during the more stratified phase of the tide. When the classic pattern of tidal straining is observed, the increased shear during the ebb tide favors down-estuary transport that must be balanced barotropically in order to conserve mass over the tidal cycle. When tidal asymmetries act uniformly across an estuary and there are no significant lateral gradients in turbulent mixing, this will result in a vertically segregated two-layered exchange flow as described by Jay and Smith (1991). However, many drowned river valley estuaries have channel-shoal bathymetries that lead to lateral variability in density stratification

and turbulent mixing. As a result, tidal straining can significantly increase density stratification during the ebb tide over deeper areas, while shallower areas remain relatively well mixed. This results in large lateral variations in internal friction, causing the tide to turn from ebb to flood considerably earlier on the shoals than in the channel. This increases the duration of the ebb tide over the channel and favors down-estuary residual flow that is balanced by residual inflow over the shoals.

CHAPTER 3

TIDALLY-DRIVEN EKMAN FLOWS IN A SHALLOW STRATIFIED ESTUARY

3.1 INTRODUCTION

While many studies of estuarine processes focus on the longitudinal dynamics, estuarine flows are fundamentally three-dimensional in nature. The interaction of the axial and lateral flows plays an important role in the diffusive processes acting in estuaries (Fisher, 1972; Scott, 1994). Thus, knowledge of the lateral dynamics in estuaries is fundamentally important to understanding the transport of momentum, salt, sediment, and many biologically important materials. Many of previous studies on lateral processes in estuaries have focused on the sub-tidal dynamical balance. In his pioneering work in the James River, Pritchard (1956) suggested that the non-tidal lateral balance was predominantly geostrophic. A similar balance was presented by Larouche et al. (1987) who found that the nontidal baroclinic and barotropic pressure gradients contribute at the same order.

While these results suggest that frictional stress is not dynamically important to the sub-tidal lateral balance, a number of authors working in well-mixed systems provide evidence for its importance. Consistent with the classical view of the sub-tidal longitudinal estuarine dynamics (e.g. Officer, 1976), a number of authors have suggested the lateral dynamics are a balance between the baroclinic and barotropic pressure gradient and the internal friction (Smith, 1976; Nunes and Simpson, 1985). More recently, observations collected in the James River suggest that both friction and non-linear advection contribute significantly to the lateral sub-tidal balance, and their relative importance showed significantly fortnightly variability. (Valle-Levinson et al., 2000).

While these studies provide significant insight into the lateral dynamics, studies examining the dynamics at tidal time-scales are necessary to fully understand the diffusive transport processes fundamental to estuarine dynamics. Observational studies examining the tidal dynamics have been carried out in a number of estuarine systems with significant curvature. In a stretch of the Hudson River that flows around a headland, Chant and Wilson (1997) found that the centrifugal acceleration was mostly balanced by the cross-stream baroclinic pressure gradient under stratified conditions. Similar findings were presented by Seim and Gregg (1997), in Puget Sound when streamwise currents were below 0.75 m/s. Lacy and Monismith (2001) did not find a similar balance in the northern San Francisco Bay because the short travel time around the bend did not allow this steady balance to develop. Although they did not close the lateral balance, they found that the advective acceleration terms were of first order importance to the streamwise momentum balance.

The response of the baroclinic pressure gradient to channel curvature clearly exerts an important control on lateral estuarine dynamics. Even in the absence of curvature, the tidal baroclinic pressure gradient plays a fundamental role in the lateral balance. In shallow frictional systems, the lateral baroclinic pressure gradient is usually assumed to be driven by differential advection of the longitudinal density gradient leading to the commonly observed axial fronts during the flood tide (Nunes and Simpson, 1985; Huzzey and Brubaker, 1988). However, recent work has demonstrated that baroclinicity driven by the interaction of lateral circulation with vertical density stratification can play an important role in the lateral dynamics of stratified systems (Lerczak and Geyer, 2004). When rotation was included in their model simulations,

Lerczak and Geyer (2004) found that the tidal lateral balance was mainly geostrophic. The lateral tilt of the isohalines and the longitudinal vertical shear (du/dz) were largely in balance according to the thermal wind balance.

Despite the significant work examining lateral dynamics in estuaries, there are surprisingly few observational studies that specifically look at the tidal lateral dynamics in straight estuaries. In this paper, we examine the lateral dynamics in the York River Estuary during relatively stratified conditions. The study site and observational methods are detailed in section 3.2 and the observational results are presented in section 3.3. A simple analytical two-layer reduced-gravity model for the lateral tidal dynamics in a stratified estuarine system is presented in section 3.3.3 and compared with observations. The results are discussed in section 3.4 and conclusions are presented in section 3.5.

3.2 OBSERVATIONS AND METHODS

3.2.1 Study Site

The York River is a partially-mixed sub-estuary of the Chesapeake Bay that forms at the confluence of the Mattaponi and Pamunkey Rivers (Fig. 3-1). Most of the York River is characterized by a main channel with an approximate depth of 10 m, flanked by broad shoals with a mean depth of approximately 4 m. The main portion of the mesohaline York River below the confluence of the Mattaponi and Pamunkey Rivers and above Gloucester point is relatively straight, with little or no curvature. Although the mean tidal range is only about 0.7 m, tidal currents are energetic with surface currents exceeding 1 m/s during spring tidal conditions. Both salinity and temperature exhibit significant seasonal variability, however the density gradient is nearly always dominated by gradients in salt. The vertical density stratification varies significantly on tidal,

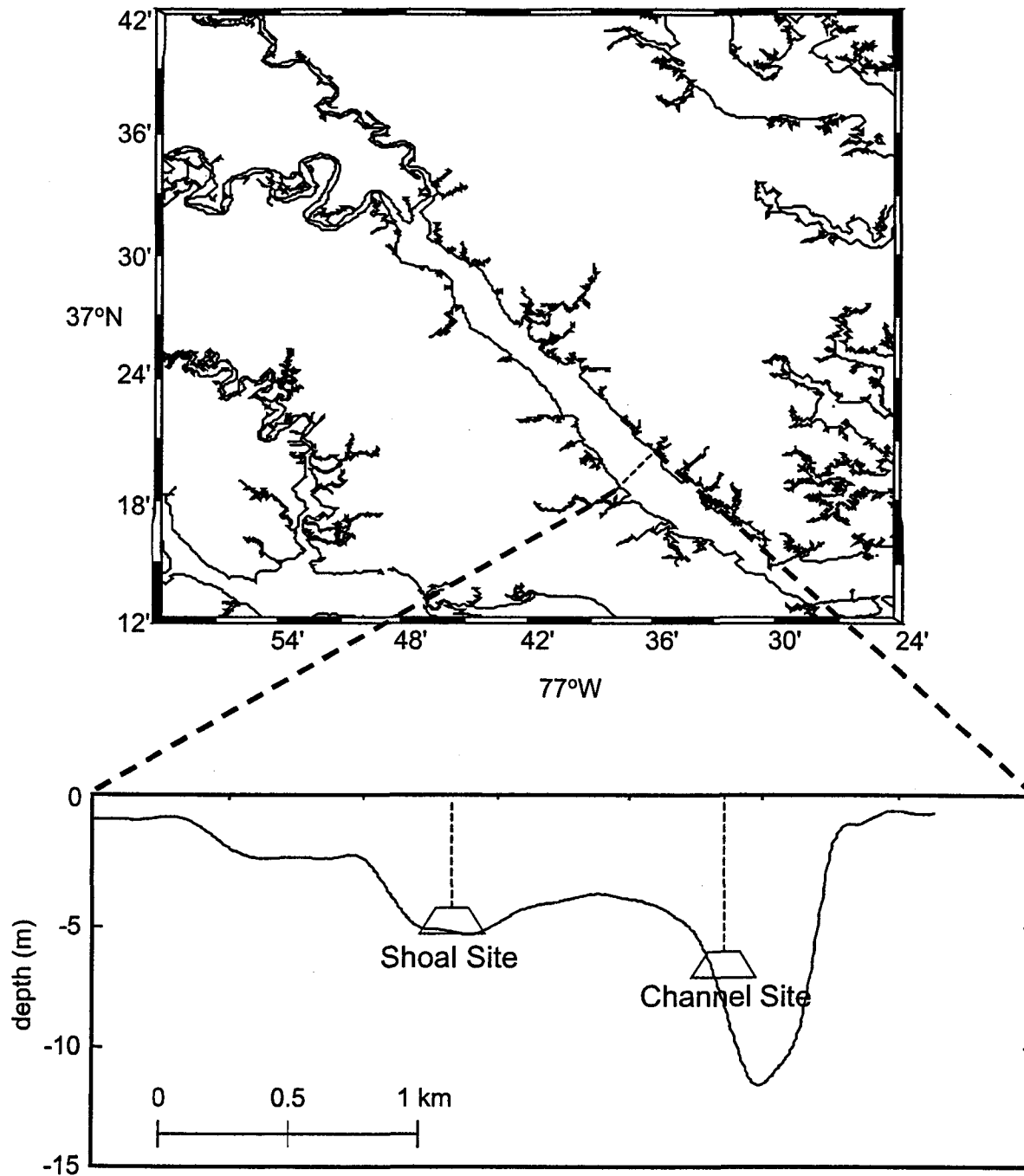


Figure 3-1. Map of study area, York River Estuary, Virginia with estuarine cross-section at the "channel" and "shoal" deployment locations.

fortnightly, and synoptic time scales (Haas, 1976; Sharples et al. 1994; Scully et al. 2005). Under high river discharge conditions ($> 200 \text{ m}^3/\text{s}$ combined discharge) the estuary can be strongly stratified, with bottom to surface salinity differences of greater than 15 psu. Under normal to low river discharge conditions ($\leq 40 \text{ m}^3/\text{s}$ combined discharge) the estuary varies between partially-mixed and well-mixed conditions.

3.2.2 Observations

During the winter of 2003-04, instrumentation was maintained at two laterally adjacent locations in the estuarine cross-section near Clay Bank, located roughly 13 kilometers up-estuary from Gloucester Point. At this location in the York River, the main channel of the estuary is located on the northeastern side of the river with a maximum depth of approximately 10 m. A broad shoal extends to the southwest of the main navigational channel with a maximum depth of approximately 6.5 m. Instruments were deployed along the southwestern side of the main channel at a water depth of approximately 7 m (“channel” site) to avoid interfering with navigation, and at the deepest location within the southwestern shoals at a water depth of roughly 6 m (“shoal” site).

The instrumentation deployed during this experiment has been described in detail in both chapters 2 and 3. The reader is referred to these previous chapters for the details. However, for clarity the main instrumentation discussed in this chapter is outlined below. Vertical profiles of velocity were collected by an RDI 1200 kHz acoustic Doppler current profiler (ADCP), at the channel site and a Sontek 1500 kHz acoustic Doppler profiler (ADP) at the shoal site. The ADCP collected vertical profiles of current velocity in 0.50 m bins. It sampled at roughly 1 Hz and collected one 10-minute burst every hour. The

ADP deployed at the shoal site sampled at a rate of 1 Hz averaged over one minute bursts to provide vertical profiles of current velocity in 0.25 m bins.

Three YSI 6000 conductivity, temperature and depth sensors (CTDs) were mounted on a tripod at the channel site at 0.10, 0.41, and 1.4 mab and collected pressure, salinity, and temperature every 30 minutes. A mooring that consisted of a YSI 6000 CTD and an InterOcean S4 current meter, outfitted with a CTD was located immediately adjacent to the tripod at the channel site. The CTD and S4 on the mooring were located 2.8 and 3.4 mab, respectively. At the shoal site, two YSI 6600 CTDs located 0.10 and 1.5 mab and an InterOcean S4 sensor with a CTD located 3.5 mab were deployed immediately adjacent to the ADP. In addition to the instrumentation outlined above, the tripods at the both the channel and shoal location were equipped with Sontek pulse-coherent acoustic Doppler Profilers (PC-ADPs). Each PC-ADP was mounted approximately 1 mab in a downward looking configuration to measure the near-bed current velocities and was equipped with a strain gage pressure sensor. Although we used the pressure data from the PC-ADPs the velocity data from these sensors will not be discussed in this paper. The PC-ADPs collected 15 minute bursts every 30 minutes and sampled at 1 Hz. Although the manufacturer's reported resolution for the pressure sensor is only on the order of 1.0 cm, the pressure readings were averaged over each burst ($n = 900$) reducing the standard error substantially. In fact, the standard error from each burst averaged over the entire deployment is approximately 0.4 mm. Using this large averaging duration gives us confidence in the pressure estimates collected during the experiment.

3.2.3 Momentum Balance

The primary focus of this paper is to examine the tidal, lateral dynamical balance.

In a straight estuary this can be represented as:

$$\frac{dv}{dt} - fu + u \frac{dv}{dx} + v \frac{dv}{dy} + w \frac{dv}{dz} = -g \frac{d\eta}{dy} + \frac{g}{\rho_o} \int \frac{d\rho}{dy} dz + \frac{1}{\rho_o} \frac{d\tau}{dz} \quad (3-1)$$

where u is the axial velocity (positive landward), v is the lateral velocity (positive to the right of positive u), w is the vertical velocity (positive upward), g is gravitational acceleration, f is the coriolis parameter, η is the sea surface height, ρ water density and τ is the Reynolds stress. Although we are unable to accurately measure all of the terms in (3-1), our focus is on whether or not the dominant lateral balance is geostrophic at tidal time scales. Thus, we are most interested in the coriolis terms (second term on the left hand side), and the barotropic (first term right hand side) and baroclinic (second term right hand) pressure gradients. In order to estimate the coriolis term, we use the ADCP and ADP data from the channel and shoal site. In order to negate the influence of any phase difference between the two locations, the data was interpolated onto a matching vertical coordinate and the along-channel velocities were averaged.

The pressure sensor at the channel site was located at a depth of 5.48 m, while the pressure sensor deployed at the shoal location was located at a depth of 5.03 m. The near-bottom pressure difference was calculated by differencing the pressure measurements collected at the channel and shoal sites after removing the hydrostatic contribution between the 5.48 and 5.03 m depths at the channel site. The pressure difference between the two pressure sensors contains both a barotropic and baroclinic contribution. Because we are interested in both of these contributions, we attempted to remove the baroclinic contribution using the CTD data collected at the channel and shoal

locations. Unfortunately, due to the instrument deployment configuration, we do not have measurements of density in the upper 2.5 meters of the water column. To offset this problem, we simply assume that the lateral density gradient is constant in z over the top 2.5 meters of the water column. We then calculate the lateral density difference measured between the two sites and remove the baroclinic contribution to the pressure gradient. In examining the lateral dynamic balance we are interested in the tidal variations of the depth-integrated form of equation (3-1). The lateral pressure difference is very sensitive to even slight changes in the relative heights of the two pressure sensors relative to the local geopotential. Tripods often settle over the course of a deployment, potentially confounding efforts to estimate the residual barotropic pressure gradient. Because we are mainly interested in the tidal dynamics, the estimates of both the depth integrated barotropic and baroclinic pressure gradients were high-pass filtered to remove any of the sub-tidal variations from the data. In doing this, any unknown offset caused by the difference in height between the two tripods relative to the geopotential is removed, by assuming that the net lateral barotropic pressure gradient does not significantly impact the tidal dynamics. The sub-tidal contribution to the coriolis term is also removed in a similar manner.

3.3 RESULTS

3.3.1 Observations

The 2003-04 experiment took place during a period of elevated rainfall. Discharge from the York River tributaries for December 2003 was, on average, nearly 3 times the 60-year average (Fig. 3-2a). The experiment spanned approximately 30 days, covering the full spring-neap tidal cycle. The spring-neap cycle was apparent in the

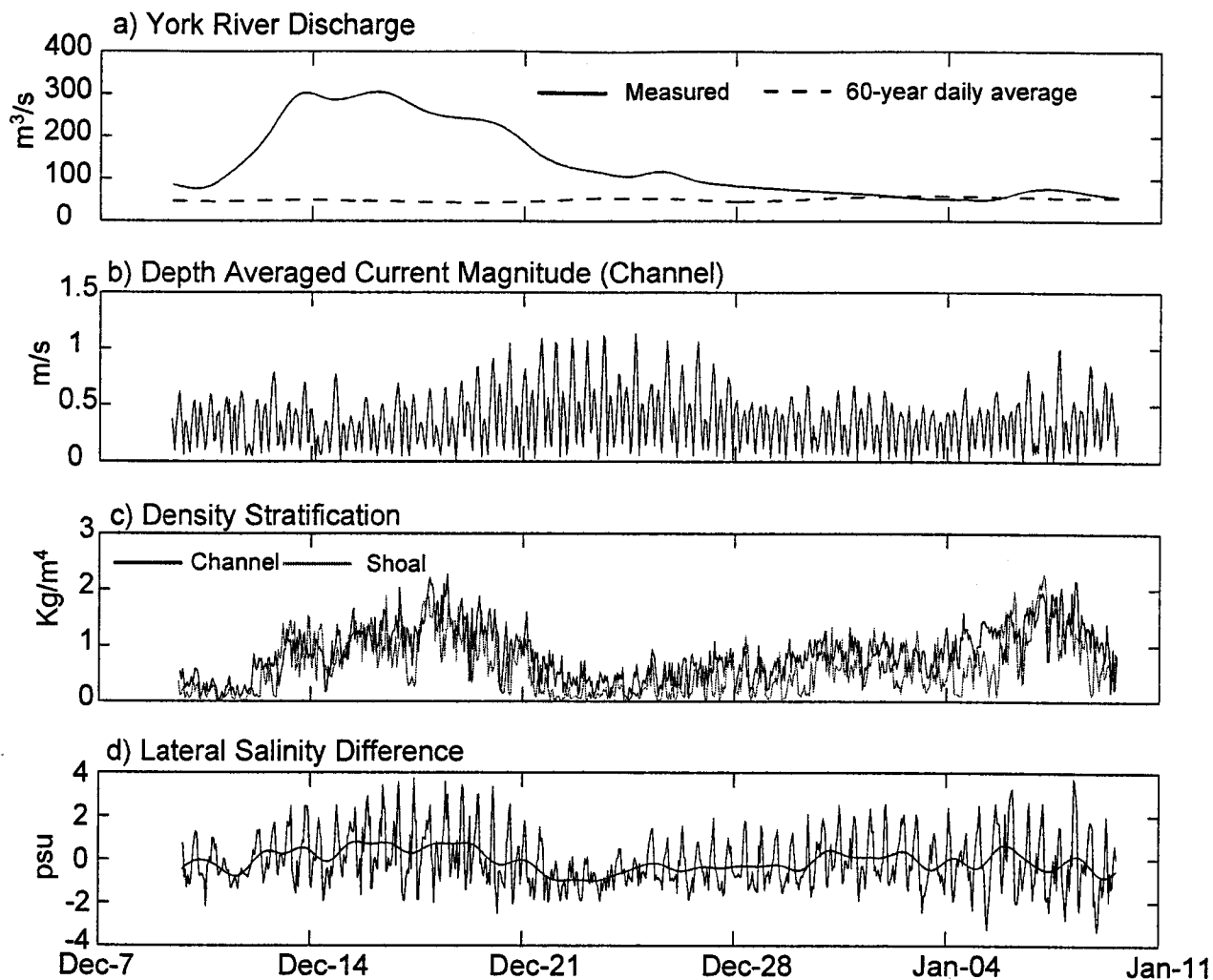


Figure 3-2. Time series data December 2003 — January 2004: a) combined daily river discharge from United States Geological Service's Mattaponi and Pamunkey gauging stations, with 60-year daily average; b) depth-averaged current magnitude measured by ADCP at the channel site; c) density stratification measured between the highest and lowest CTDs at the channel site (dark line) and the shoal site (light line); d) lateral salinity difference between channel and shoal location (positive indicates higher salinity in channel) with 35-hour lowpass filter.

depth averaged current magnitude measured at the channel site (Fig. 3-2b). With the elevated river discharge, there was persistent vertical density stratification throughout much of the experiment at both the channel and shoal sites, especially during neap tide (Fig. 3-2c). The vertical stratification exceeded 2 kg/m^4 on several occasions at both locations, and median values of stratification measured between the uppermost and lowermost sensors were 0.88 and 0.58 kg/m^4 at the channel and shoal sites, respectively. Through out the experiment there were significant lateral differences in salinity between the channel and shoal locations. Figure 3-2d shows the lateral difference in the depth averaged salinity between the channel and shoal locations. Positive values indicate saltier water at the channel site, as compared to the salinity measured at the shoal. In addition to significant tidal variability, there is a general tendency for the channel water to be fresher during the spring tide and slightly saltier during the neap. This can be seen in the lowpass filtered salinity data shown in figure 3-2d. This pattern can be explained by differential advection due to the residual axial currents at the two locations. The dynamics driving the pattern of lateral shear (du/dy) are discussed in detail in Scully and Friedrichs (submitted a) and will not be addressed in this paper.

Superimposed upon the sub-tidal variability in the salt field is significant tidal variability. There is a clear pattern where the channel location becomes saltier than the shoal during ebb, with the greatest difference occurring at the end of ebb. During the flood, this pattern is reversed and channel eventually becomes fresher than the shoal, again with the greatest difference occurring near slack water. This is opposite of the pattern expected in frictional estuaries caused by differential advection of the along-channel density gradient (Nunes and Simpson, 1985). While differential advection of the

axial density gradient is the mechanism most commonly invoked to explain lateral density gradients at the tidal time scales in shallow estuaries, in stratified systems the lateral circulation often tilts the isopycnals and can be the dominant mechanism driving the lateral density gradients (Lerczak and Geyer, 2004). Figure 3-3 shows the salinity field as measured by the CTD data at each site segregated by the stage of the tide.

Although we only have data at two locations, the data is contoured to try and visually represent the tilting of the isopycnals. The data in figure 3-3 represent “an average tidal cycle” of the salinity field beginning at the start of the ebb (Fig. 3-3a) and finishing at the end of flood (Fig. 3-3i). The average tidal cycle representation was calculated by dividing the entire time series of salinity data into sections of length equal to the M_2 tidal period and then averaging all values with the same relative tidal phase. From the data in figure 3-3, it appears that the slope of the isopycnals is oscillating back and forth at the tidal frequency.

To compare the relative importance of the vertical motions of the isohalines to differential advection of the longitudinal salinity gradient the tidal variability of the salt field is examined in more detail. Figures 3-4a and 3-4b show the average tidal cycle of the depth-averaged salinity collected by the CTDs at the channel and shoal locations, respectively. Prior to calculating the tidal phase average, any non-tidal signal was removed by subtracting the lowpass filtered time series. As a result, the tidal signal shown in figure 3-4 simply oscillates about a mean salinity of zero. For comparison, the expected change in salinity based only on longitudinal advection of the along-channel salinity gradient is shown. For this calculation the product of the depth averaged along-channel velocity and a constant along-channel salinity gradient ($-4e-4$ psu/m) is

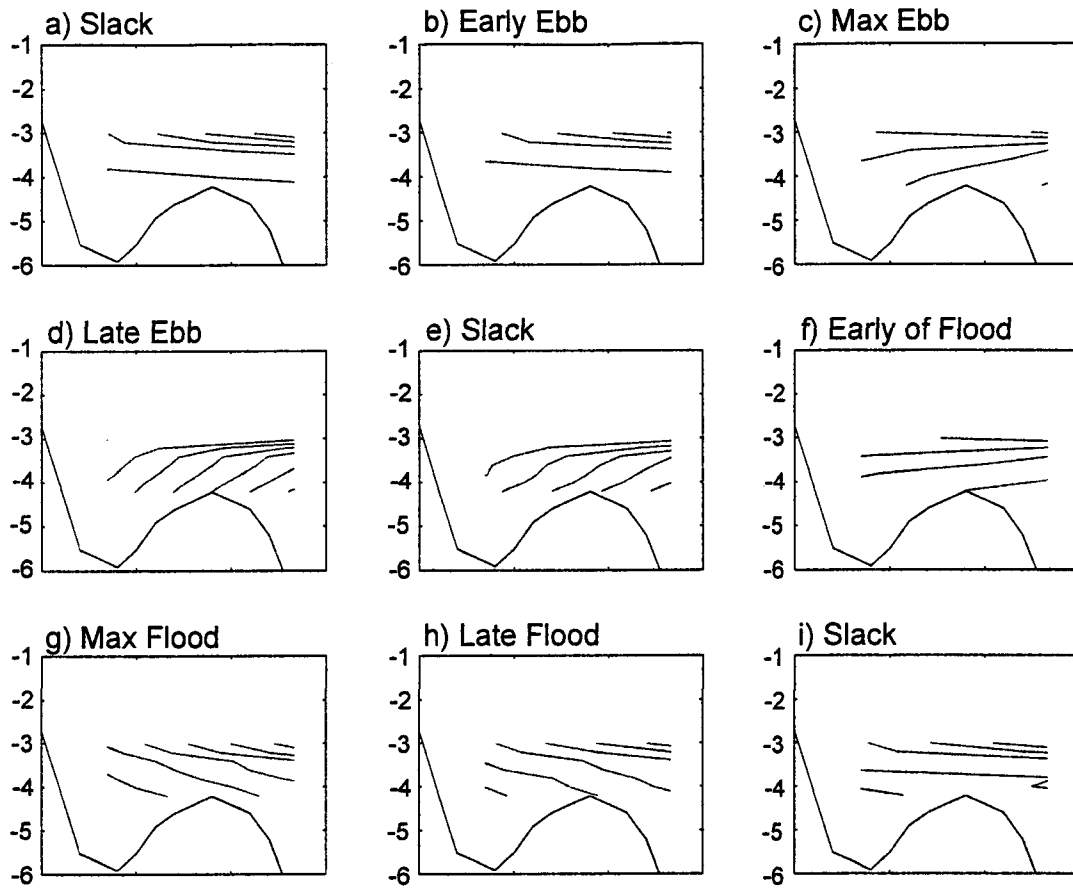


Figure 3-3. Average tidal cycle salinity contours from CTD data. Contour interval is 0.4 psu.

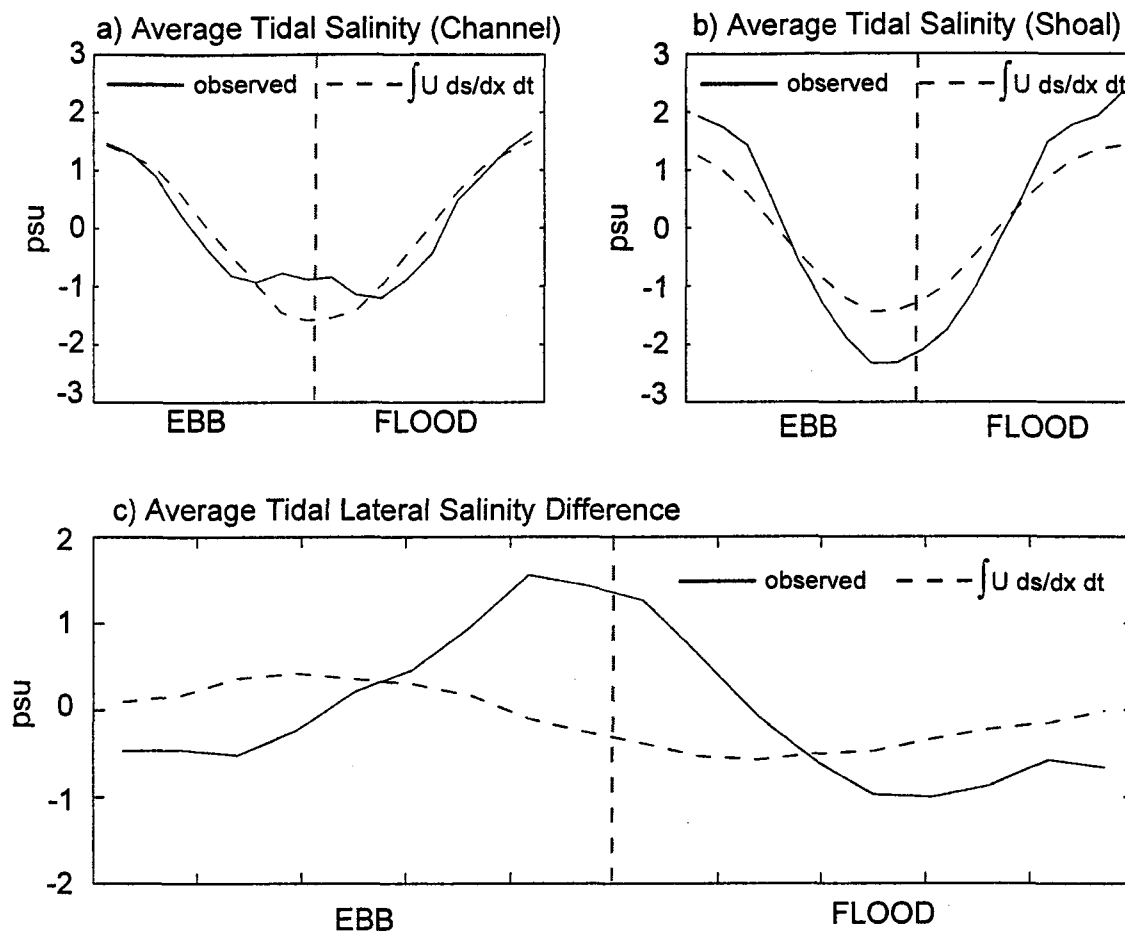


Figure 3-4. Comparison of the observed salinity with the salinity expected due to longitudinal advection. a) channel location; b) shoal location; c) lateral salinity difference (solid lines are the observed values and dashed lines are based on the expected longitudinal advection; positive values indicate the salinity at the channel is greater than the salinity at the shoal).

integrated in time and then averaged as a function of tidal phase, as discussed above. Consistent with the salinity data, the non-tidal signal was removed from the velocity time-series for both the channel and shoal sites. At the channel site during the early part of the ebb tide, the salinity is decreasing consistent with the along-channel advection. However, towards the end of ebb, the along-channel advection of fresher water is offset by the upwelling of saltier water from the deeper portion of the channel as the pycnocline seiches upwards at this location (Fig. 3-3). As the flood begins, the salinity at this location still remains relatively constant. Now, longitudinal advection during the flood appears to be offset by the freshening impact of the downward vertical motion of the pycnocline.

The change in salinity at the shoal also is consistent with the vertical motion of the pycnocline shown in figure 3-3. During both flood and ebb, the change in salinity at the shoal location is larger than if driven purely by longitudinal advection. During the flood, when the pycnocline is moving upward at this location, the salinity increases faster than due to longitudinal advection. The opposite is observed during ebb when the pycnocline is moving downward. The interaction of the lateral circulation and the stratification is the driving force controlling the lateral baroclinic pressure gradient. This is clearly illustrated in figure 3-4c, where the measured lateral salinity difference is compared to the expected lateral gradient solely due to longitudinal advection. Not only is the observed gradient significantly larger than that expected by differential advection, but also it is also 90 degrees out of phase. Thus, despite the fact that the York River has been used as an example of a system where the lateral dynamics are strongly impacted by differential advection (Huzzey and Brubaker, 1988), the results presented in figure 3-4

suggest that differential advection is not dynamically important during stratified conditions.

It appears from the data presented above that lateral circulation is driving the lateral baroclinic pressure response. Figures 3-5a and 3-5c show the lateral velocity profiles measured by the ADP deployed at the shoal and the ADCP deployed at the channel location, for both flood and ebb. Because we are interested in the tidal behavior, flood and ebb values are plotted separately (Figs. 3-5b and 3-5d) after removing the mean profile (dashed line in Figs. 3-5b and 3-5d). At the shoal location during the ebb, the near bottom currents are to the right (when looking up-estuary), while the surface currents are to the left, consistent with Ekman dynamics. This pattern of secondary circulation is leading to the upwelling of saltier water observed at the channel site during the ebb tide. The reverse pattern is seen during the flood when the near bottom lateral currents at the shoal are directed to the left surface currents are to the right. This pattern of lateral circulation causes the pycnocline to seiche back in the other direction, with downwelling at the channel location during flood. At the channel site, the pattern of lateral circulation appears to be inconsistent with those observed at the shoal site. There is a relatively strong mean circulation at this location, with a tidal signal that is opposite of that observed at the shoal location. It appears that the velocity data collected at the shoal are more representative of the overall circulation pattern for the region in between the sampling locations, and that the velocity data recorded at the channel site is more representative of dynamics of the deeper and adjacent region of the channel. The apparent inconsistency between the velocity data collected at the two locations will be discussed in detail in section 3-4.

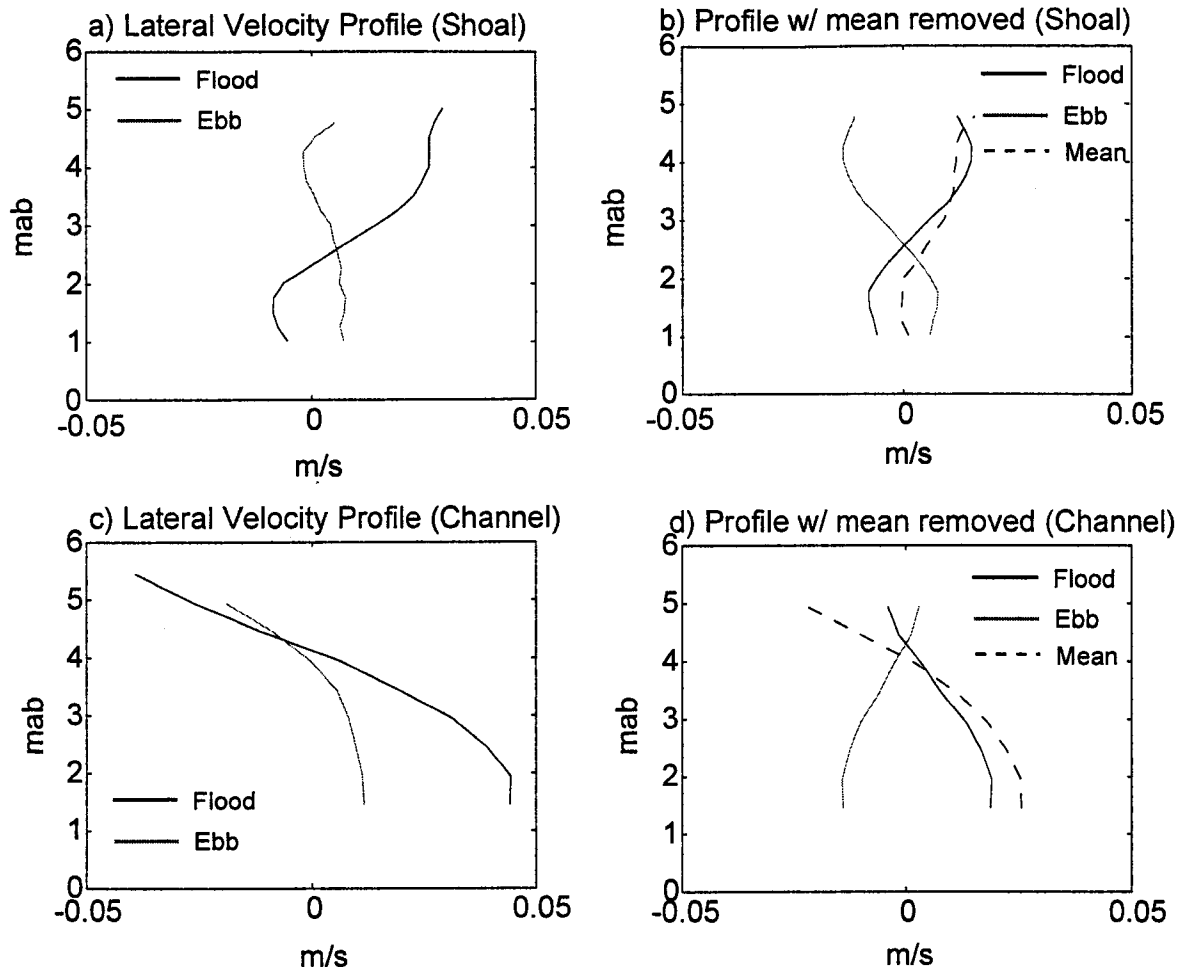


Figure 3-5. Average profiles of lateral velocity at the shoal (a and b) and channel (c and d), segregated by the phase of the tide (dark line flood, light line ebb). In a and c, the mean profile (dashed line) has been removed.

Lerczak and Geyer (2004) concluded that under stratified conditions, the interaction between lateral circulation and stratification acted to limit secondary flows. In their modeling study, the lateral circulation was significantly reduced during more stratified conditions. This behavior is clearly seen in this data set. Although the focus of this paper is on the tidal dynamics, looking at the sub-tidal patterns in lateral circulation is informative. The strength of the lateral circulation is quantified by simply differencing the lateral velocity from the top and bottom bins from the ADCP and ADP at the channel and shoal locations, respectively. The absolute value of this time-series was smoothed using a 50-hour lowpass filter and plotted in figure 3-6. At both the channel and shoal locations the strength of the lateral circulation is greater during the less stratified spring tidal conditions. In fact at both locations the strength of the lateral circulation is negatively correlated with the observed lowpass filtered density stratification ($r = -0.38$ and $r = -0.65$, at the channel and shoal, respectively).

The seiching behavior of the pycnocline presented in figure 3-3 suggests that the upper portion of the water column is largely frictionless and that the lateral balance is geostrophic. Consistent with a thermal wind balance, the lateral density gradient and du/dz are in balance, reversing with the change of the tide. To examine the importance of friction in the upper layer we can use the ADCP and ADP data in conjunction with the CTD data to estimate a gradient Richardson number (Ri_g), given as:

$$Ri_g = \frac{-\frac{g}{\rho} \frac{\partial \rho}{\partial z}}{\left(\frac{\partial u}{\partial z}\right)^2 + \left(\frac{\partial v}{\partial z}\right)^2} \quad (3-2)$$

At both the channel and shoal locations, the two uppermost CTDs were used to measure the density gradient. The velocity data from the ADCP and ADP were interpolated to the

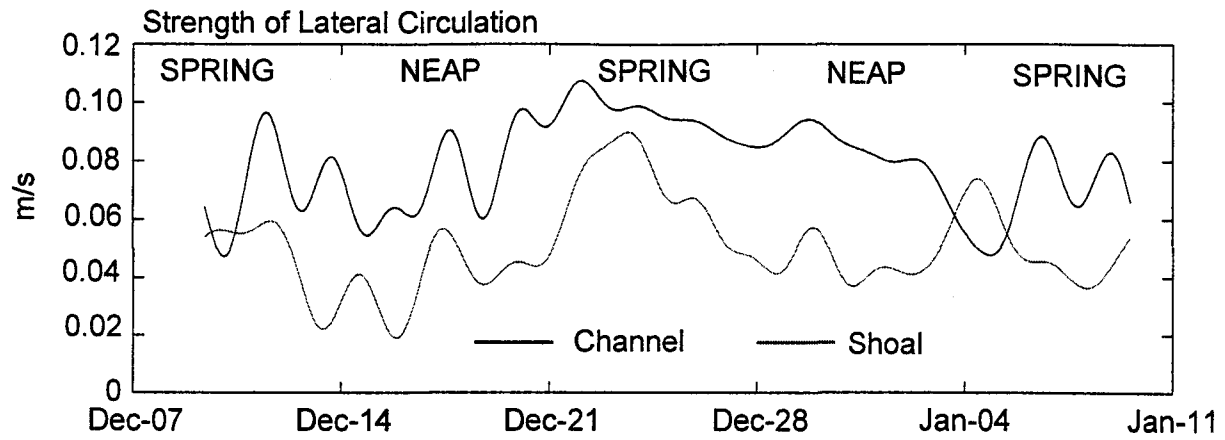


Figure 3-6. Strength of lateral circulation at channel (dark line) and shoal (light line) locations. The strength of the lateral circulation was calculated by taking the absolute value of the difference between the top and bottom bins of the ADCP/ADP. Values have been smoothed with a 50-hour lowpass filter.

heights of these CTDs to estimate the vertical velocity shear. Estimates of Ri_g are shown in figure 3-7 for the channel and shoal locations. Because we are taking the quotient of two gradient quantities, estimates of Ri_g are noisy. Despite the noise, it is clear that for both locations Ri_g is well above its critical value of 0.25 in the upper portion of the water column. Median values for the entire deployment are 1.47 and 3.66 for the channel and shoal locations, respectively, suggesting that the density stratification is suppressing mixing due to shear instabilities.

3.3.2 Lateral Momentum Balance

The evidence presented above suggests that the lateral balance is geostrophic at tidal time scales. However, we can use both the pressure sensor data and along-channel velocity data to more quantitatively evaluate the lateral dynamical balance, as discussed in section 3.2.3. Figure 3-8a shows the time series of the depth integrated coriolis term plotted against the combined pressure gradient terms. These terms are highly correlated, with a correlation coefficient of 0.75. The same data are shown as a scatter plot in figure 3-8b. Although there is some scatter in the data, the balance at the tidal time scale appears to be largely geostrophic. This balance can be examined more clearly by looking at the average tidal cycle values of the depth integrated coriolis, barotropic and baroclinic forcing (Fig 3-8c). From this view it is clear that the baroclinic and barotropic pressure gradients are largely out of phase. At the tidal time-scale the lateral pressure gradient largely balances the coriolis forcing. In addition to measuring the baroclinic and barotropic pressure gradients and coriolis forcing, we are able to estimate a number of the other terms equation (3-1). Using the lateral velocity data we can estimate both the acceleration term, as well as the bed stress based on quadratic drag. The magnitude of

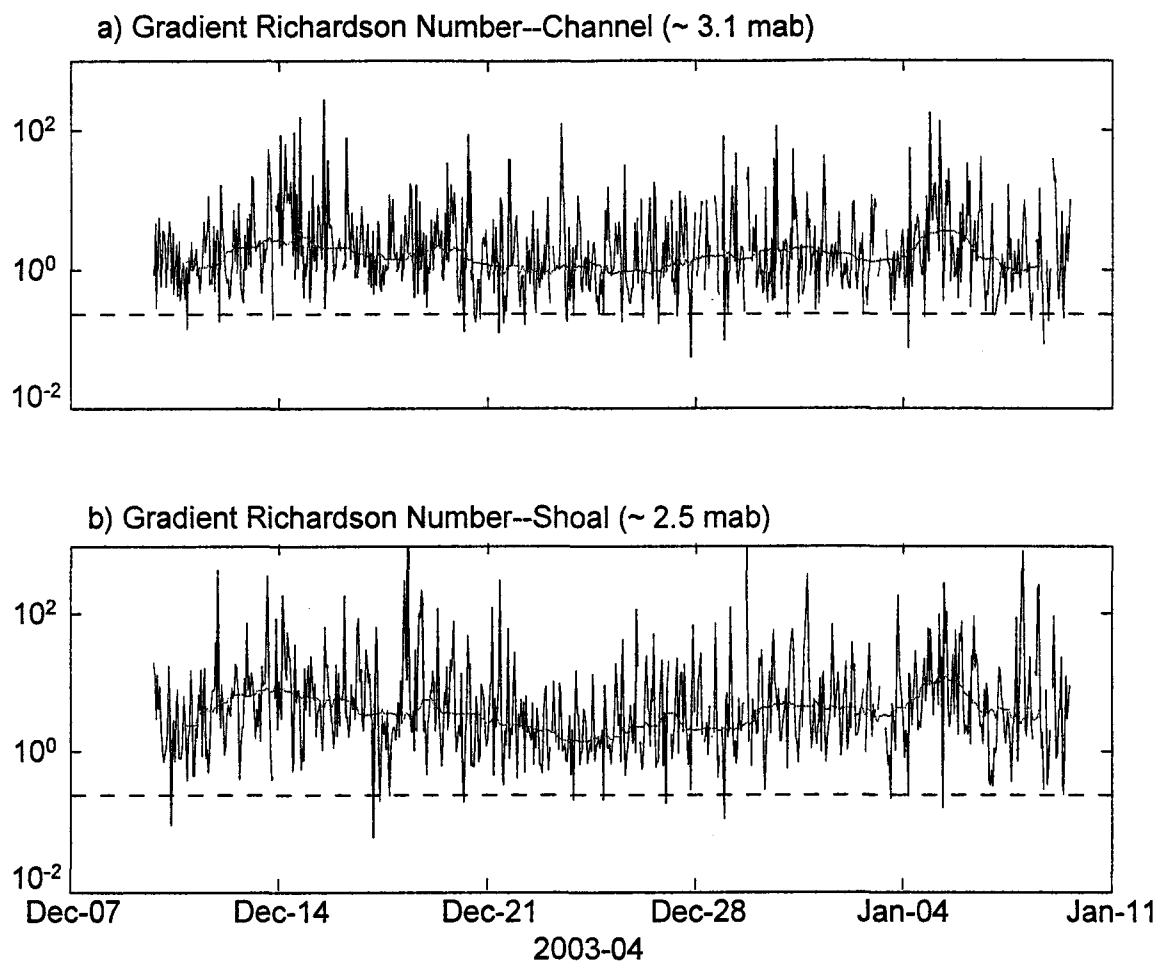


Figure 3-7. Gradient Richardson number at a) Channel location; b) Shoal location. Horizontal dashed line represents critical value (i.e. $Ri_g = 0.25$). Light solid line represents 50 hour running median.

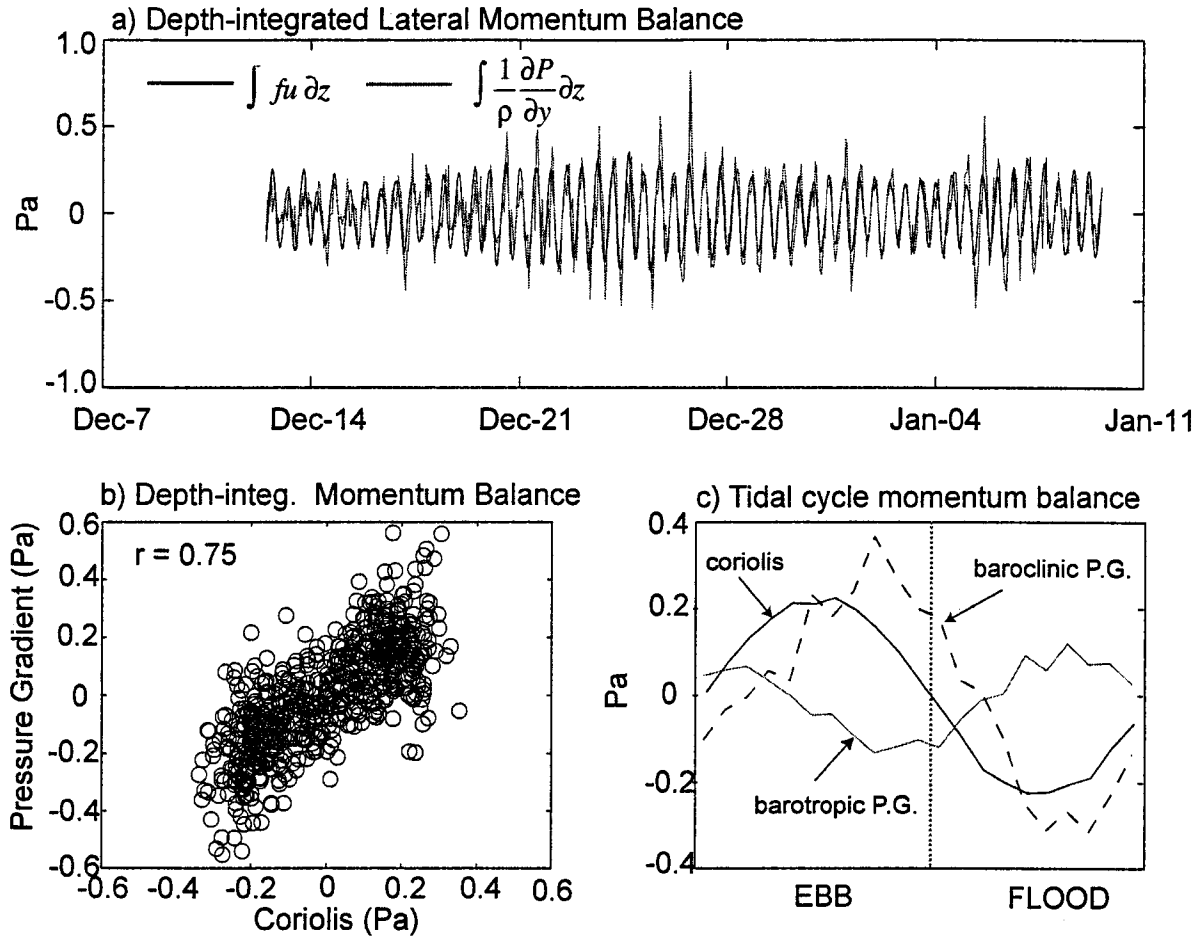


Figure 3-8. Estimates of the depth-integrated lateral momentum balance. a) time series of the coriolis forcing compared with lateral pressure gradient; b) scatter plot of depth-integrated coriolis and lateral pressure gradient terms; c) average tidal cycle showing contributions from coriolis (dark line), barotropic pressure gradient (light line), and baroclinic pressure gradient (dashed line).

both of these terms is consistently at least an order of magnitude smaller the terms comprising the geostrophic balance at the tidal time scale. Estimating the advective terms is more difficult given the relatively large distance between the two instrumented locations and the lack of along-channel resolution. These terms may be important particularly near abrupt changes in bathymetry as suggested by Valle-Levinson et al. (2000). However, our estimates suggest that they do not contribute at first order to the more integrated approach taken in this paper.

3.3.3 Simple Model for Lateral Tidal Dynamics

The data presented above suggest that the lateral dynamics in straight estuaries under stratified conditions are largely geostrophic. The presence of stratification and the absence of friction above the pycnocline enable several simplifying assumptions and allows us to construct a simple reduced-gravity two-layer model, as depicted in Figure 3-9. We define the upper and lower layer thicknesses to be h_1 and h_2 , respectively. The vertical coordinate (z) is positive upward with the interface between the two-layers defined as $z = \zeta$ and the water surface at $z = \eta$. If the pressure field is assumed to be hydrostatic, the linearized, layer-averaged, Boussinesq momentum and continuity equations can be written as:

$$\frac{du_1}{dt} = -g \frac{d\eta}{dx} \quad (3-3a)$$

$$f u_1 = g \frac{d\eta}{dy} \quad (3-3b)$$

$$\frac{du_2}{dt} = -g \frac{d\eta}{dx} - R u_2 \quad (3-3c)$$

$$f u_2 = g \frac{d\eta}{dy} + g' \frac{d\zeta}{dy} \quad (3-3d)$$

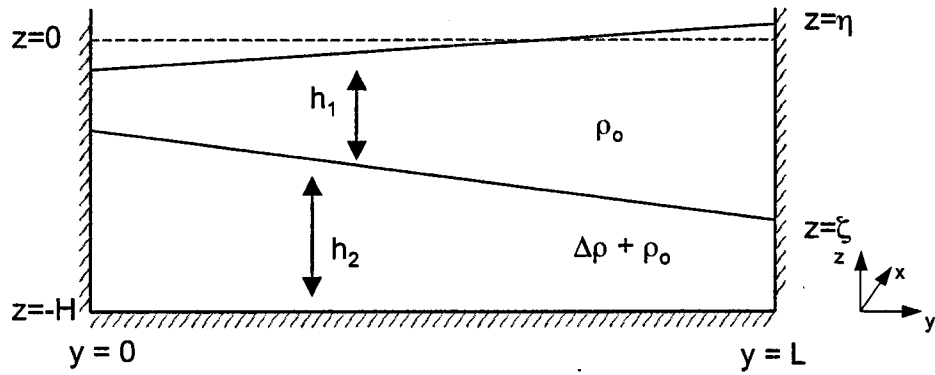


Figure 3-9. Schematic representation of the two-layer reduced gravity model.

$$-\frac{d\zeta}{dt} + h_1 \frac{dv_1}{dy} = 0 \quad (3-3e)$$

$$\frac{d\zeta}{dt} + h_2 \frac{dv_2}{dy} = 0 \quad (3-3f)$$

This approach is similar to the 3-layer model of Martin et al. (2005) applied to the outer Straight of Juan de Fuca. However, the Straight of Juan de Fuca is an order of magnitude deeper and wider than the system described above. Both scaling arguments, as well as estimates from the momentum integral allow us to make further simplifications. Given the Richardson number estimates presented above, we assume that the upper layer is frictionless. Based upon both the momentum estimates, as well as scaling arguments, we are neglecting both lateral acceleration and lateral friction in both the upper and lower layers. Lateral friction is easily included, but does not change the results presented below for a system as narrow as the York River. Friction does contribute at first order to the lower layer x-momentum equation (3-3c), and is parameterized using a Raleigh drag coefficient (R). In addition, we do not include the influence of rotation in the along-channel momentum equations (3-3a and 3-3c), because we assume it does not contribute at first order to the tidal dynamics. However, as with the lateral friction term, this term could be included and would not change the results presented below. All along-channel variations ($\partial/\partial x$) are ignored except in the prescribed barotropic pressure gradient. The layer-averaged continuity equations (3-3e and 3-3f) have been linearized by assuming that $\zeta \gg \eta$ and that h_1 and $h_2 \gg \zeta$. The reduced gravity (g') is defined as $g \Delta\rho/\rho_0$.

Because we are interested in the tidal dynamics, we assume that the quantities of interest vary periodically at the tidal frequency ($u, v, \eta, \zeta \sim e^{i\omega t}$, where ω is the M2 tidal frequency). This set of equations is easily solved by applying the boundary conditions of

no flow at either lateral barrier (v_1 and $v_2 = 0$ at $y = 0$ and $y = L$) and by prescribing the magnitude of the along-channel barotropic pressure gradient ($\partial\eta_o/\partial x$), which is assumed to be independent in y . Solution of these equations gives:

$$u_1 = \text{Re} \left\{ \frac{d\eta_o}{dx} \frac{gi}{\omega} e^{i\omega x} \right\} \quad (3-4a)$$

$$u_2 = \text{Re} \left\{ \frac{d\eta_o}{dx} \frac{g}{\omega} \frac{(i - R/\omega)}{(1 + R^2/\omega^2)} e^{i\omega x} \right\} \quad (3-4b)$$

$$v_1 = \text{Re} \left\{ \frac{1}{2} \frac{d\eta_o}{dx} \frac{Rfg}{h_1 g' \omega} \frac{(i - R/\omega)}{(1 + R^2/\omega^2)} yL \left(1 - \frac{y}{L}\right) e^{i\omega x} \right\} \quad (3-4c)$$

$$v_2 = \text{Re} \left\{ -\frac{1}{2} \frac{d\eta_o}{dx} \frac{Rfg}{h_2 g' \omega} \frac{(i - R/\omega)}{(1 + R^2/\omega^2)} yL \left(1 - \frac{y}{L}\right) e^{i\omega x} \right\} \quad (3-4d)$$

$$\eta = \text{Re} \left\{ \frac{d\eta_o}{dx} \frac{if}{\omega} L \left(\frac{y}{L} - \frac{1}{2}\right) e^{i\omega x} \right\} \quad (3-4e)$$

$$\zeta = \text{Re} \left\{ \frac{d\eta_o}{dx} \frac{iRfg}{\omega^2 g'} \frac{(1 - R/\omega)}{(1 + R^2/\omega^2)} L \left(\frac{y}{L} - \frac{1}{2}\right) e^{i\omega x} \right\} \quad (3-4f)$$

To examine the simplest case broadly representative of the York River estuary, the model was applied to 3 km wide channel of uniform depth (10 m). The initial layer thicknesses are equal ($h_1 = h_2 = 5$ m), and the magnitude of the along-channel barotropic pressure gradient was selected to result in an along-channel current magnitude in the upper layer of approximately 0.75 cm/s ($\partial\eta_o/\partial x = i\omega u_1/g$). A value for the reduced gravity (g') of 0.04 m/s² was used, consistent with the degree of stratification observed during this experiment.

This rather simple model captures a number of the key features of the lateral dynamics described above. As shown in Figures 3-10a and b, it predicts the upwelling of

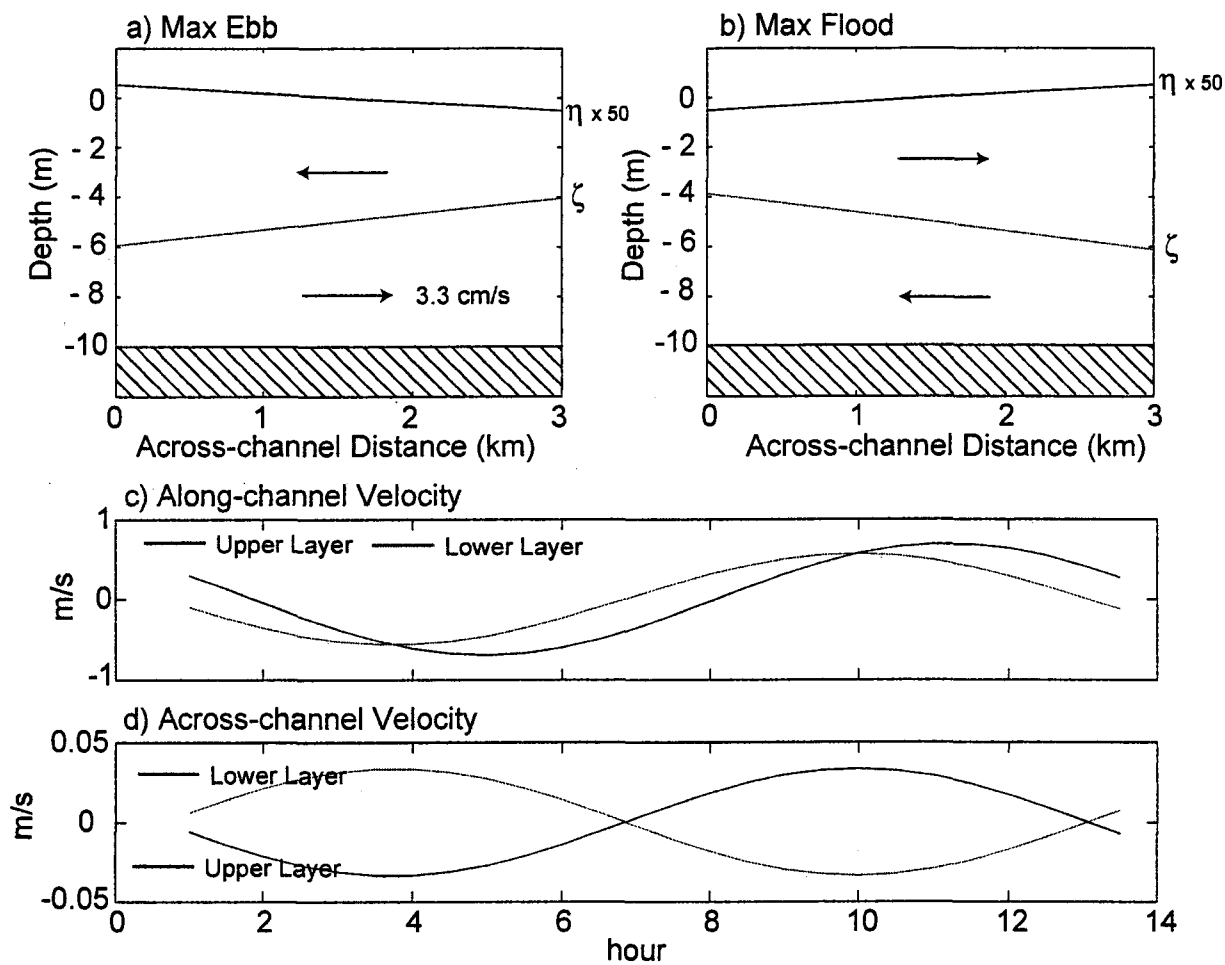


Figure 3-10. Predicted surface elevation (multiplied by a factor of 50) and pycnocline height from the two-layered model for a) max ebb; b) max flood; and the predicted c) longitudinal and d) lateral velocities for the channel mid-point in the upper (dark line) and lower (light line) layer.

the pycnocline along the right side (looking up-estuary) of the channel during ebb (negative values in Fig. 3-10c) and downwelling at this location during the flood, with a vertical excursion of approximately 2 meters. This behavior of the pycnocline is driven by the Ekman transport in the lower layer. The frictionless surface layer is in geostrophic balance with the lateral barotropic pressure gradient. As a result, the barotropic and baroclinic pressure gradients are largely out of phase consistent with data shown in figure 3-8c. This results in a pattern of circulation where the lower layer flow is in the opposite direction of the surface layer flow (Fig. 3-10d). Consistent with the pattern seen in figure 3-5b, the near-bed velocity is to the right (looking up-estuary) during ebb and to the left during flood. Figure 3-11 shows the integrated momentum balance for the lower layer from the model, which is highly consistent in both magnitude and phase with the measured balanced presented in figure 3-8c. The inverse dependence of the lateral circulation on stratification demonstrated in figure 6, can be clearly seen in equations 3-4c and d, where g' appears in the denominator. The lateral flow also is dependent upon the magnitude of the along-channel barotropic pressure gradient ($\partial\eta_0/\partial x$), and the linear friction coefficient (R), both of which would increase during spring tidal conditions favoring greater lateral circulation. However, the strength of the lateral circulation will clearly depend most on the level of stratification, which will have the greatest level of fortnightly variability.

The lateral circulation in the model is driven by along-channel friction through Ekman transport. Thus, while the lateral circulation is frictionally-driven, friction does not appear in the y-momentum equation. Even when lateral friction is included the results shown in figure 3-10 remain unchanged. Without friction, the balance would be

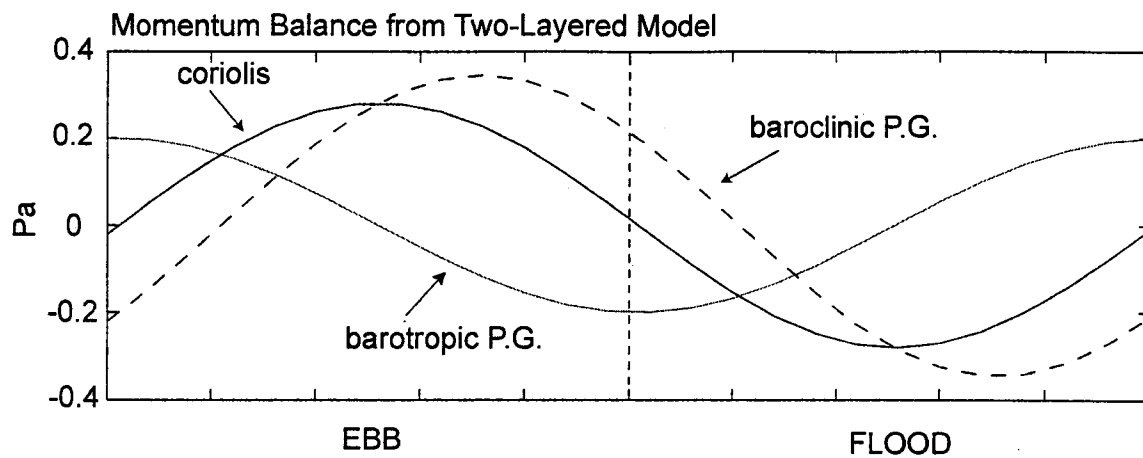


Figure 3-11. Depth-integrated lateral momentum balance for the lower layer from the reduced-gravity model. Consistent with the observations, the balance is geostrophic with the coriolis forcing (dark line), balanced by the combined barotropic (light line) and baroclinic (dashed line) pressure gradients.

purely geostrophic and would not drive any lateral circulation. This is consistent with the observations presented in section 3.3.2, which demonstrate that the lateral balance is largely geostrophic, despite relatively strong lateral circulation. Excluding the lateral friction term can only be justified in relatively narrow systems such as the York. Scaling the lateral friction (RV_2) to the rotational forcing ($f\Delta U$) suggests this assumption is only appropriate when the channel width (L) $\ll 8(h_2g')^{1/2}/R$.

3.4 DISCUSSION

The lateral velocity profiles for the channel location presented in figures 3-5c and 5d do not appear to be consistent with the Ekman driven lateral flows observed at the shoal location or described by the analytical model presented in section 3.3.3. There is a strong mean circulation and the flood and ebb profiles are opposite from the expected Ekman dynamics. There are several possible explanations for this behavior.

3.4.1 Channel Curvature

The first explanation is the presence of slight curvature of the channel down-estuary from the deployment location. Although the river itself is very straight throughout this region, the channel does undergo roughly a 15-degree bend towards the south down-estuary from Clay Bank. Given the angular nature of this bend, estimating a radius of curvature (r) is somewhat difficult. However, an estimate of r of approximately 10 to 15 kilometers appears reasonable. Scaling arguments suggest that channel curvature will be dynamically important when the ratio $(fr)/u$ is order one. Given that typical along-channel velocities approach 1 m/s, it is possible that the flow pattern observed at the channel location is influenced by curvature effects. This would induce the observed mean pattern of circulation demonstrated in figure 3-5d. Curvature effects

are unlikely to be important during the ebb because the channel is straight upstream from this location and estimates of the Froude number indicate that the flow is, on average, supercritical. If curvature effects are only impacting the lateral velocity profiles at this location during the flood tide, removing the mean circulation profile may bias the ebb data in figure 3-5d making it appear inconsistent with the expected Ekman dynamics. However, without removing the mean circulation, the ebb profiles are consistent with the dynamics discussed above as seen in figure 3-5c. The lack of consistency during the flood could be the results of the tidally asymmetric influence of channel curvature.

3.4.2 Bathymetry

The other possible explanation is related to the positioning of the instrumentation at the channel location. In order to avoid interfering with shipping traffic, the instrumentation at this site was deployed along the southwest flank of the channel. The ADCP is capturing the upper 6 m of the water column, while the deepest part of the adjacent channel is approximately 10 m deep. Given the strong stratification observed during the experiment, it is likely that boundary layer is confined to a limited region near the bed. If the velocity profiles collected by the ADCP are more representative of the upper portion of the deeper channel than the adjacent shoal, the Ekman-driven boundary layer flow may not be observed. The model presented above assumes a channel of constant depth. However, the lateral bathymetry of the York River clearly varies in the across-channel direction. While the bottom boundary layer may effectively represent the lower half of the water column over the broad shoal region in between the two instrument locations, it may occupy a significantly smaller portion of the water column at the deeper channel location.

Lerczak and Geyer (2004) derive an analytical representation for tidally-varying Ekman-forced lateral flow in a homogenous fluid. They demonstrate that for small values of eddy viscosity ($A_z \sim 3.3e-4 \text{ m}^2/\text{s}$), the bottom boundary layer is very thin and the lateral flow has a three-layer structure. Given their results, it is possible our instruments at the channel did not capture the thin near-bed boundary layer, but only the upper two layers of the lateral circulation. The lateral circulation predicted by their solution is plotted in figure 3-12 using values representative of both the channel and shoal regions of the York River under stratified conditions. At the shoal location we use a depth of 6 m and an eddy viscosity of $1e-3 \text{ m}^2/\text{s}$ and for the channel, a depth of 10 m and an eddy viscosity of $5e-4 \text{ m}^2/\text{s}$. These values of eddy viscosity are slightly smaller than those estimated by Scully and Friedrichs (submitted a), but are consistent with the lateral asymmetry they demonstrated with larger values over the shoal region. The mean lateral flow predicted for ebb and flood are plotted in figures 3-12a and 3-12b, respectively. These profiles are largely consistent with the tidal patterns presented in figures 3-5b and 3-5d, with convergent flows near the bed during ebb and divergent flows during flood. This tidal pattern of near-bed convergence and divergence may contribute to the vertical motion of the isohalines near the channel location. During ebb, the convergent near-bed flow would create upward vertical velocities, which would contribute to the upward advection of isohalines, with the reverse pattern observed during flood.

3.4.3 Sub-tidal Forcing

The discussion above focuses only on the tidal behavior superimposed on the mean lateral circulation. Although we are unable to directly estimate the sub-tidal balance because of the uncertainty in the sub-tidal lateral barotropic pressure gradient, we

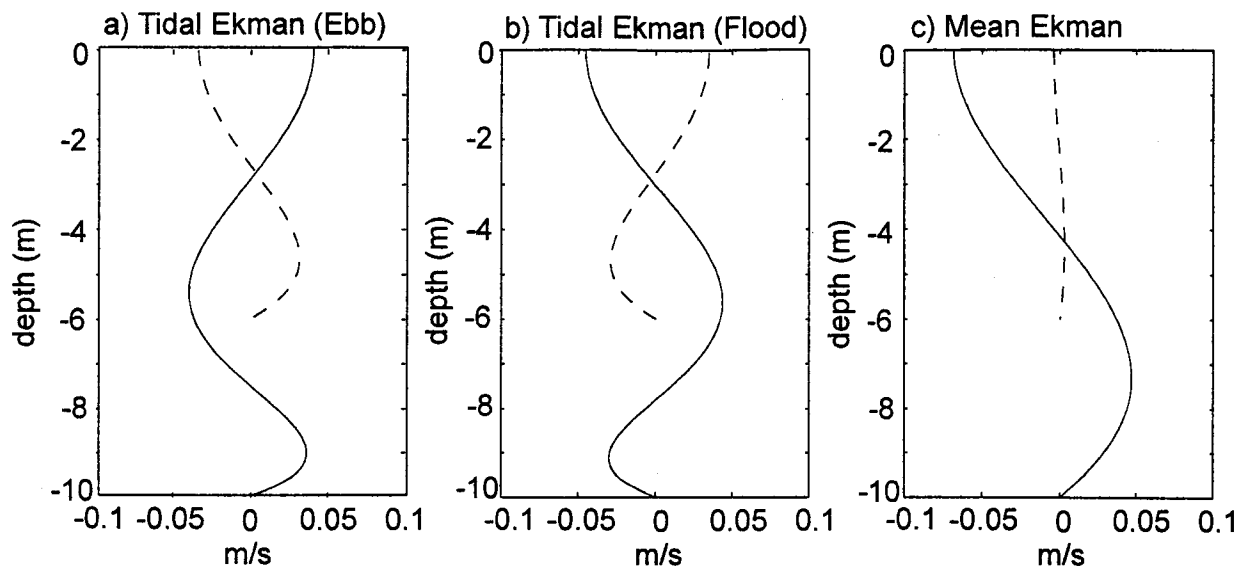


Figure 3-12. Analytic solution for tidally varying Ekman-forced lateral flow a) ebb and b) flood for a depth of 10 m and $A_z = 5 \text{ cm}^2/\text{s}$ (solid line) and and 6 m and $A_z = 10 \text{ cm}^2/\text{s}$ (dashed line); and c) Steady Ekman solution for a depth of 10 m and $A_z = 5 \text{ cm}^2/\text{s}$ (solid line) and and 6 m and $A_z = 10 \text{ cm}^2/\text{s}$ (dashed line) with $dp/dx = -3e-4 \text{ kg/m}^4$ and $dp/dy = -4e-5 \text{ kg/m}^4$.

can use our data to qualitatively examine this balance. At the channel location, there is a strong mean circulation and the lateral vertical velocity shear (dv/dz) does not change direction with the tide, suggesting that the tidal Ekman forcing is not sufficient to overcome the sub-tidal forcing. Previous authors have suggested a sub-tidal lateral balance between the combined pressure gradients and the internal stress, which results in a mean lateral circulation similar to the classic view of along-channel estuarine circulation (e.g. Nunes and Simpson, 1985). During this experiment relatively strong lateral sub-tidal density gradients were observed (Fig. 3-2d). Not only is the lateral density gradient often stronger than the axial density gradient, but it also changes sign during the fortnightly cycle. However, the mean values of dv/dz observed at the channel locations, do not change sign consistent with a frictional balance. This combined with the large estimated values of Ri_g suggests that friction does not contribute to the sub-tidal balance at the channel at first order.

Valle-Levinson et al. (2003) present an analytic model for sub-tidal estuarine flows that includes the barotropic and baroclinic pressure gradients, friction and the earth's rotation. Although they developed the model to examine the impact of transverse estuarine bathymetry, the solution is equally applicable to a 1-dimensional representation. This solution is presented in figure 3-12c, using the same parameters applied to tidally varying Ekman solution of Lerczak and Geyer (2004). In addition, application requires the specification of both the along-channel and across-channel density gradients. Both of these gradients can be estimated from our data and the mean values for the entire experiment were used. At the channel location, the predicted mean circulation is consistent with the observations. In addition, the predicted mean circulation is of the

same order as the predicted tidal circulation at the channel location. In contrast, at the shoal the predicted tidal circulation is significantly larger than the mean. It should be noted that the tidal Ekman solution of Lerczak and Geyer (2004) is for a homogenous fluid and there is no feedback between the lateral circulation and the stratification.

Without this interaction, the predicted tidal circulation represents the maximum Ekman-driven flow, which would be reduced by its interaction with stratification. Although the estimated lateral density difference varies substantially, even reversing sign during the experiment, the results in figure 3-12c are relatively insensitive to this for low values of eddy viscosity. In fact, as eddy viscosity decreases, dv/dz approaches the thermal wind balance and is completely independent of the lateral pressure gradient. This provides an explanation for why the residual lateral circulation at the channel maintains negative shear during neap conditions when the observed lateral density forcing would induce a positively-sheared residual profile.

At the channel location, the tidally-averaged values of dv/dz become increasingly negative higher in the water column, approaching the value dictated by $d\rho/dx$ through thermal wind near the water surface. The presence of strong stratification appears to limit the impact of friction to the near-bed region, and higher in the water column the sub-tidal balance is approaching thermal wind. The shear at the shoal location is not consistent with thermal wind, suggesting that friction may be important to the sub-tidal balance. For dv/dz to be explained via thermal wind, the rotational forcing (fv) must be of the same order or larger than the stress divergence in the sub-tidal along-channel momentum balance. In chapter two, we did not explicitly address the vertical structure of the sub-tidal along-channel momentum balance. However, we can use this data to

examine the balance. Figure 3-13, shows the profiles of the dominant terms in the along-channel momentum balance for both the channel and shoal locations. At the shoal location, the mean along-channel pressure forcing is predominantly balanced by stress divergence. However, at the channel location, the stress divergence and coriolis forcing have approximately the same magnitude. In fact, in the upper portion of the water column, the coriolis forcing is greater than stress divergence and the sub-tidal balance is approaching geostrophy. The dominance of the stress divergence term at the shoal suggests that the mean shear will be dictated by the lateral pressure forcing, which we cannot accurately resolve in our data set.

Although we are unable to directly measure the dominant terms in the sub-tidal lateral momentum balance, the evidence suggests that friction is not important at the channel location. The mean circulation, which is close to the thermal wind balance, is stronger than the Ekman forced tidal flow. The super-position of the mean and the tidal forcing, as depicted in figures 3-12b and 3-12c, leads to the tidal asymmetry in the lateral flow shown in figure 3-5c, with stronger lateral circulation during flood. At the channel location, the mean dv/dz is not consistent with thermal wind and the tidal forcing is significantly larger than the mean. Despite the fact, that the lateral balance appears to be largely geostrophic at tidal time-scales, friction may be important to the sub-tidal balance at the shoal location. This is supported by estimates of the along-channel momentum balance, but cannot be quantitatively addressed with our data.

3.5 CONCLUSIONS

The data and modeling results presented in this paper demonstrate that the lateral tidal momentum balance is largely geostrophic. Despite the fact that friction does not

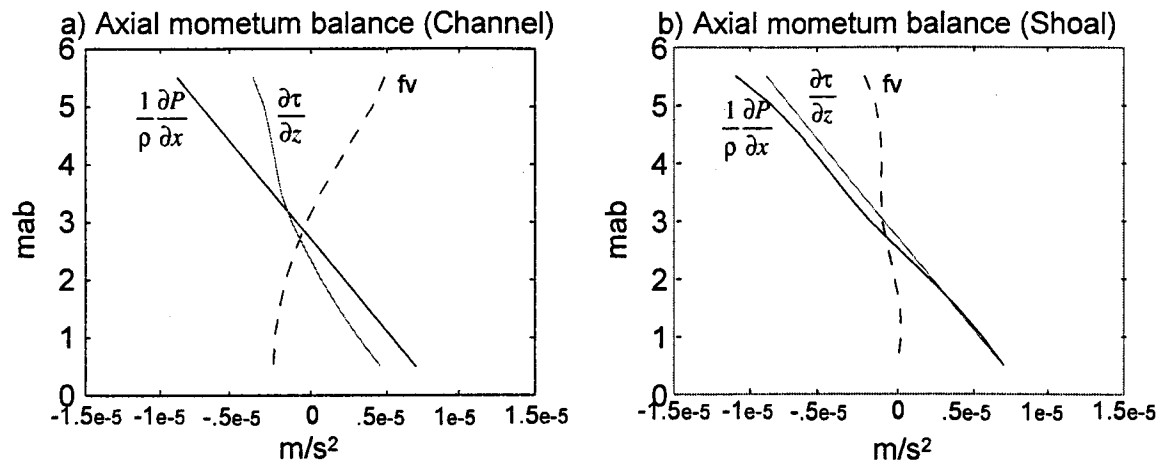


Figure 3-13. Sub-tidal axial momentum balance for the a) Channel and b) Shoal locations. Shown are the axial pressure gradient (dark line), coriolis forcing (dashed line) and stress divergence (light line) terms.

appear to contribute at first order to the lateral balance, frictional retardation of the along-channel flow is the driving force of the lateral circulation. The Ekman response to the along-channel flow drives a lateral circulation that causes the pycnocline to slope downward to the right of the along-channel flow. In the inviscid surface layer, the lateral barotropic pressure gradient responds geostrophically to the along-channel flow, causing the water surface and the pycnocline to move in opposition during the tidal cycle. This interaction of the lateral circulation and the stratification is the driving force controlling the lateral baroclinic pressure gradient. While differential advection of the along-channel density gradient may be important in well-mixed frictional systems, our results suggest that it is not driving the behavior of the lateral baroclinic forcing under stratified conditions. This feedback between the lateral circulation and the baroclinic pressure gradient reduces lateral circulation during stratified conditions and enhances lateral flows when the water column becomes more mixed. While the results detailing the sub-tidal lateral balance are less conclusive, there is evidence that the shallower channel areas are frictionally balanced, while the more stratified areas near the channel are approaching geostrophy at the sub-tidal time scale. More detailed studies that capture the interaction between the cross channel bathymetry, spatially and temporally stratification and turbulent mixing are necessary to better understand the dynamics of lateral flows and their importance to estuarine dynamics.

CHAPTER 4
SEDIMENT PUMPING BY TIDAL ASYMMETRY IN A
PARTIALLY-MIXED ESTUARY

4.0 INTRODUCTION

Classically, estuarine sediment transport is thought to be driven by the seaward-directed flux of the mean river discharge and landward-directed flux that results from the baroclinic residual circulation (e.g. Schubel, 1968). It is the convergence of these two processes that is most often invoked when explaining the region of elevated turbidity known as the Estuarine Turbidity Maximum (ETM). While the ETM often is located at the upstream limit of salt intrusion, secondary ETMs are found in the lower reaches of many estuaries (Lin & Kuo, 2001). Although it is likely that this simple convergent process plays a role in maintaining estuarine turbidity in many systems, a number of other processes exert important controls on estuarine sediment transport. The along-channel density gradient that drives the residual baroclinic circulation also creates vertical density stratification, which significantly impacts the turbulent mixing responsible maintaining sediment in suspension (Scully and Friedrichs, 2003). Geyer (1993) showed that the suppression of turbulence by stratification plays an important role in trapping sediment in the ETM.

In many partially mixed estuaries, vertically sheared tidal currents interact with the along-estuary salinity gradient, leading to predictable semi-diurnal variations in thermohaline stratification (Simpson et al., 1990). This process, known as tidal straining, promotes vertical mixing during the flood tide and suppresses mixing during the ebb (Stacey et al., 1999; Geyer et al., 2000; Rippeth et al., 2001). Tidal asymmetries in mixing caused by semi-diurnal variations in stratification have been shown to contribute

to the landward flux of sediment and contribute to particle trapping within estuaries (Jay and Musiak, 1994). Scully and Friedrichs (2003) demonstrated that this mechanism lead to a net up-estuary sediment flux even during periods when the residual circulation was directed in the opposite direction. Their results suggested that the asymmetries in stratification did not impact the bed stress, but altered the eddy diffusivity, leading to greater sediment resuspension during the flood tide.

The fall velocity of suspended sediment also exerts an important control on its vertical distribution. In estuarine systems characterized by fine cohesive sediments, particles in suspension often exist in an aggregated state (Postma, 1967). These larger “flocs” typically have higher settling velocities than their component grains. Because this process increases the settling velocity, leading to greater suspension lower in the water column, it increases the trapping effect of estuarine circulation and augments the formation of the ETM (Kranck, 1981). Aggregates form when individual particles collide due to Brownian motion, turbulent mixing, or differential settling. Turbulent mixing is also thought to play a role in the break-up of flocs when the length scale of the smallest turbulent eddies and the floc diameter are roughly of the same order (van Leussen, 1988). In the Hudson estuary, Traykovski et al. (2004) documented that the floc diameter was inhibited during the energetic portions of the tidal cycle, followed by relatively rapid flocculation when energy decreased. While a number of authors have documented the important relationship between turbulence and settling velocity, its role in estuarine sediment transport has not been fully addressed. It is possible that tidal asymmetries in mixing that are often observed in estuaries could result in asymmetries in resuspension that are the result of tidal changes in fall velocity.

This chapter is intended to examine the processes driving sediment transport in the York River estuary. It will highlight the importance that tidal asymmetries in turbulent mixing have on sediment resuspension by impacting both the eddy diffusivity as well as aggregation dynamics. In addition to these hydrodynamic effects, the erodibility of sediment in the bed also will be examined. The observational and analytical methods are described in Section 4.2 and the results are presented in Section 4.3. The results are discussed in Section 4.4 and conclusions are presented in Section 4.5.

4.2 METHODS

4.2.1 Hydrographic Measurements

During the winter of 2003-04, instrumentation was maintained at two laterally adjacent locations in the estuarine cross-section of the York River near Clay Bank, located roughly 13 kilometers up-estuary from Gloucester Point (Fig. 4-1). At this location in the York River, the main channel of the estuary is located on the northeastern side of the river with a maximum depth of approximately 10 meters. A broad shoal extends to the southwest of the main navigational channel with a maximum depth of approximately 6.5 meters. Instruments were deployed along the southwestern side of the main channel at a water depth of approximately 7 meters (“channel” site) to avoid interfering with navigation, and at the deepest location within the southwestern shoals at a water depth of roughly 6 meters (“shoal” site).

During the experiment, detailed velocity measurements were collected by 4 Sontek acoustic Doppler velocimeters (ADV), an RDI 1200 kHz acoustic Doppler current profiler (ADCP), and a Sontek 1500 kHz acoustic Doppler profiler (ADP). The 4 ADVs were mounted on a benthic boundary layer tripod deployed at the channel site to

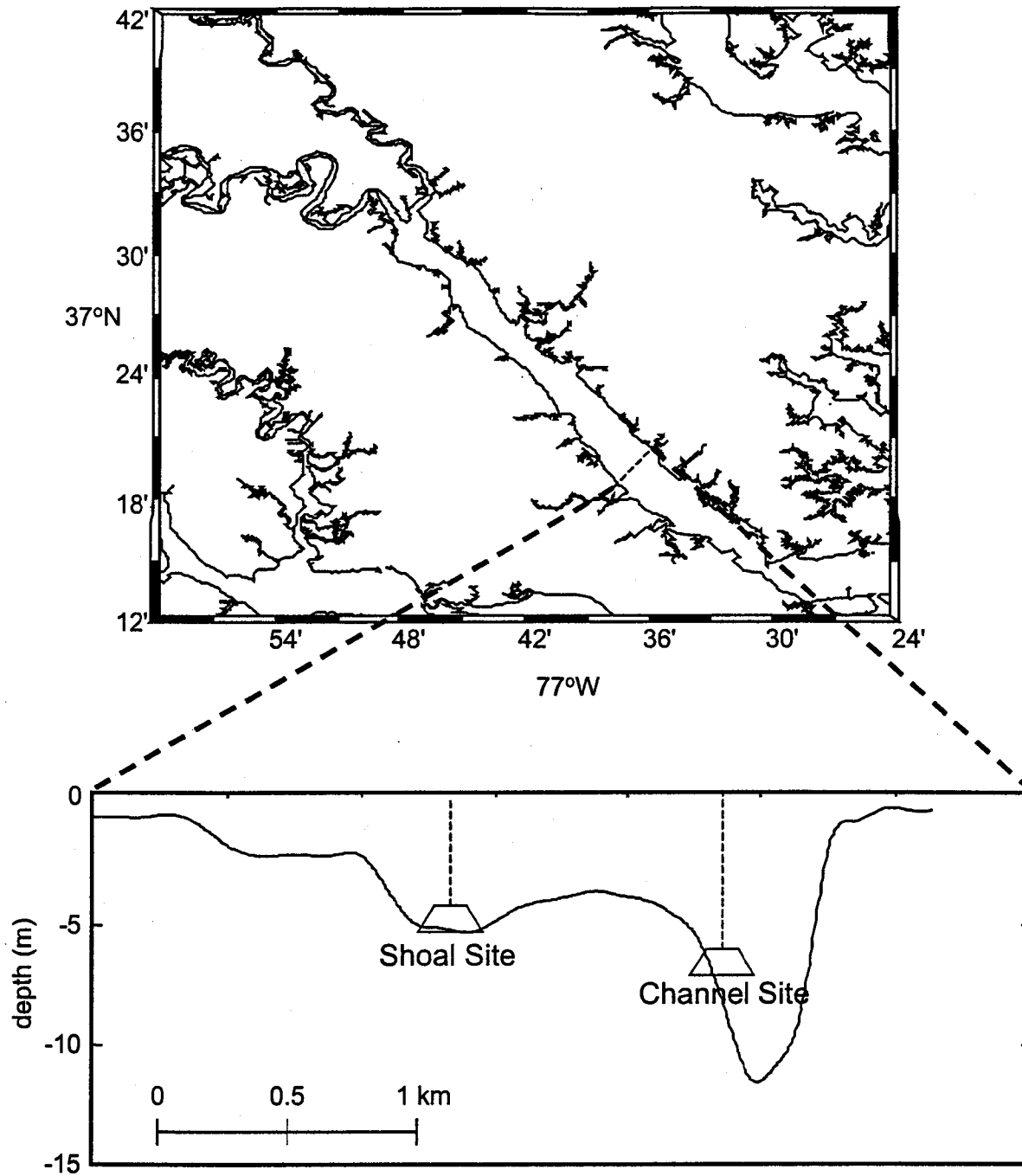


Figure 4-1. Map of study area, York River Estuary, Virginia with estuarine cross-section at the “channel” and “shoal” deployment locations.

provide high-resolution velocity measurements at discrete elevations over the lowest 1.2 meters of the water column. The ADVs were mounted 0.10, 0.43, 0.76, and 1.1 meters above the bed (mab), on an arm of the tripod that was rotated perpendicular to the dominant orientation of the York River channel. Unfortunately, the ADVs at 0.43 and 0.76 mab did not function properly and will not be discussed. The ADVs collected three-dimensional velocity measurements in 5 minute bursts once an hour at a sampling frequency of 5 Hz. The ADVs were equipped with an acoustic altimetry feature that reported the distance from the sensor to the bed at the end of each burst. The 1200 kHz ADCP was deployed immediately adjacent to the tripod at the channel site and collected vertical profiles of current velocity in 0.50 m bins. The ADCP sampled at roughly 1 Hz and collected one 10-minute burst every hour. The 1500 kHz ADP was deployed at the shoal site and sampled at a rate of 1 Hz averaged over one minute bursts to provide vertical profiles of current velocity in 0.25 m bins.

Three YSI 6000 conductivity, temperature and depth sensors (CTDs) outfitted with optical transmissometers were mounted on the tripod at the channel site at 0.10, 0.41, and 1.5 mab and collected pressure, salinity, temperature, and light transmission every 30 minutes. A mooring that consisted of a YSI 6000 CTD and an InterOcean S4 current meter, outfitted with a CTD was located immediately adjacent to the tripod at the channel site. The CTD and S4 on the mooring were located 2.8 and 3.4 mab, respectively. At the shoal site, two YSI 6600 CTDs located 0.10 and 1.5 mab and an InterOcean S4 sensor with a CTD located 3.5 mab were deployed immediately adjacent to the ADP. As with the YSI 6000, each of the YSI 6600 CTDs was outfitted with an optical transmissometer.

4.2.2 Suspended Sediment Measurements

All of the CTDs deployed at both the channel and shoals sites were outfitted with optical transmissometers to measure the attenuation of light due to the presence of suspended sediments. Prior to deployment, a two point linear calibration was performed for each transmissometer using de-ionized water and a fixed laboratory standard of with a known value of nephelometric turbidity units (NTUs). While this pre-calibration ensures that the instruments respond consistently to known values of laboratory standards, in order to convert NTUs actual concentration values, additional field calibration was necessary. Upon retrieval of the instruments, bottom sediment samples were collected immediately adjacent to the channel deployment site using a benthic grab. In the laboratory, these sediments were mixed in varying levels for calibration purposes. A known quantity of sediment was added to a calibration chamber, where it was maintained in suspension under constant stirring. Each transmissometer was placed in the calibration chamber for roughly one minute to record optical transmission. For each concentration level, water samples were collected and filtered to obtain the mass concentration. A linear calibration between the measured light attenuation and mass concentration was then performed for each instrument in order to obtain estimates of suspended sediment concentration during the experiment.

Each of the transmissometers was equipped with a wiping device that cleaned the optics prior to recording each sample. While the wipers prevented significant biofouling of the instruments, some gradual biofouling was detected during the course of the experiment. In order to remove this effect, a logarithmic curve was fit to the light transmission data during slack water at the beginning and end of the experiment. This

logarithmically increasing minimum concentration was then removed by subtracting this curve from the data. This procedure assured the time variation of the minimum concentration observed during slack water by the transmissometer was well correlated with the time variation of the minimum in acoustic backscatter from the ADCP, which was also used to estimate suspended sediment concentration.

Both the RDI ADCP and Sontek ADP record echo intensity (E) at every depth bin. In order to estimate of suspended sediment concentration, E which is measured in counts and is proportional to the logarithm of power, must be converted to decibels (dB) by the factor K_c . Following Deinnes (1999) the sonar equation can be represented as:

$$S_v = C_o + 20\log_{10}(R) + 2\alpha R + K_c(E) \quad (4-1)$$

where S_v is the acoustic backscatter in dB, C_o is a linear calibration constant that encompasses a number of factors including transmit pulse length, transmit power, and system noise. The loss of acoustic energy due to spherical spreading and the attenuation due to water are represented by the second and third terms on the right hand side of the equation, where R is range along the beam to the scatterers (m) and α is absorption coefficient of water (dB/m). The coefficient K_c is unique to each instrument, but has a reported range of values of 0.35 to 0.55 dB/Bit (Deinnes, 1999). In order to estimate K_c for each instrument, we assume that there periods of vertically uniform scattering during slack water when the vertical differences in E are solely to the spreading and attenuation terms. Because of possible errors associated with additional attenuation due to suspended sediment (Thorne and Hanes, 2002), values of K_c were estimated near the bed where attenuation is minimal. This method resulted in $K_c = 0.52$ for both the ADCP and ADP. Using K_c , E was then converted to dB and range corrected.

Previous work suggests that there is a consistent relationship between the concentration of fine sediment in estuaries (C in mass per volume) and the acoustic backscatter of the form (Holdaway et al., 1999; Fugate and Friedrichs, 2002):

$$C = A 10^{\beta Sv} \quad (4-2)$$

where A and β are calibration coefficients. Figure 4-2a, shows the best fit least squares regression between concentration estimate from the transmissometer at the channel location, deployed 3.1 mab and the acoustic backscatter measured by the ADCP at a vertical adjacent bin. Figure 4-2b, shows the same relationship for the shoal site, between the transmissometer 2.1 mab and the acoustic backscatter measured by the ADP at a vertical adjacent bin. For both the ADCP and ADP data there is a relatively high correlation between the acoustic backscatter and the \log_{10} of the concentration as estimated by the adjacent transmissometer ($r = 0.82$ and 0.80 , respectively).

Just as the backscatter from the ADCP and ADP can be calibrated, so can the echo intensity of the ADVs. In fact, because no range correction is necessary to adjust the point measurement of the ADV, the procedure is relatively simple. On the main channel tripod, the lowest ADV and transmissometer were roughly located at the same height above the bed. A simple empirical calibration was performed according to equation (4-2). A similar calibration was performed for the highest ADV. However, because there was no vertically adjacent transmissometer, the concentration profile obtained from the ADCP had to be interpolated down to the height of the upper ADV. This was done using a second order polynomial. Because the profiles were only extrapolated over roughly 0.40 meters, the estimate was relatively insensitive to the method of extrapolation. Figures 4-2c and 4-2d show the best fit least squares regression for the

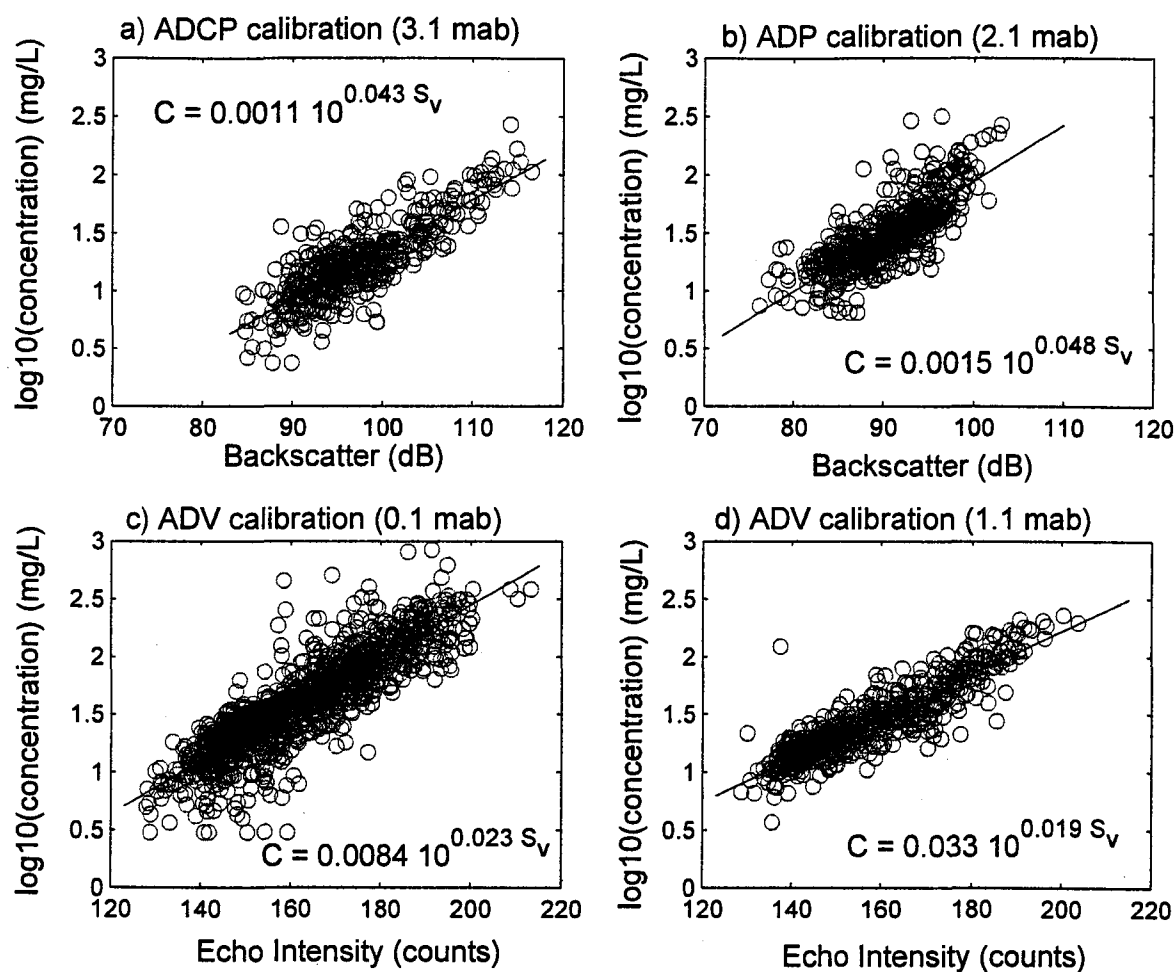


Figure 4-2. Sediment calibration curves for acoustic backscatter from a) ADCP (channel); B) ADP (shoal); c) ADV 0.1 mab (channel); d) ADV 1.1 mab (channel). All calibration curves are plotted against concentration values obtained from co-located transmissometers, except the ADV 1.1 mab, which was calibrated against concentration values obtained from the ADCP.

calibration of the ADVs deployed 0.10 and 1.1 mab at the channel site ($r = 0.87$ and $r = 0.90$, respectively).

4.3 RESULTS

The 2003-04 experiment took place during a period of elevated rainfall. Discharge from the York River tributaries for December 2003 was, on average, nearly 3 times the 60-year average (Fig. 4-3a). The experiment spanned approximately 30 days, covering the full spring-neap tidal cycle. The spring-neap cycle was apparent in the both the depth-averaged current magnitude (Fig. 4-3b) as well as the depth-averaged suspended sediment concentration at both the channel (Fig. 4-3c) and shoal (Fig. 4-3d) locations. With the elevated river discharge, there was persistent vertical density stratification throughout much of the experiment at both the channel and shoal sites, especially during neap tide (Fig. 4-3e). The vertical stratification exceeded 2 kg/m^4 on several occasions at both locations, and median values of stratification measured between the upper-most and lower-most sensors were 0.88 and 0.58 kg/m^4 at the channel and shoal sites, respectively. In addition, significant tidal asymmetries in stratification were observed at both locations. At the channel site, the median stratification on flood and ebb was 0.81 and 0.94 kg/m^4 , respectively. The asymmetry had the opposite sense at the shoal site, where the flood was actually more stratified on average than the ebb (0.65 and 0.53 kg/m^4).

With co-located estimates of sediment concentration and current velocity, it is straightforward to estimate sediment flux. Although there is stronger residual outflow over the channel site (Fig. 4-4a), the sediment flux is more strongly seaward

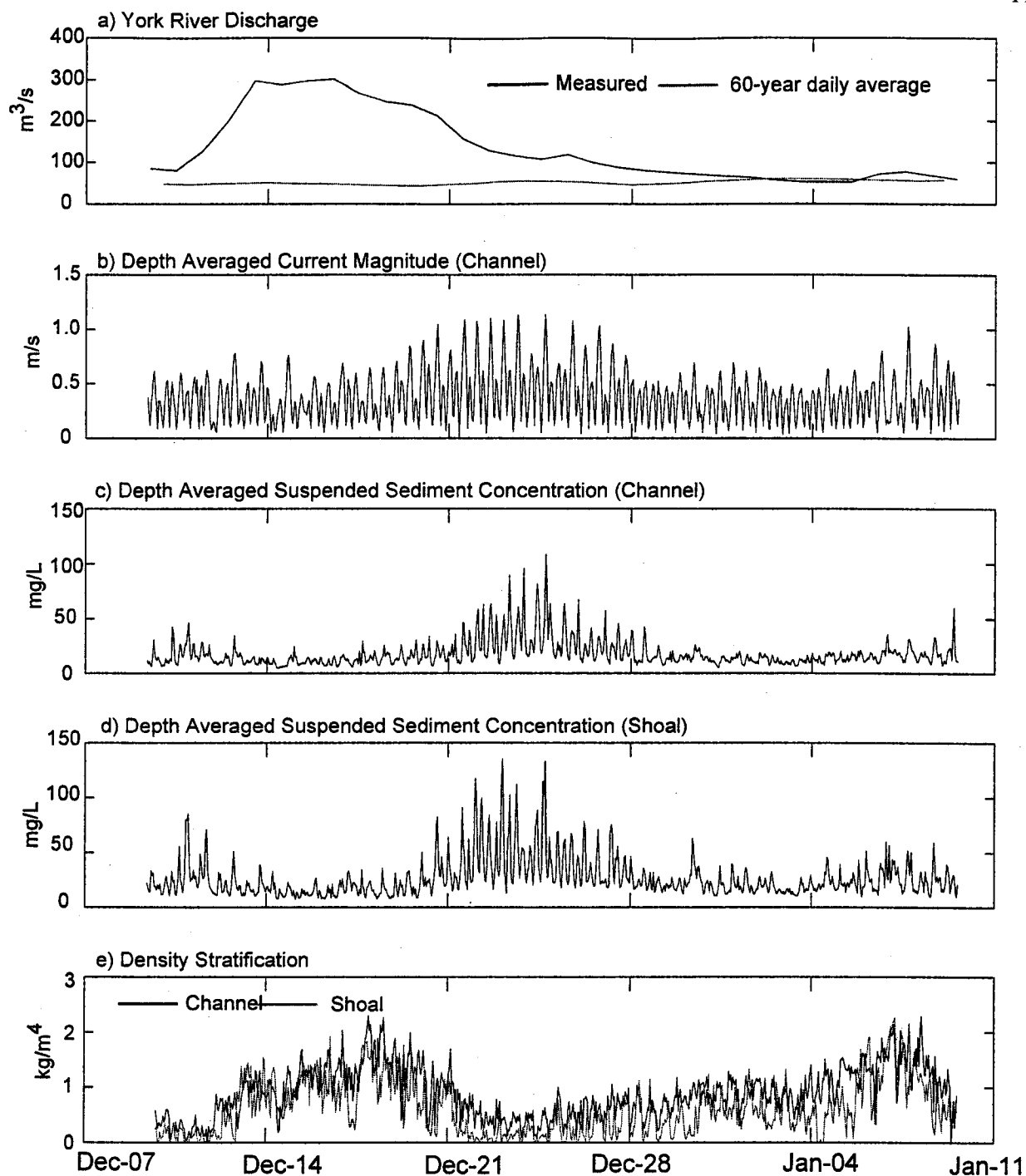


Figure 4-3. Time series data December 2003—January 2004: a) combined daily river discharge from United States Geological Service's Mattaponi and Pamunkey gauging stations, with 60-year daily average; b) depth-averaged current magnitude measured by ADCP at the channel site; c) depth-averaged sediment concentration measured by calibrated ADCP backscatter at the channel site; d) depth-averaged sediment concentration measured by calibrated ADP backscatter at the shoal site; e) density stratification measured between the highest and lowest CTDs at the channel site (dark line) and the shoal site (light line).

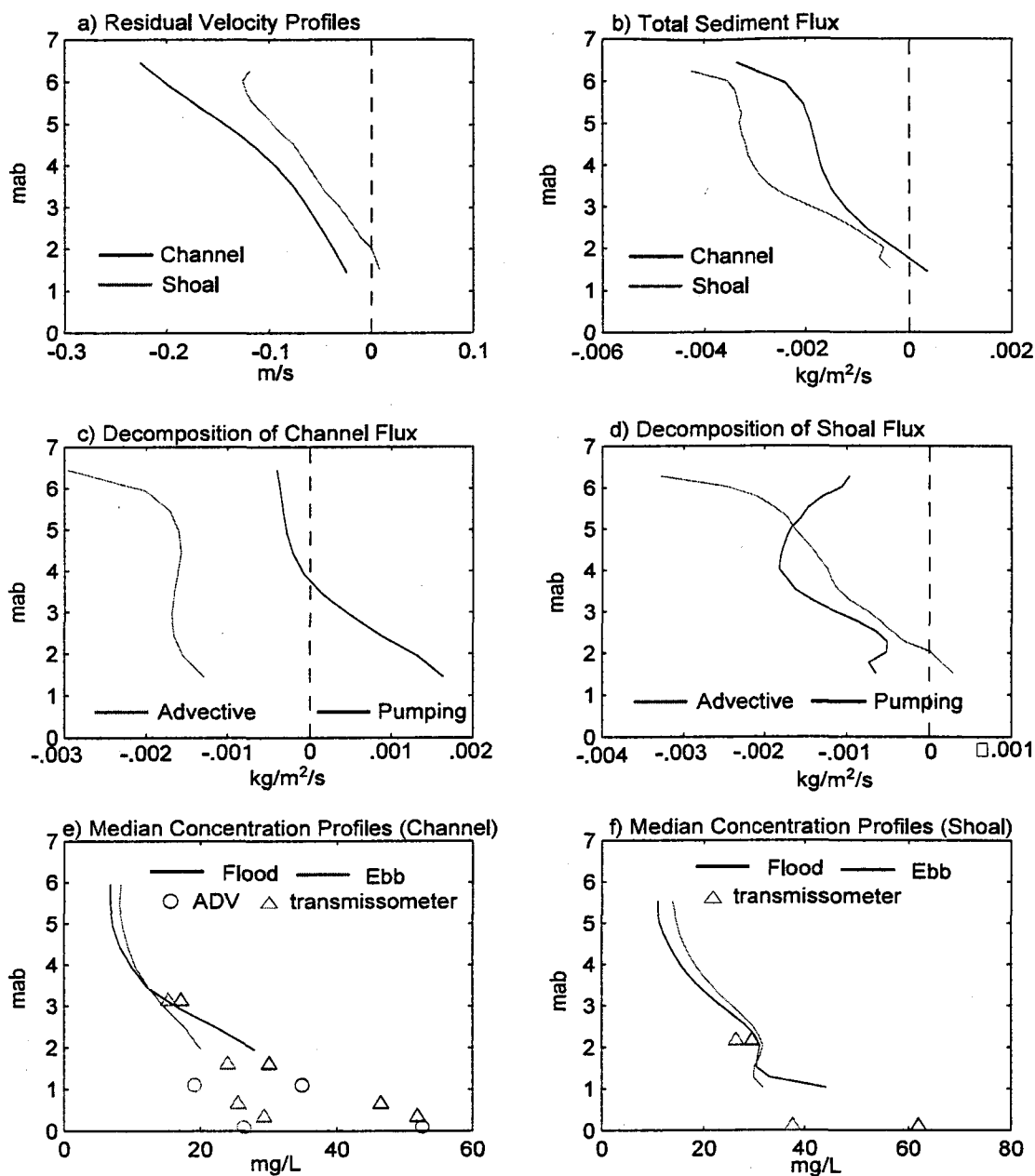


Figure 4-4. a) Depth averaged along-channel velocity profiles measured by ADCP at the channel site (dark line) and ADP at the shoal site (light line); b) depth averaged along-channel sediment flux profiles measured by ADCP at the channel site (dark line) and ADP at the shoal site (light line); c) depth averaged profiles of sediment pumping flux (dark line) and advective flux (light line) at the channel site; d) depth averaged profiles of sediment pumping flux (dark line) and advective flux (light line) at the shoal site; e) tidally-averaged sediment concentration profiles for flood (dark line and symbols) and ebb (light line and symbol) at the channel site obtained from calibrated ADCP (lines). Circles represent values obtained from calibrated ADV backscatter and triangles represent values from calibrated transmissometers; f) tidally-averaged sediment concentration profiles for flood (dark line and symbols) and ebb (light line and symbol) at the shoal site obtained from calibrated ADP (lines). Triangles represent values from calibrated transmissometers.

directed at the shoal location (Fig. 4-4b). Figure 4-4b, shows the average profiles of sediment flux for the channel and shoal sites, using the ADCP and ADP concentration and velocity data. To examine these patterns in more detail, the sediment flux can be divided into an advective flux and a pumping flux, similar to the methods used by Geyer et al. (2001). The advective flux is driven by the tidally averaged velocity and tidally-average concentration, given as:

$$Q_A = \langle U(z) \rangle \langle C(z) \rangle \quad (4-3)$$

where U is the along-channel velocity, C is the suspended sediment concentration, and the angled brackets denote tidal averages (tides were removed using a 35-hour lowpass filter). The pumping flux is then given as:

$$Q_P = u'(z) c'(z) \quad (4-4)$$

where the primes indicate the deviations from the tidally-averaged values. This decomposition of the flux enables us to more closely examine the processes driving sediment flux at the two locations. Figures 4-4c and 4-4d show the profiles of the advective and the pumping sediment flux, averaged over the deployment, for both channel and shoal locations, respectively. At the channel location, although the average advective flux is down estuary throughout the water column, the pumping flux is directed up estuary near the bed. In fact, the magnitude of the pumping flux is greater than the advective flux near the bed, resulting in a net up-estuary transport of sediment as measured by the lowest bin of the ADCP. At the shoal location, both the advective and pumping fluxes are directed down-estuary.

The up-estuary sediment pumping observed near the bed at the channel location is driven by tidal asymmetries in sediment resuspension. Figure 4-4e shows profiles of the

median sediment concentration for both the channel and the shoal location, segregated by the phase of the tide. Despite larger velocities on the ebb phase of the tide at the channel location, sediment concentrations are significantly greater during the flood phase of the tide. At the shoal location the pattern is less clear (Fig. 4-4f). Although concentrations appear to be greater on the flood near the bed, they are greater on ebb higher in the water column. At the shoal location, where the flood tide was slightly more stratified on average than the ebb, the net sediment pumping is ebb directed. In chapter 2, the dominant terms in the axial momentum balance were used to estimate vertical profiles of eddy viscosity for both the channel and shoals locations. Figure 4-5 shows the profiles of eddy viscosity, segregated by the phase of the tide, as well as for spring and neap tidal conditions. At the channel location, there is a clear tidal asymmetry in eddy viscosity, with larger values reported for the flood tide. This asymmetry is particularly pronounced during spring tidal conditions and exists despite the fact that strong down estuary residual flows are reported during this period. At the shoal location, there is no pronounced asymmetry in the eddy viscosity profiles, and the suspended sediment profiles do not exhibit the strong tidal asymmetry observed in the channel.

The impact that the tidal asymmetry in eddy viscosity has on sediment pumping is clearly evident when examining the time series of sediment pumping in figure 4-6. Figure 4-6 shows the time series of the depth integrated total flux, advective flux and pumping flux at both the channel and shoal sites. As expected, the magnitude of total sediment flux is greatest at both locations during the spring tide. In fact, the overall flux is very similar between the two locations. However, during the spring tides the advective flux and pumping flux measured at the channel site are in the opposite direction of the

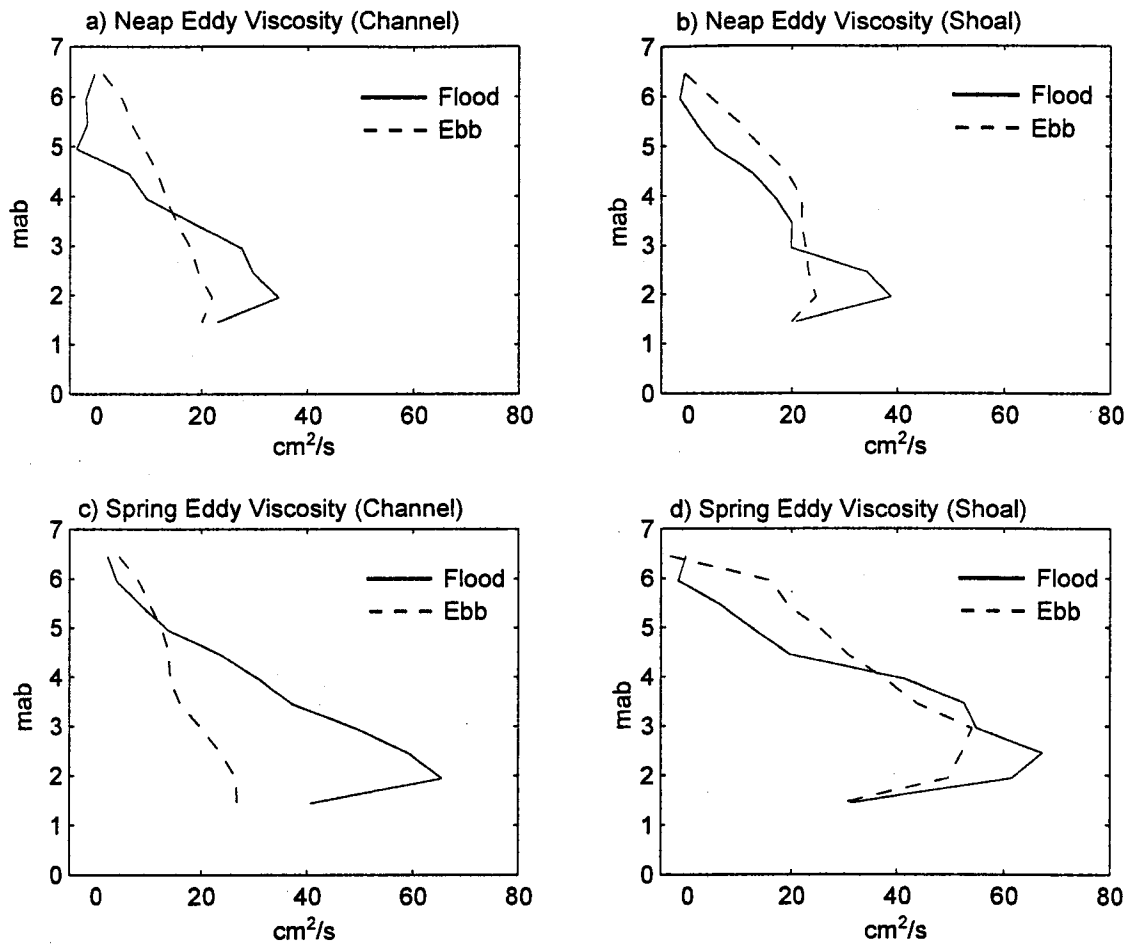


Figure 4-5. Median profiles of the eddy viscosity (from chapter 2) estimated from the momentum integral for both channel and shoal sites during spring and neap tidal conditions (solid line denotes flood and dashed line denotes ebb).

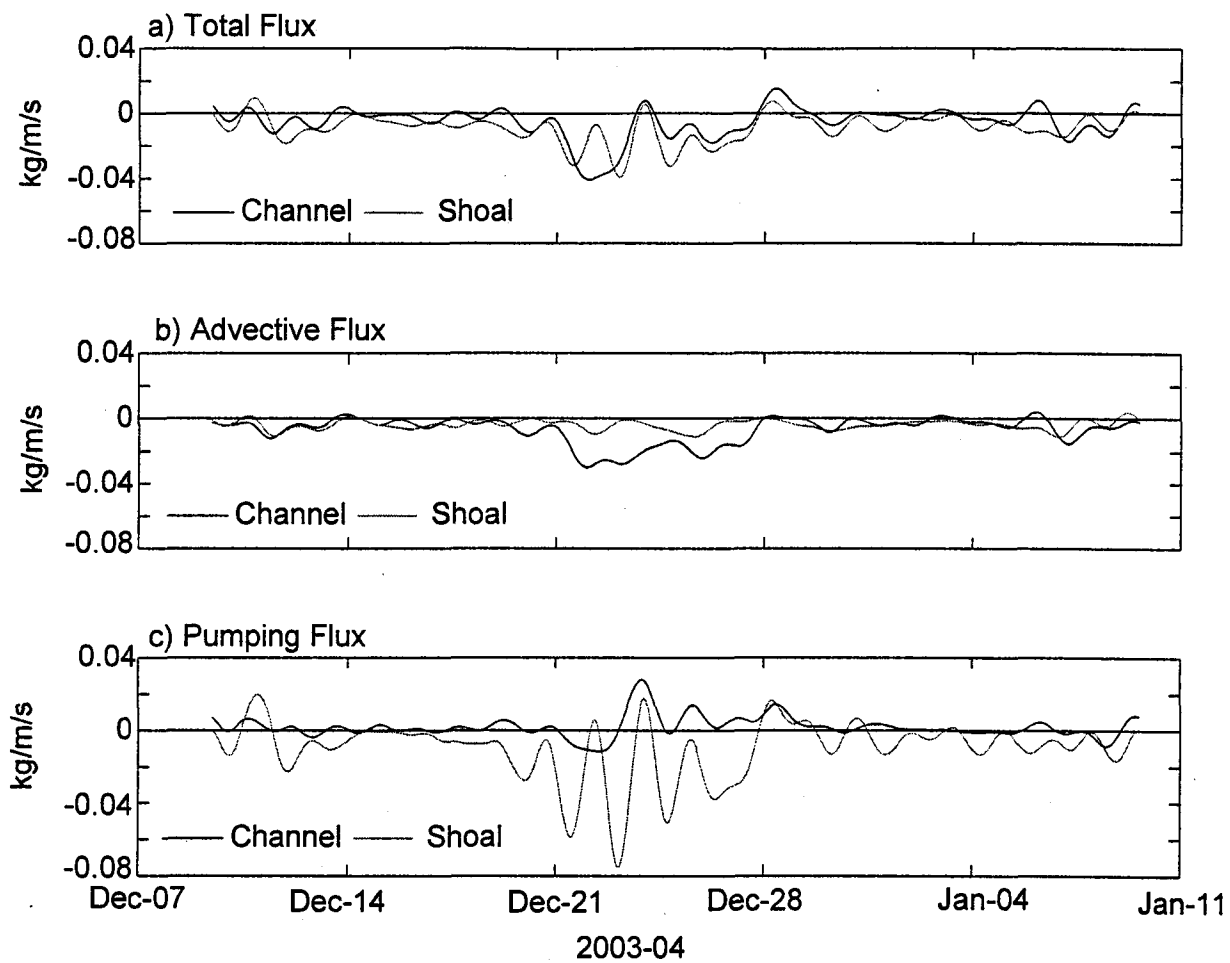


Figure 4-6. Time series of depth integrated a) total sediment flux; b) advective sediment flux; and c) pumping sediment flux (dark lines represent the channel site and light lines represent the shoal site).

fluxes measured at the shoal location. At the channel location, the strong down-estuary advective flux is offset and even at times reversed by the up-estuary sediment pumping, while the opposite trend is observed at the shoal. The opposite sense of the advective and pumping sediment fluxes is largely a consequence of tidal asymmetries in stratification. During the ebb tide at the channel location, the increased stratification damps turbulent mixing, limiting sediment resuspension. The preferential damping of turbulence during the ebb tide at the channel location enhances up-estuary sediment pumping.

It is interesting to note that the pumping term is net seaward directed above 4 mab at the channel location. Sediment pumping due to tidal asymmetries in mixing is driven by sediment resuspension. With the relatively stratified conditions observed during this experiment, sediment resuspension was limited to the lower portion of the water column, mostly below the pycnocline. As a result, sediment pumping due to tidal asymmetry was mainly limited to this region. The net seaward-directed sediment pumping above the pycnocline is not caused by resuspension, but probably represents preferential advection of higher turbidity water from upstream.

4.4 DISCUSSION

4.4.1 The Impact of Tidal Asymmetries on the Advective Flux

Sediment pumping as expressed in equation (4-4) is driven by tidal asymmetries in resuspension. If the vertical profiles of suspended sediment were identical between flood and ebb, there would be no flux due to pumping and all of the flux would follow the mean flow. However, the presence of a residual mean circulation suggests an inequality in bed stress that also could lead to tidal asymmetries in sediment resuspension. This asymmetry in bed stress would appear as a pumping flux as defined

by equation (4-2), but would not be the result of an internal asymmetry in mixing as described by Jay and Musiak (1994). This pattern of sediment flux would result in a positive correlation between advective and mean flux. However, this is not the pattern observed at the channel location, where the pumping flux is directed up-estuary while the mean flux is directed down-estuary. Because the advective and pumping fluxes have the opposite sign at the channel location, it is unlikely that the pumping flux is the result of tidal asymmetries in bed stress.

Previous authors have demonstrated how the reduced stratification during the flood phase of the tide can enhance sediment resuspension, resulting in an up-estuary pumping of sediment (Jay and Musiak, 1994; Chant and Stoner, 2001; Scully and Friedrichs, 2003). As discussed by Scully and Friedrichs (2003), tidal asymmetries in mixing do not impact the bed stress directly, just the overlying eddy viscosity (and presumably the eddy diffusivity), which controls the vertical distribution of sediment through out the water column. Thus, in estuaries that experience the expected pattern of tidal straining, this internal asymmetry in mixing would enhance up-estuary sediment pumping. However, the results from chapter 2 demonstrate how tidal asymmetries in mixing also can impact the advective sediment flux term. These results show that in estuaries with shoal and channel morphologies, significant lateral asymmetries in mixing allow tidal straining to increase the vertical velocity shear during the ebb phase of the tide and favor down-estuary flow over the channel regions. As a result, tidal asymmetries in mixing caused by tidal straining will have the opposite impact on the advective and pumping sediment flux. While the increased stratification during ebb increases the vertical velocity shear and increases the down-estuary advective flux, the increased eddy

viscosity on the flood tide favors sediment resuspension higher in the water column where currents are stronger, increasing up-estuary sediment pumping. This process appears to be what is driving the strong divergence between the advective and pumping flux that is observed during the spring tide at the channel location. The same strong divergence is not noted at the shoal site, where relatively weak asymmetries in internal mixing were observed. This strong divergence would not be expected in systems with more uniform lateral bathymetry. As discussed in chapter 2 and first shown by Jay and Musiak (1994), tidal asymmetries in mixing can increase the two layer residual circulation, increasing the up-estuary flux of both the advective and pumping terms. However, because this process involves the response of residual barotropic pressure gradient, it impacts the tidal asymmetries in bed stress as well as overlying asymmetries in mixing.

4.4.2 Influence of Sediment Availability

Tidally asymmetries in sediment resuspension may be simply manifestations of tidally asymmetries in bed stress, driven by the residual mean circulation. Such an asymmetry would contribute to the pumping flux and would be positively correlated with the mean flux. However, this contribution to the pumping flux could be negated if the amount of sediment available for resuspension in the bed is limited. Under supply-limited conditions, tidal asymmetries in bed stress may not lead to commensurate asymmetries in resuspension. During the spring tide the ADV data at the channel site suggests that the residual stress is ebb-directed (chapter 2). In the absence of supply-limitation, this asymmetry in stress should increase the resuspension on ebb and help offset the sediment pumping due to the overlying internal asymmetry. However, there is

a strong divergence between the advective and pumping fluxes at the channel site during the spring tide, suggesting that the increased stress on ebb is not driving asymmetries in resuspension that are leading to down-estuary pumping. In contrast, at the shoal location the asymmetry in bed stress does appear to contribute greater resuspension during the ebb and both the advective and pumping fluxes are directed down-estuary during the spring tide.

The ADV data that was collected 0.12 mab at the channel site is used to further investigate the role that sediment erodibility plays in the observed patterns of sediment flux. This data provides both a direct measure of the bed stress, as well as an estimate of the concentration very close to the bed. Although the results from chapter 2 demonstrated that stratification can impact the relationship between stress and velocity, even over the lower meter of the water column, we assume that the stress and concentration data 0.12 mab are relatively unaffected by the overlying stratification. This enables us to more closely examine the relationship between bed stress and a bed reference concentration independently from any overlying internal asymmetry. Figure 4-7a shows a plot of the bed stress against the concentration, as measured by the ADV. Flood and ebb data are plotted separately. At lower values of stress, there is clearly a positive relationship between the bed stress and near-bed concentration. However, once a stress of approximately 0.3 Pa is exceeded, there is no clear positive correlation. In fact, a linear regression yields a negative slope when fit to all data above 0.3 Pa. This pattern clearly suggests that the resuspension of sediment, particularly under higher stress conditions, is supply limited. Because the residual stress tended to be ebb directed during

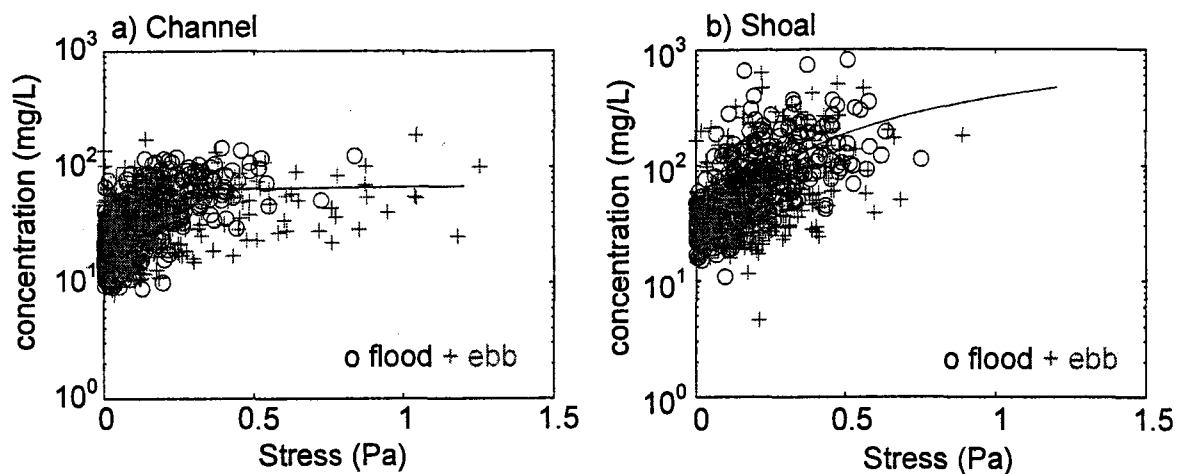


Figure 4-7. Bed stress vs. concentration measured 0.10 mab for a) Channel site; and b) Shoal site. Circles indicate flood and crosses indicate ebb. Stress at the channel site was measured by the ADV 0.12 mab and stress at the shoal site was estimated using a drag coefficient (0.0023) and quadratic velocity measure 1.0 mab. Lines indicate a linear regression fit to all data where the stress exceeded 0.3 Pa.

high stress conditions, supply-limitation prevents a significant asymmetry in resuspension that would favor down-estuary sediment pumping.

Unfortunately, no direct estimates of stress were available at the shoal location. However, we can estimate stress using a quadratic drag relationship and examine the potential for supply limitation and the shoal location. Figure 4-7b plots the quadratic stress estimated using the ADP velocity measured approximately 1 mab and the drag coefficient estimated in chapter 2, against the concentration estimate from the lowest transmissometer (0.10 mab). In contrast to the results shown in figure 4-7a, at the shoal location there is a consistent increase in near-bed concentration with increasing stress, even at the higher levels of stress. It should be noted, that the drag coefficient used to estimate stress is sensitive to changes in stratification, so these results should be interpreted with caution. However, it does not appear that supply-limitation is significantly impacting the shoal location, providing an explanation for why the pumping and advective terms are in the same direction at this site.

The patterns of sediment flux observed appear to be influenced by long-term changes in bed erodibility. A relatively simple way of evaluating erodibility is to assume that the sediment concentration (C_a) near the bed is related to the bed stress (τ_b), multiplied by some constant (γ):

$$C_a \propto \gamma \tau_b \quad (4-5)$$

This is a simplification of a complex process, but is analogous to the reference concentration approach commonly used to model sediment transport (Smith and McLean, 1977). However, because we don't know the critical erosion threshold, which changes with both time and depth into the bed, we lump all of the changes in erodibility into a

single coefficient (γ). This provides a simple way of looking at temporal changes in erodibility.

The parameter γ can be estimated from the ADV estimates of stress and concentration measured by the lowest sensor at the channel location. Estimates of γ are noisy because we are often dividing by number that is approaching zero. To try to remove this effect, the bed-stress and concentration were both smoothed using a 96-hour running median. The time-series estimate of γ using the smoothed data is shown in figure 4-8a. The estimate of γ exhibits significant temporal variability, changing by a factor of 4 over time scales shorter than spring-neap cycle. The changes in γ are positively correlated with changes in the bed elevation (figure 4-8b) as measured by the altimetry feature of the ADV ($r = 0.70$), suggesting that the sediment becomes increasingly more difficult to erode with depth into the bed. During the period from 18-Dec to 28-Dec, approximately 2 cm of sediment appear to be removed from the bed. During this period, there is a steady decrease in γ suggesting the underlying sediment is more consolidated and more difficult to remove. Bed elevation increases slightly from 12/28/03 to 1/7/04, which is accompanied by an increase in the erodibility as parameterized by γ .

The increase in erodibility with depth, leads to a hysteresis effect during spring tidal conditions. During the beginning period of the spring tide, when stress is increasing, the easily eroded sediment is removed from the bed. As a result, less sediment can be eroded for a similar value of stress during the second half of the spring tide, when stress is decreasing. This hysteresis appears to significantly impact the processes governing sediment pumping. During the early portion of the spring tide, when tidal energy is still increasing, supply-limitation is not significant, and asymmetries in

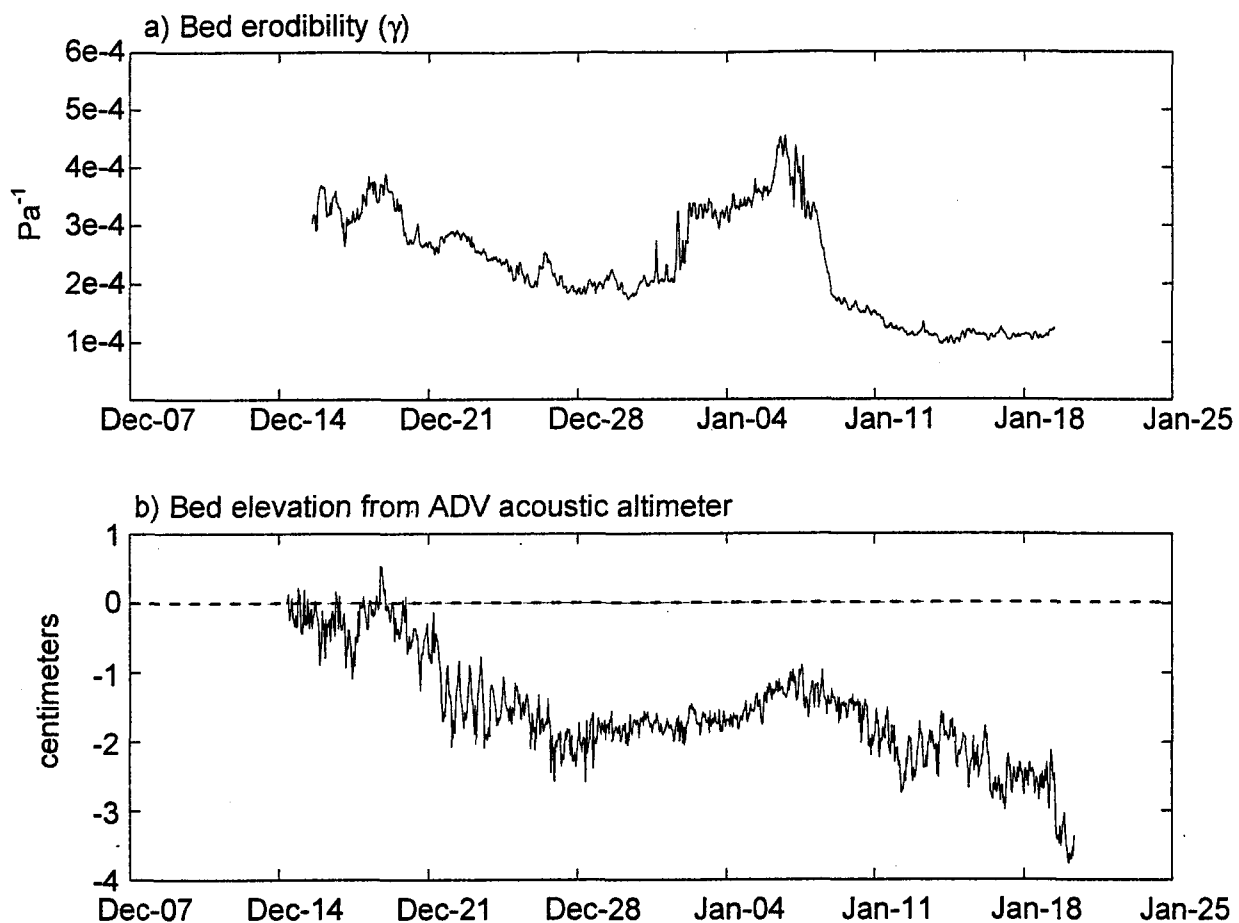


Figure 4-8. a) Sediment erodibility estimated at the channel location, using ADV concentration and stress measured 0.10 mab; b) Bed elevation measured by the acoustic altimetry feature of the ADV 0.10 mab.

bed stress can lead to asymmetries in resuspension. The residual stress is ebb directed and this early portion of the spring tide is the only period when significant down-estuary sediment pumping is observed at the channel location. During the second half of the spring tide when the residual stress is still ebb directed, supply limitation negates the impact of the asymmetry in bed stress and sediment pumping is dominated by the overlying internal asymmetry. It is during this period of decreasing stress when the greatest up-estuary sediment pumping occurs. Because the amount of sediment resuspended near the bed is controlled by its availability and not by the magnitude of the stress, the stronger bed stress on the ebb tide does not contribute to down-estuary sediment pumping. The up-estuary pumping is driven by the overlying eddy viscosity, which is larger on flood because of tidal straining. This hysteresis effect is not seen at the shoal location, and as a consequence, the sediment pumping term is directed down estuary, consistent with the asymmetry in bed stress.

The erodibility of the bed is constantly changing as shown in figure 4-8. Both erosion and deposition occur at tidal time scales, leading to significant changes in erodibility over short time scales. While the data presented in figure 4-8 presents evidence for the importance of supply-limitation, its treatment here is relatively simplistic. Closer examination of the altimetry data from the ADV reveals a clear tidal periodicity to the bed elevation, particularly during energetic spring tides. In fact, the changes in bed elevation are positively correlated with the cumulative estimates of sediment flux calculated using the velocity and backscatter data from the ADCP (Fig. 4-9). Unfortunately the across-estuary orientation of the instrumentation in this experiment does not allow us to examine along-estuary processes that in all likelihood control the

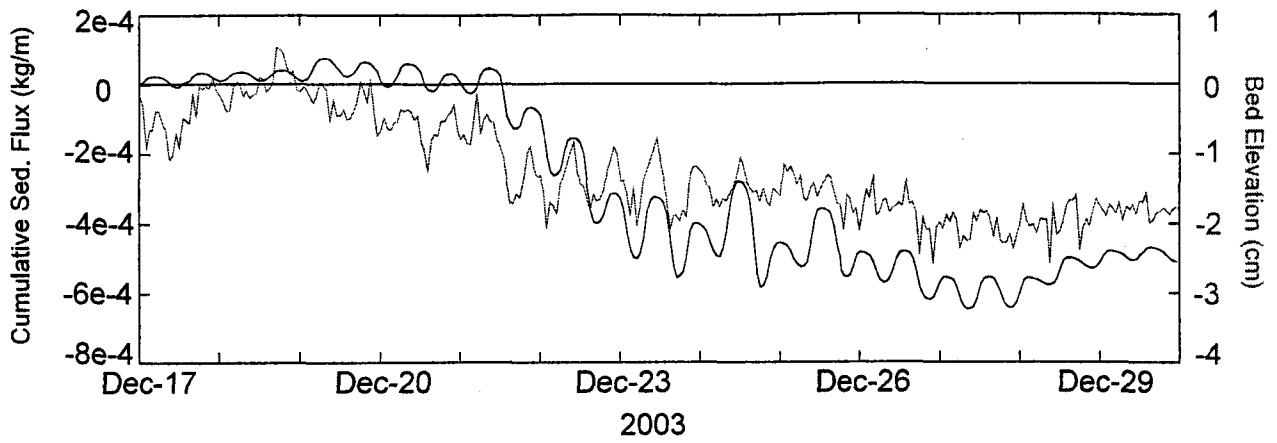


Figure 4-9. Comparison of the depth integrated cumulative sediment flux measured by the ADCP at the channel site (dark line--left axis) and the bed elevation measured by the acoustic altimetry feature of the ADV 0.10 mab (light line-right axis).

convergence of sediment flux and hence deposition. However, figure 4-9 demonstrates that at the channel location, deposition is favored during the flood and erosion is favored during the ebb. Even these slight changes in bed elevation may significantly impact the erodibility of the sediment. In fact, the greater sediment resuspension during the flood tides, despite higher stresses during ebb, could be the result of changes in erodibility occurring at the tidal time scale.

4.4.3 Fall Velocity

The results of Scully and Friedrichs (2003) demonstrate that tidal asymmetries in internal mixing lead to sediment pumping by controlling the vertical distribution of sediment in the water column. Changes in the sediment fall velocity also can have a significant impact on the vertical distribution of sediment. In estuaries with fine cohesive sediments, sediment particles often exist in loosely bound aggregates (Eisma, 1986). While the processes that control the aggregation and disaggregation of particles are complex, there is evidence that the level of turbulent shear significantly impacts flocculation dynamics. The results of Kranck and Milligan (1992) demonstrate an inverse relationship between the level of turbulence and floc diameter. Thus the internal asymmetry in mixing caused by changes in stratification may impact the vertical distribution of sediment not only through its impact on the eddy diffusivity, but also by altering the sediment fall velocity.

Fugate and Friedrichs (2002) used calibrated ADV backscatter to estimate the fall velocity of aggregated estuarine particles. This method assumes that at first order the concentration of suspended sediment at a given height above the bed can be represented as a balance between the downward settling flux and the upward turbulent diffusive flux:

$$-w_s \langle c \rangle = \langle c' w' \rangle \quad (4-6)$$

where w_s is the sediment fall velocity, c is concentration, w is vertical velocity, and the primes denote fluctuations from the mean, which is denoted by the angled brackets. The slope of a linear regression between the turbulent diffusive flux and the concentration as measured by the ADV, gives an estimate of the fall velocity. This method was applied, and figures 4-10a and b plot the relationship between the estimated turbulent diffusive flux and the concentration measured by the ADVs 0.12 and 1.06 mab, respectively. Values for flood and ebb are plotted separately. Because the data are somewhat noisy, they were grouped into roughly 6 equally spaced bins based on the concentration, and the median values are plotted in figure 4-10c. In figure 4-10c, both flood and ebb data plotted using different symbols, as are the data from the two different ADVs. In both the binned and non-binned data, estimates of the fall velocity are higher during ebb than they are during the flood. Estimates from linear regressions fit to the binned data give fall velocity values of 2.0 and 1.3 mm/s for ebb and flood, respectively. These values are significantly higher than would be expected for the disaggregated fine sediment found in the York River, suggesting that much of the sediment is packaged as flocculated aggregates.

Given the evidence for an internal asymmetry in turbulent mixing (figure 4-5), it is possible that the inferred tidal asymmetries in the fall velocity could be the result of asymmetries in turbulent mixing caused by the changes in stratification. During the less stratified and more turbulent flood tide, greater break up of the aggregated particles may occur, resulting in a lower settling velocity. Because the non-settling background concentration changes over meteorological time scales (Fugate and Friedrichs, 2002), it is

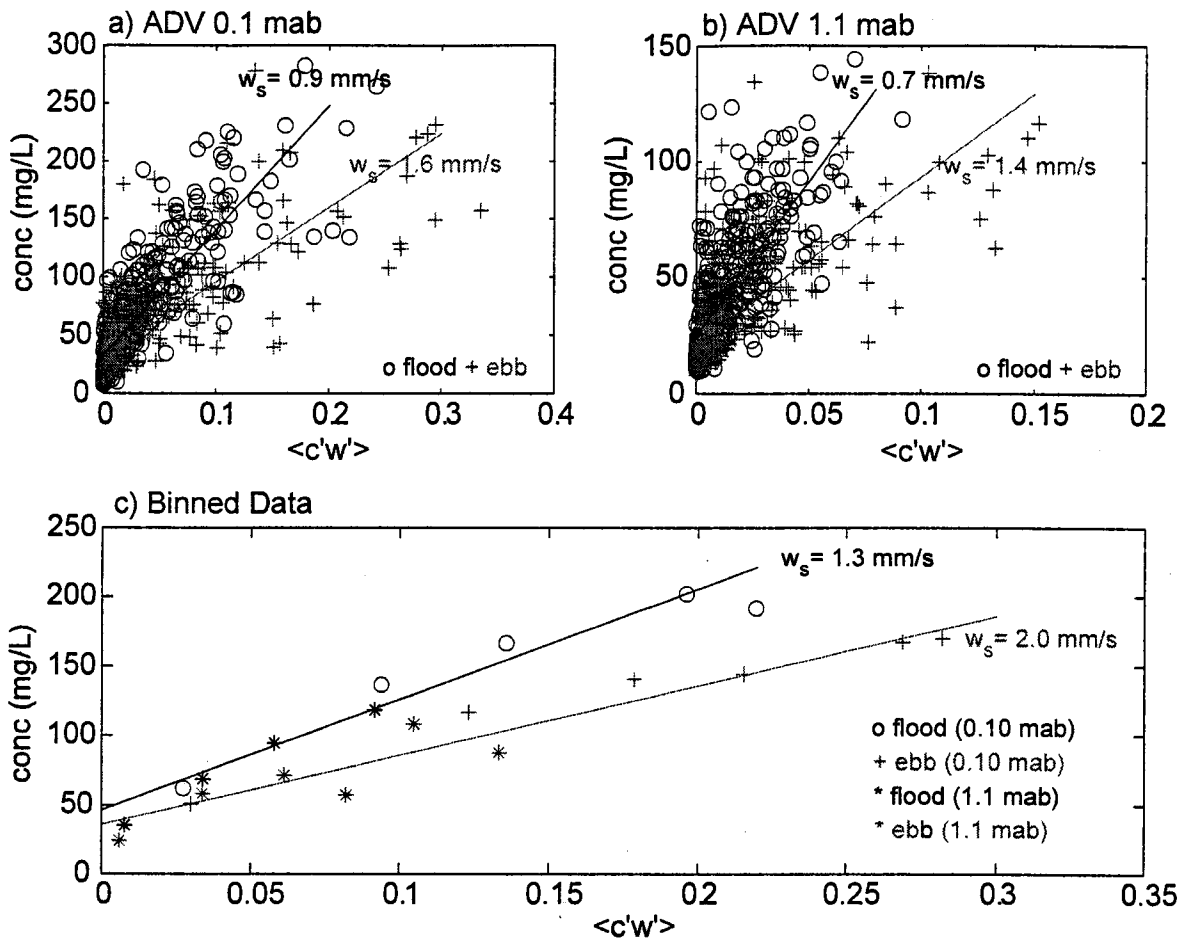


Figure 4-10. Estimate of fall velocity from ADV data obtained by regressing the turbulent diffusive sediment flux against concentration as measured by the ADVs a) 0.10 mab; b) 1.1 mab; c) after binning data from each ADV into equal increments based on concentration.

difficult to directly solve equation (4-6) to examine the temporal behavior of the estimated fall velocity. However the non-integrated form of the sediment conservation equation can be used if you assume that there are no vertical gradients in the slowly settling background concentration:

$$dc/dt = -w_s dc/dz - d/dz \langle c'w' \rangle \quad (4-7)$$

With estimates of concentration and diffusive sediment flux at two heights, equation (4-7) can be used to estimate the time series of sediment fall velocity, without bias from the background non-settling wash load. Figure 4-11 shows the time series of w_s , estimated from the ADV data collected at the main channel. The estimates of w_s from equation (4-7) are noisy, so the time series was smoothed using a 50-hour lowpass filter. Prior to smoothing all negative values and values which exceeded 10 mm/s were removed and substituted with values from a simple linear interpolation of the time series. As a result, roughly 30 percent of the data were excluded, usually occurring during periods of low current velocity when the vertical concentration gradient was very small. The smoothed values of w_s range from 0.2 to 3.6 mm/s, consistent with previously published values for flocculated estuarine particles (Milligan et al., 2001). The smoothed time series of w_s exhibits a weak positive correlation with the overall degree of density stratification ($r = 0.35$), suggesting that level of turbulent shear is playing some role in controlling the size of the flocculated particles at sub-tidal time scales.

Another method for inferring information about the state of the suspended sediment particles is to examine the ratio of the acoustic estimate of sediment concentration to that obtained using the optical transmissometer. It is well established that for optical instruments the backscattering signal is proportional to geometrical cross

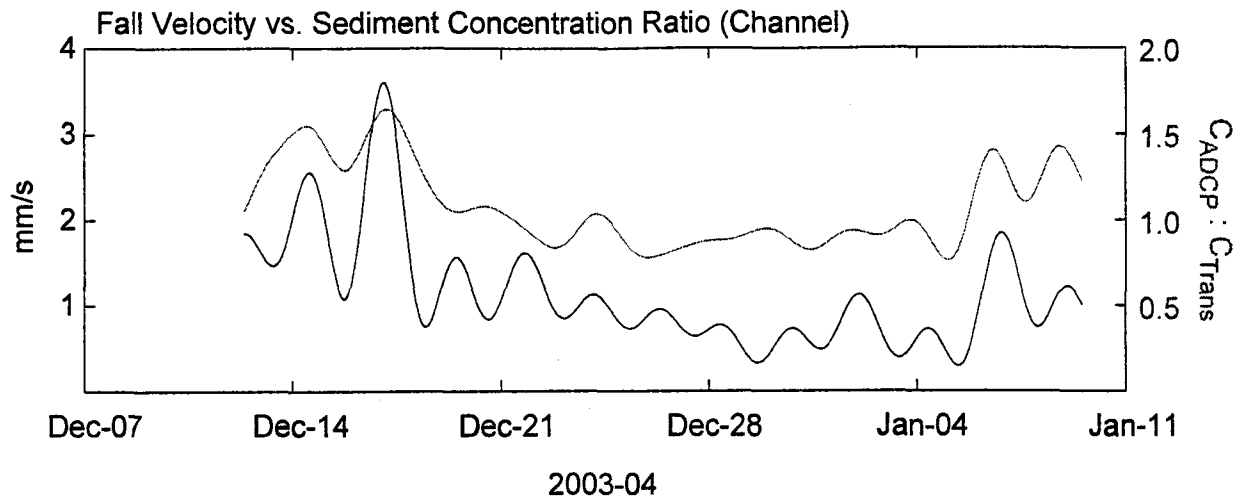


Figure 4-11. Comparison of smoothed time-series (50-hour lowpass filter) of fall velocity (dark line--left axis) and the ratio of ADCP concentration to transmissometer concentration measured 3.1 mab (light line--right axis).

section of the suspended particles, whereas backscattering from acoustic sensors is proportional to the particle volume squared. Therefore the ratio of the acoustic backscatter to the optical backscatter is proportional to the particle radius to fourth power (Lynch et al., 1997). With vertically co-located acoustic (ADCP) and optical (transmissometer) estimates of concentration, it is possible to examine the time series of this ratio. Figure 4-11 shows the time series of the ratio of the concentration measured by the ADCP to the concentration measured by the transmissometer, both located roughly 3 mab. Consistent with the time series estimate of w_s , the acoustic to optical concentration ratio was smoothed with a 50-hour lowpass filter. During the more stratified conditions, the ratio is consistently above unity, while under the more energetic mixed conditions, the ratio is below unity. Because the acoustic estimates of sediment respond more strongly to the larger flocculated particles, whereas the optical estimates respond more strongly to the finer un-flocculated particles, the time series of the concentration ratio suggests that suspended population consists of either a greater proportion of aggregated particles, or larger aggregated particles, during stratified conditions. Additionally, the high correlation between the concentration ratio and the estimate of the fall velocity ($r = 0.85$) provides confidence in the validity of the fall velocity estimate.

Turbulent energy is generated by large scale turbulent eddies and dissipated by viscosity at very small scales. As the level of turbulence increases, dissipation is driven to smaller and smaller length scales. The length scale of the smallest turbulent eddies is often presented as the Kolmogorov micro scale:

$$\eta = (\nu^3/\epsilon)^{1/4} \quad (4-8)$$

where ν is the kinematic viscosity of water and ϵ is rate of turbulent dissipation. A number of authors have suggested that the Kolmogorov micro scale sets the upper bounds of the size that flocculated particles can reach before they are sheared apart by turbulence (van Leussen, 1988). Assuming that the production of turbulence must be balanced by dissipation, and applying log layer scaling, turbulent dissipation can be estimated as:

$$\epsilon = u_*^3 / \kappa z \quad (4-9)$$

where u_* is the turbulent shear velocity, κ is von Karmans constant (0.41) and z is the height above bed. Using the Reynolds stress estimates from ADVs deployed at the channel location to calculate u_* , it is possible to estimate turbulent dissipation. Although there were no direct measurements of the size of the flocs during this experiment, other authors have developed empirical relationships relating fall velocity to aggregate diameter. Sternberg et al. (1999) suggested the following relationship between the observed floc diameter (D in microns) and the observed fall velocity (w_s in mm/s) for aggregated particles on the continental shelf of northern California:

$$w_s = .0002 D^{1.54} \quad (4-10)$$

Using this relationship, we can estimate the diameter of the flocculated particles from the estimate of fall velocity. Figure 4-12a, shows a frequency histogram of floc diameter based on all of the data calculated following equation (4-7), prior to smoothing. Figure 4-12b, shows a similar histogram but for the estimated Kolmogorov micro-scale estimated following (4-8). Consistent with the results of Berhane et al. (1997) from work on the Amazon shelf, the average floc diameter is roughly half the average value of η .

Despite the fact the median value of η is larger than the estimated median diameter of the aggregated particles, there is significant overlap between the two

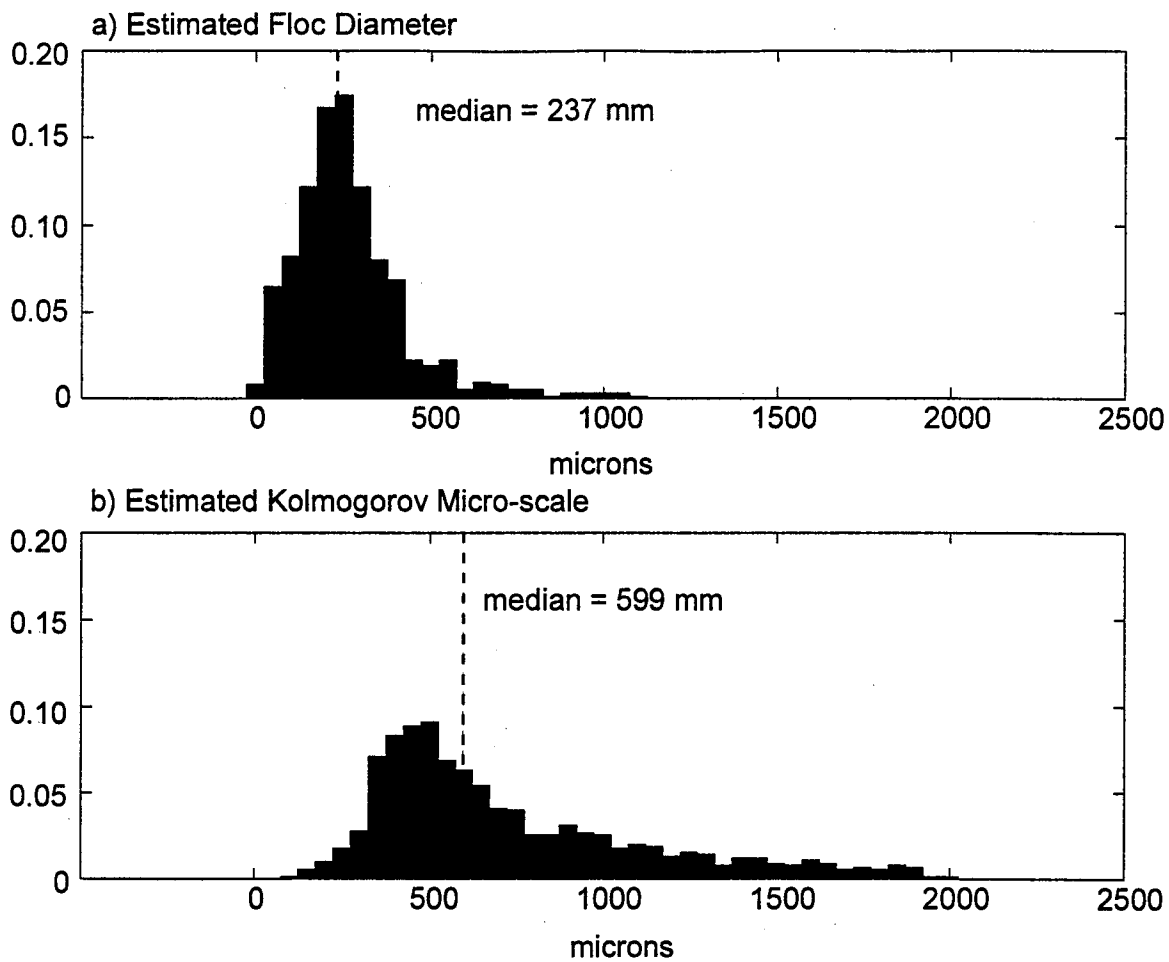


Figure 4-12. Frequency histogram of a) floc diameter calculated from the ADV estimate of fall velocity following equation (4-10); b) Kolmogorov micro-scale, estimated following equation (4-8).

histograms. Clearly in an estuary, the level of turbulence will vary at the tidal time scale. During slack conditions, η will be significantly larger than during peak flow. To look at the tidal variability of both η and the estimated floc diameter (D), the data were segregated by the phase of the tide using the velocity time series and the median values were plotted to represent an “average” tidal cycle. Figures 4-13 compares the average tidal cycle values of D and η . As expected, the values of η vary significantly during the tidal cycle. However, during maximum flood and maximum ebb, the value of η approaches that of D suggesting that under peak flow, the smallest scale of turbulence is approximately the same size as the flocculated particles.

Because the estimated dissipation is based upon simple log layer scaling using the measured bottom stress, which is largely unaffected by the overlying stratification, it is likely that the estimates of η do not realistically represent the impact of the internal asymmetry shown in figure 4-5. However, there does appear to be some evidence for the impact of this asymmetry in the tidal estimates of the floc diameter. There is a general trend for floc diameter to increase throughout both flood and ebb tide, reaching maximum values near slack water. The values decrease back to near minimum as the tidal currents begin to accelerate. However, floc growth during the flood is slower than during ebb, indicating greater limitation by the turbulent length scale during flood. It is clear from figure 4-13 that the time scale of floc growth is substantially slower than the rate of change of η . So while the maximum floc diameter may be set during energetic conditions, the floc growth rate is too slow for the aggregates to exist in a dynamic equilibrium where floc growth is balanced by floc breakup as suggested by Jackson (1995). It appears that the suspension exists in a partially flocculated state as suggested

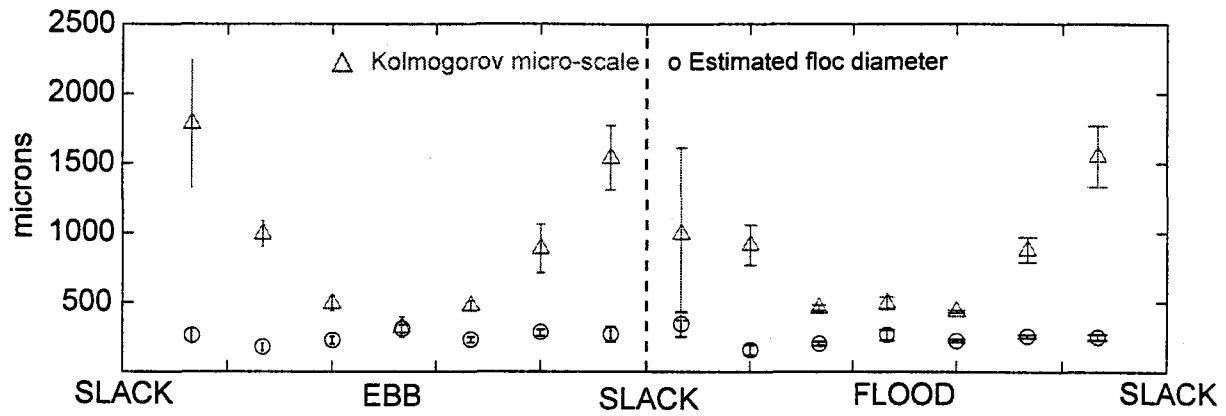


Figure 4-13. Comparison of the averaged tidal cycle values of the flocc diameter estimated following equation (4-10) (dark circles) and the Kolmogorov micro-scale estimated following equation (4-8) (light triangles). Vertical line represent one standard error.

by McCave (1985), where the aggregation rate is slow and settling removes sediment from suspension before complete flocculation can occur. In this situation, a tidal asymmetry in fall velocity caused by turbulent floc break-up is not only dependent upon the relative asymmetry in the Kolmogorov length scale, but also on the floc growth rate.

4.5 CONCLUSIONS

The net estuarine sediment transport is most often attributed to the landward flux of sediment, driven by the residual baroclinic estuarine circulation. However, tidal asymmetries in sediment resuspension can lead to sediment pumping, which are often the same order of magnitude as the residual advective flux. These asymmetries in resuspension can be driven either by asymmetries in bed stress or by asymmetries in internal mixing. Unlike asymmetries in bed stress, which are driven by the direction of the net pressure gradient forcing, asymmetries in internal mixing are impacted by tidal asymmetries in stratification. As a result, the eddy viscosity can be greater on flood than on ebb, even when the residual stress is ebb directed. Thus, asymmetries in bed stress and asymmetries in internal stress can influence tidal asymmetries in sediment resuspension with the opposite sense.

Observations of sediment flux collected from the channel location in the York River appear to be dominated by tidal asymmetries in internal mixing. At this location, tidal straining of the density field leads to greater sediment resuspension during the flood tide, resulting in up-estuary sediment flux even when the advective residual is directed down-estuary. The internal asymmetry dominates at the channel location because supply-limitation effectively decouples the asymmetry in bed stress from sediment resuspension. The opposite appears to be the case at the shoal site, where they advective

and pumping fluxes are both directed down-estuary. Neither supply-limitation nor significant tidal asymmetry in internal mixing was observed at the shoal location, leading to down-estuary sediment pumping. Thus, during the energetic spring tidal condition, there was significant up-estuary sediment pumping in the channel with down-estuary pumping over the shoals. Tidal asymmetries in fall velocity may have contributed to the up-estuary sediment pumping at the channel location. Estimates of fall velocity were greater during the more stratified ebb than they were during the flood tide near the bed. This asymmetry may reflect the tidal asymmetry in internal mixing caused by tidal straining. Estimates of the median floc diameter and the Kolmogorov micro-scale were the same order during periods of peak tidal flow, suggesting that turbulence is a controlling factor for floc size.

LITERATURE CITED

- Berhane, I.; Sternberg, R.W.; Kineke, G.C.; Milligan, T.G.; and Kranck, K. The variability of suspended aggregates on the Amazon continental shelf. *Continental Shelf Research*. 17:267-285; 1997.
- Burchard, H.; and Bolding, K. Comparative analysis of four second-moment turbulence closure models for the oceanic mixed layer. *Journal of Physical Oceanography*. 31:1943-1968; 2001.
- Businger, J.A.; Wyngaard, J.C.; Izumi, Y.; Bradley, E.F. Flux-profile relationships in the atmospheric surface layer. *Journal of Atmospheric Science*. 28:181-189; 1971.
- Canuto, V.M.; Howard, A.; Cheng, Y.; and Dubovikov, M.S. Ocean turbulence I: One-point closure model. Momentum and heat vertical diffusivities with and without rotation. *Journal of Physical Oceanography*. 31:1413-1426; 2001.
- Chant, R.J.; and Wilson, R.E. Secondary circulation in a highly stratified estuary. *Journal of Geophysical Research*. 102:23 207-23 216; 1997.
- Chant, R.J.; and Stoner, A.W. Particle trapping in a stratified flood-dominated estuary. *Journal of Marine Research*. 59:29-51; 2001.
- Charlton, J.A.; McNicoll, W.; and West, J.R. Tidal and freshwater induced circulation in the Tay Estuary. *Proceedings of the Royal Society of Edinburgh*. 75:11-27; 1975.
- Cleveland, W.S. Robust locally weighted regression and smoothing scatterplots. *Journal of the American Statistical Association*. 74:829-836; 1979.
- Deines, K.L. Backscatter estimation using broadband acoustic Doppler current profilers. *Oceans 99 MTS/IEEE Conference Proceedings*. 13-16 September, 1999.
- Eisma, D. Flocculation and deflocculation of suspended matter in estuaries. *Netherlands Journal of Sea Research*. 20:183-99; 1986.
- Elliott, A.J. Observations of the meteorologically induced circulation in the Potomac estuary. *Estuarine and Coastal Marine Science*. 6:285-299; 1978.
- Fisher, H.B. Mass transport mechanisms in partially stratified estuaries. *Journal of Fluid Mechanics*. 53:671-687; 1972.
- Friedrichs, C.T.; Hamrick, J.M. Effects of channel geometry on cross-sectional variations in along-channel velocity in partially stratified estuaries. in *Buoyancy Effects on Coastal and Estuarine Dynamics*, D.G. Aubrey and C.T. Friedrichs, Eds., Coastal and Estuarine Studies, Vol. 53, Amer. Geophys. Union, 283-300; 1996.

- Friedrichs, C.T.; Wright, L.D.; Hepworth, D.A.; and Kim, S.C. Bottom boundary layer processes associated with fine sediment accumulation in coastal seas and bays. *Continental Shelf Research*. 20:807-841; 2000.
- Fugate, D.C.; and Friedrichs, C.T. Determining concentration and fall velocity of estuarine particle populations using ADV, OBS and LISST. *Continental Shelf Research*. 22:1867-1886; 2002.
- Geyer, W.R. Influence of wind on dynamics and flushing of shallow estuaries. *Estuarine, Coastal and Shelf Science*. 44:713-722; 1997.
- Geyer, W.R.; Trowbridge, J.H.; and Bowen, M.M. The dynamics of a partially-mixed estuary. *Journal of Physical Oceanography*. 30:2035-2048; 2000.
- Geyer, W.R.; Woodruff, J.D.; and Traykovski, P. Sediment transport and trapping in the Hudson River Estuary. *Estuaries*. 24:670-679; 2001.
- Haas, L.W. The effect of the spring-neap tidal cycle on the vertical salinity structure of the James, York and Rappahannock Rivers, Virginia, U.S.A. *Estuarine Coastal Shelf Science*. 5:485-496; 1977.
- Hellweger, F.L.; Blumberg, A.F.; Schlosser, P.; Ho, D.T.; Caplow, T.; Lall, U.; and Li, H. Transport in the Hudson Estuary: A modeling study of estuarine circulation and tidal trapping. *Estuaries*. 27:527-538; 2004.
- Holdaway, G.P., Thorne, P.D.; Flatt, D.; Jones, S.E.; and Prandle, D. Comparison between ADCP and transmissometer measurements of suspended sediment concentration. *Continental Shelf Research*. 19:421-441; 1999.
- Huzzey, L.M.; and Brubaker, J.M. The formation of longitudinal fronts in a coastal plain estuary. *Journal of Geophysical Research*. 93:1329-1334; 1988.
- Jackson, G.A. Comparing observed changes in particle size spectra with those predicted using coagulation theory. *Deep Sea Research II*. 42:159-184; 1995.
- Jay, D.A.; and Smith, J.D. Residual circulation in shallow estuaries, 2: Weakly stratified and partially mixed, narrow estuaries. *Journal of Geophysical Research*. 95:733-748; 1990.
- Jay, D.A.; and Musiak, J.D. Particle trapping in estuarine tidal flows. *Journal of Geophysical Research*. 99:20 445-20 461; 1994.
- Kasai, A.; Hill, A.E.; Fujiwara, T.; and Simpson, J.H. Effect of the earth's rotation on the circulation in regions of freshwater influence. *Journal of Geophysical Research*. 105:16961-16969; 2000.

- Kim, S-C.; Friedrichs, C.T.; Maa, J.P-Y.; Wright, L.D. Estimating bottom stress in tidal boundary layers from acoustic Doppler velocimeter data. *Journal of Hydraulic Engineering*. 126:399-406; 2000.
- Kjerfve, B. Bathymetry as an indicator of net circulation in well mixed estuaries. *Limnology and Oceanography*. 23:816-821; 1978.
- Kranck, K. Particulate matter grain-size characteristics and flocculation in a partially-mixed estuary. *Sedimentology*. 28:107-114; 1981.
- Kranck, K.; and Milligan, T.G. Characteristics of suspended particles at an 11 hour anchor station in San Francisco Bay, California. *Journal of Geophysical Research*. 97:11 373-11 382; 1992.
- Large, W.G.; and Pond, S. Open ocean momentum flux measurements in moderate to strong winds. *Journal of Physical Oceanography*. 11:324-336; 1981.
- Lacy, J. R.; and Monismith, S.G. Secondary currents in a curved, stratified, estuarine channel. *Journal of Geophysical Research*. 106:31 283-31 302; 2001.
- Larouche, P.; Koutitonsky, V.G.; Chanut, J-P.; and El-Sabh, M.I. Lateral stratification and dynamic balance at the Matane transect in the lower Saint Lawrence Estuary. *Estuarine Coastal Shelf Science*. 24:859-871; 1987.
- Lerczak, J.A.; Geyer, W.R. Modeling the lateral circulation in straight, stratified estuaries. *Journal of Physical Oceanography*. 34:1410-1428; 2004.
- van Leussen, W. Aggregation of particles, settling velocity of mud flocs a review, In: Dronkers, J., and W, van Leussen (Eds.) *Physical Processes in Estuaries*. Springer-Verlag. 347-403; 1988.
- Li, H.; and O'Donnell, J. Tidally induced residual circulation in shallow estuaries with lateral depth variation. *Journal of Geophysical Research*. 102:27 915-27 929; 1997.
- Li, H.; Valle-Levinson, A.; Wong, K.C.; and Lwiza, K.M.M. Separating baroclinic flow from tidally induced flow in estuaries. *Journal of Geophysical Research*. 103:10 405-10 417; 1998.
- Lin, J.; and Kuo, A.Y. Secondary turbidity maximum in a partially mixed microtidal estuary. *Estuaries*. 24:707-720; 2001.
- Lynch, J.F.; Gross, T.F.; Sherwood, C.R.; Irish, J.D.; and Brumley, B.H. Acoustical and optical backscatter measurements of sediment transport in the 1988-1989 STRESS experiment. *Continental Shelf Research*. 17:337-366; 1997.

- Martin, W.; MacCready, P.; and Dewey, R. Boundary layer forcing of a semidiurnal cross-channel seiche. *Journal of Physical Oceanography*. 35:1518-1537; 2005.
- McCave, I.N. Mechanics of deposition of fine-grained sediments from nepheloid layers. *Geo-Marine Letters*. 4:243-245; 1985.
- Milligan, T.G.; Kineke, G.C.; Blake, A.C.; Alexander, C.R.; and Hill, P.S. Flocculation and sedimentation in the ACE Basin, South Carolina. *Estuaries*. 24:734-744; 2001.
- Noble, M.A.; Schroeder, W.W.; Wiseman, W.J.; Ryan, H.F.; and Gelfenbaum, G. Subtidal circulation patterns in a shallow, highly stratified estuary: Mobile Bay, Alabama. *Journal of Geophysical Research*. 101:25,689-25,703; 1996.
- North, E.W.; Chao, S-Y.; Sanford, L.P.; and Hood, R.R. The influence of wind and river pulses on an estuarine turbidity maximum: Numerical studies and field observations in Chesapeake Bay. *Estuaries*. 27:132-146; 2004.
- Nunes, R.A.; and Simpson, J.H. Axial convergence in a well-mixed estuary. *Estuarine Coastal Shelf Science*. 20:637-649; 1985.
- Officer, C.B. *Physical Oceanography of Estuaries and Associated Coast Waters*. John Wiley and Sons, New York, New York; 1976.
- Postma, H., Sediment transport and sedimentation in the estuarine environment, In: Lauff, G.H. (Ed.) *Estuaries*. A.A.A.S. Publ., 83:158-179; 1967.
- Pritchard, D.W. The dynamic structure of a coastal plain estuary. *Journal of Marine Research*. 15:33-42; 1956.
- Rippeth, T.P.; Fisher, N.P.; and Simpson, J.H. The cycle of turbulent dissipation in the presence of tidal straining. *Journal Physical Oceanography*. 31:2458-2471; 2001.
- Robinson, A.H.W. Ebb-flood channel systems in sandy bays and estuaries. *Geography*. 45:183-199; 1960.
- Schubel, J.R. Turbidity maximum of the northern Chesapeake Bay. *Science*. 6:1012-1015; 1968.
- Scott, C.F. A numerical study of the interaction of tidal oscillations and non-linearities in an estuary. *Estuarine Coastal Shelf Science*. 39:477-496; 1994.
- Scully, M.E.; and Friedrichs, C.T. The influence of asymmetries in overlying stratification on near bed turbulence and sediment suspension in a partially mixed estuary. *Ocean Dynamics*. 53:208-219; 2003.

- Scully, M.E.; Friedrichs, C.T.; and Brubaker, J.M. Control of estuarine stratification and mixing by wind-induced straining of the estuarine density field. *Estuaries*. 28:321-326; 2005.
- Scully, M.E.; and Friedrichs, C.T. The importance of tidal and lateral asymmetries in stratification to residual circulation in partially-mixed estuaries. *Journal of Physical Oceanography*, in press.
- Scully, M.E.; and Friedrichs, C.T. Sediment pumping by tidal asymmetry in a partially-mixed estuary. *Journal of Geophysical Research*, submitted.
- Sharples, J.; Simpson, J.H.; and Brubaker, J.M. Observations and modeling of periodic stratification in the upper York River Estuary, Virginia. *Estuarine, Coastal and Shelf Science*. 38:301-312; 1994.
- Simpson, J.H.; and Bowers, D. Models of stratification and frontal movement in the shelf seas. *Deep-Sea Research*. 28:727-738; 1981.
- Simpson, J.H.; Brown, J.; Matthews, J.P.; and Allen, G. Tidal straining, density currents and stirring in the control of estuarine stratification. *Estuaries*. 12:129-132; 1990.
- Simpson, J.H.; Sharples, J.; and Rippeth, T.P. A prescriptive model of stratification induced by freshwater runoff. *Estuarine, Coastal and Shelf Science*. 33:23-35; 1991.
- Simpson, J.H.; Williams, E.; Brasseur, L.H.; and Brubaker, J.M. The impact of tidal straining on the cycle of turbulence in a partially stratified estuary. *Continental Shelf Research*. 25:51-64; 2005.
- Smith, J.D.; and McLean, S.R. Spatially averaged flow over a wavy surface. *Journal Geophysical Research*. 82:1735-1746; 1977.
- Smith, R. Longitudinal dispersion of a buoyant contaminant in a shallow channel. *Journal of Fluid Mechanics*. 78:677-688; 1976.
- Soulsby, R.L.; and Dyer, K.R. The form of the near-bed velocity profile in tidally accelerating flow. *Journal Geophysical Research*. 86:8067-8074; 1981.
- Stacey, M.T.; Monismith, S.G.; and Burau, J.R. Measurements of Reynolds stress profiles in unstratified tidal flow. *Journal of Geophysical Research*. 104:10933-10950; 1999.
- Stacey, M.T.; Burau, J.R.; and Monismith, S.G. Creation of residual flows in a partially stratified estuary. *Journal of Geophysical Research*. 106:17 013-17 037; 2001.

- Sternberg, R.W.; Berhane, I.; and Ogston, A.S. Measurement of size and settling velocity of suspended aggregates on the northern California continental shelf. *Marine Geology*. 154:43-53; 1999.
- Thorne, P.D.; and Hanes, D.M. A review of acoustic measurement for small-scale sediment processes. *Continental Shelf Research*. 22:602-632; 2002.
- Traykovski, P.; Geyer, R.; and Sommerfield, C. Rapid sediment deposition and fin-scale strata formation in the Hudson estuary. *Journal of Geophysical Research*. 109:doi:10.1029/2003JF000096; 2004.
- Trowbridge, J.H.; Geyer, W.R.; Bowen, M.M.; and Williams, A.J. Near-bottom turbulence measurements in a partially mixed estuary: turbulent energy balance, velocity structure, and along-channel momentum balance. *Journal Physical Oceanography*. 29:3056-3072; 1999.
- Uncles, R.J.; and Stephens, J.A. Observations of currents, salinity, turbidity and intertidal mudflat characteristics and properties in the Tavy Estuary, UK. *Continental Shelf Research*. 20:1531-1549; 2000.
- Valle-Levinson, A.; Wong, K.-C.; Kamazima, K.M.M. Fortnightly variability in the transverse dynamics of a coastal plain estuary. *Journal of Geophysical Research*. 105:3413-3424; 2000.
- Valle-Levinson, A.; Reyes, C.; and Sanay, R. Effects of bathymetry, friction, and rotation on estuary-ocean exchange. *Journal Physical Oceanography*. 33:2375-2393; 2003.
- Wang, D.P. Wind-driven circulation in the Chesapeake Bay, Winter, 1975. *Journal of Physical Oceanography*. 9:564-572; 1979.
- Wang, H.V.C.; and Chao, S.Y.-. Intensification of subtidal surface currents over a deep channel in the upper Chesapeake Bay. *Estuarine Coastal Shelf Science*. 42:771-785; 1996.
- Weisberg, R.H. The nontidal flow in the Providence River of Narragansett Bay: A stochastic approach to estuarine circulation. *Journal of Physical Oceanography*. 6:721-734; 1976.
- Winant, C.D.; and Gutierrez de Velasco, G. Tidal dynamics and residual circulation in a well-mixed inverse estuary. *Journal of Physical Oceanography*. 33:1365-1379; 2003.
- Wong, K.-C. On the nature of transverse variability in a coastal plain estuary. *Journal of Geophysical Research*. 99:14 209-14 222; 1994.

VITA

MALCOLM ELLIS SCULLY

Born August 24, 1971 in Athens, Greece. Graduated in 1993 from the University of Virginia with a Bachelor of Arts in Environmental Science. Lived and worked in Telluride, CO, Ocracoke, NC, Washington, DC, and San Francisco, CA from 1993 to 1998. Received a Master of Science degree in Physical Sciences from the College of William and Mary, School of Marine Science in December 2001. Received a Doctor of Philosophy degree in Physical Sciences from the College of William and Mary, School of Marine Science in December 2005.